

## Order out of Randomness : Self-Organization Processes in Astrophysics

Markus J. Aschwanden<sup>1</sup>

<sup>1</sup>) *Lockheed Martin, Solar and Astrophysics Laboratory, Org. A021S, Bldg. 252, 3251 Hanover St., Palo Alto, CA 94304, USA; e-mail: aschwanden@lmsal.com*

Felix Scholkmann<sup>2</sup>

<sup>2</sup>) *Research Office for Complex Physical and Biological Systems, Mutschellenstr. 179, 8038 Zürich, Switzerland; e-mail: felix.scholkmann@gmail.com*

William Béthune<sup>3</sup>

<sup>3</sup>) *DAMTP, University of Cambridge, CMS, Wilberforce Road, Cambridge CB3 0WA, United Kingdom; e-mail: wb288@damtp.cam.ac.uk*

Werner Schmutz<sup>4</sup>

<sup>4</sup>) *Physikalisch Meteorologisches Observatorium Davos and World Radiation Center, Dorfstrasse 33, 7260 Davos Dorf, Switzerland ; e-mail: werner.schmutz@pmodwrc.ch*

Valentina Abramenko<sup>5</sup>

<sup>5</sup>) *Crimean Astrophysical Observatory, Russian Academy of Science, Nauchny, Bakhchisaray 298409, Crimea ; e-mail: vabramenko@gmail.com*

Mark Cheung<sup>6</sup>

<sup>6</sup>) *Lockheed Martin, Solar and Astrophysics Laboratory, Org. A021S, Bldg. 252, 3251 Hanover St., Palo Alto, CA 94304, USA; e-mail: cheung@lmsal.com*

Daniel Müller<sup>8</sup>

<sup>8</sup>) *European Space Agency ESTEC (SCI-9), P.O.Box 299, NL-2200 AG, The Netherlands; e-mail: dmueller@cosmos.esa.int*

Arnold Benz<sup>9</sup>

<sup>9</sup>) *Institute for Astronomy, ETH, Zurich; Institute of 4D Technologies, FHNW, Windisch, Switzerland ; e-mail: benz@astro.phys.ethz.ch*

Juergen Kurths<sup>10</sup>

<sup>10</sup>) *Potsdam Institute for Climate Research, 14473 Potsdam, Germany ; e-mail: juergen.kurths@pik-potsdam.de*

Guennadi Chernov<sup>11</sup>

<sup>11</sup>) *Pushkov Institute of Terrestrial Magnetism, Ionosphere and Radio Wave Propagation, Russian Academy of Sciences, Izmiran, Russia ; e-mail: gchernov@izmiran.ru*

Alexei G. Kritsuk<sup>12</sup>

<sup>12</sup>) *Physics Department and Center for Astrophysics and Space Sciences, University of California, San Diego, La Jolla, CA 92093-0424, USA ; e-mail: akritsuk@ucsd.edu*

Jeffrey D. Scargle<sup>13</sup>

<sup>13</sup>) *NASA Ames Research Center, Astrobiology and Space Science Division, Moffett Field, CA 94035, USA ; e-mail: jeffrey.d.scargle@nasa.gov*

Andrew Melatos<sup>14</sup>

<sup>14</sup>) *School of Physics, University of Melbourne, Parkville, VIC 3010, Australia ; e-mail: amelatos@unimelb.edu.au*

Robert, V. Wagoner<sup>15</sup>

<sup>15</sup>) *Dept. of Physics and KIPAC, Stanford University, Stanford, CA 94305-4060, USA ; e-mail: wagoner@stanford.edu*

Virginia Trimble<sup>16</sup>

<sup>16</sup>) *University of California, Irvine, Department of Physics and Astronomy, Irvine, CA 92697-4575, USA ; e-mail: vtrimble@astro.umd.edu*

William Green<sup>17</sup>

<sup>17</sup>) *Department of Physics, Florida State University, Tallahassee, Florida 32306, USA ; e-mail: whgreen@fsu.edu*

## ABSTRACT

Self-organization is a property of dissipative nonlinear processes that are governed by a global driving force and a local positive feedback mechanism, which creates regular geometric and/or temporal patterns, and decreases the entropy locally, in contrast to random processes. Here we investigate for the first time a comprehensive number of (17) self-organization processes that operate in planetary physics, solar physics, stellar physics, galactic physics, and cosmology. Self-organizing systems create spontaneous “*order out of randomness*”, during the evolution from an initially disordered system to an ordered quasi-stationary system, mostly by quasi-periodic limit-cycle dynamics, but also by harmonic (mechanical or gyromagnetic) resonances. The global driving force can be due to gravity, electromagnetic forces, mechanical forces (e.g., rotation or differential rotation), thermal pressure, or acceleration of nonthermal particles, while the positive feedback mechanism is often an instability, such as the magneto-rotational (Balbus-Hawley) instability, the convective (Rayleigh-Bénard) instability, turbulence, vortex attraction, magnetic reconnection, plasma condensation, or a loss-cone instability. Physical models of astrophysical self-organization processes require hydrodynamic, magneto-hydrodynamic (MHD), plasma, or N-body simulations. Analytical formulations of self-organizing systems generally involve coupled differential equations with limit-cycle solutions of the Lotka-Volterra or Hopf-bifurcation type.

*Subject headings:* astrophysics — planetary physics — stellar physics — solar physics — self-organization — limit-cycle dynamics — instabilities — Lotka-Volterra systems — Hopf bifurcation

## 1. INTRODUCTION

*Self-organization is the spontaneous often seemingly purposeful formation of spatial, temporal, spatio-temporal structures or functions in systems composed of few or many components. In physics, chemistry, and biology, self-organization occurs in open systems driven away from thermal equilibrium. The process of self-organization can be found in many other fields also, such as economy, sociology, medicine, technology* (Haken 2008). Self-organization creates “order out of randomness” that is opposite to random processes with increasing entropy. Self-organization is a spontaneous process that does not need any control by an external force. It is often initiated by random fluctuations where the local reaction is amplified by a positive feedback mechanism. It can evolve into a stationary cyclic dynamics governed by a (strange) attractor, and develops, as a result of many microscopic interactions, a macroscopic regular geometric spatial pattern (Nicolis and Prigogine 1977; Kauffman 1993, 1996). In this review we compile for the first time a comprehensive set of self-organizing systems observed or inferred in astrophysics. For each astrophysical self-organizing system we discuss a physical model, generally in terms of a system-wide driving force and a positive feedback mechanism, which by mutual interactions evolve into a self-organized quasi-stationary pattern that is different from a random structure. Note that the term “self-organization” should not be confused with the term “self-organized criticality” (Bak et al. 1987; Pruessner 2012; Aschwanden et al. 2016), which is just one (of many) self-organizing complex systems, producing power law-like size distributions of scale-free avalanche events, whereas self-organizing systems usually evolve into a specific quantized (spatial or temporal) scale that is not scale-free.

Physical models of self-organization involve non-equilibrium processes, mechanical resonances, magneto-convection, plasma turbulence, superconductivity, phase transitions, or chemical reactions. In planetary physics, the principle of self-organization has been applied to harmonic orbit resonances (Aschwanden 2018; Aschwanden and Scholkmann 2018), Jupiter’s or Saturn’s rings and moons (Peale 1976), protoplanetary disks (Kunz and Lesur 2013; Béthune et al. 2016), Jupiter’s Red Spot (Marcus 1993), and the planetary entropy balance (Izakov 1997). In solar physics, it was applied to photospheric granulation (Krishan 1991, 1992), solar magnetic fields (Vlahos and Georgoulis 2004; Kitiashvili et al. 2010), the magnetic solar cycle (Hale 1908; Consolini et al. 2009), the evaporation-condensation cycle of flares (Krall and Antiochos 1980; Kuin and Martens 1982), and to quasi-periodic solar radio bursts (Zaitsev 1971; Aschwanden and Benz 1988). In astrophysics, it was applied to galaxy and star formation (Bodifée 1986; Cen 2014). An overview of 17 self-organization processes operating in astrophysical environments is given in Table 1, which lists also the underlying physical driving forces and feedback mechanisms. Besides the astrophysical applications, the process of self-organization can be found in many other fields, such as magnetic reconnection in laboratory physics (Yamada 2007; Yamada et al. 2010; Zweibel and Yamada 2009; <http://cmso.uchicago.edu>), plasma turbulence (Hasegawa 1985), magnetospheric physics (Valdivia et al. 2003; Yoshida et al. 2010), ionospheric physics (Leyser 2001), solid state physics and material science (Müller and Parisi 2015), chemistry (Lehn 2002), sociology (Leydesdorff 1993), cybernetics and learning algorithms (Kohonen 1989; Geach 2012), or biology (Camazine et al. 2001). A more specific overview of self-organization processes in non-astrophysical fields is provided in Table 2.

In this review we discuss 17 different astrophysical processes that exhibit self-organization. For the definition of the term “self-organization” we proceed pragmatically. A nonlinear dissipative process qualifies to be called a “self-organization” process if it fulfills at least one of the following six criteria: (S) A spatially ordered pattern that is significantly different from a random pattern; (T) a temporally ordered (e.g., quasi-periodic) structure that is significantly different from random time intervals; (E) a system with negative entropy change ( $dS < 0$ ); (LC) a nonlinear dissipative system with limit-cycle behavior (which by definition produces quasi-periodic temporal oscillations); (R) a nonlinear dissipative system with resonances; and (I) a nonlinear dissipative system that is driven by an external force and counter-acted by a positive feedback force, triggered by an instability or turbulence. We classify the 17 analyzed self-organization processes with these defining criteria (S, T, E, LC, R, I) in Table 1.

The structure of this review is organized by the various subfields in astrophysics, such as planetary physics (Section 2), solar physics (Section 3), stellar physics (Section 4), galactic physics (Section 5), and cosmology (Section 6). A discussion of randomness, self-organization, and self-organized criticality processes (Section 7) and a summary of the conclusions (Section 8) is given at the end. Each description of the 17 self-organization processes is annotated with a critical assessment at the end of each Section. The selected 17 cases are all explicitly addressed as self-organization processes by the authors of the cited studies, but we are aware that there are many more phenomena in astrophysics that implicitly qualify as self-organization processes, although they are often not labeled as such in the original literature. As a caveat, our review thus contains some bias towards citations with author-identified self-organization processes.

## 2. PLANETARY PHYSICS

### 2.1. Planetary Spacing

Our solar system exhibits planet distances  $R_i, i = 1, \dots, n$  from the Sun that are not randomly distributed, but rather follow a regular pattern that has been quantified with the Titius-Bode law, known since 250 years. The original Titius-Bode law approximated the planet distance ratios by a factor of two, i.e.,  $R_{i+1}/R_i \approx 2$ , while a generalized Titius-Bode law specified the relationship with a logarithmic spacing and a constant geometric progression factor  $Q$ , i.e.,  $R_{i+1}/R_i = Q$  (Blagg 1913). According to Kepler’s third law, a distance ratio  $Q$  corresponds to a period ratio  $q = T_{i+1}/T_i = Q^{(3/2)}$  of the orbital time periods  $T$ . However, both the original and the generalized Titius-Bode law represent empirical laws without a physical model.

Planet spacing with low harmonic ratios  $q$  of their orbital time periods  $T$ , such as  $q=(m:n)$ , with  $n = 1, 2, 3$  and  $m \geq n + 1$ , have been interpreted as harmonic (mechanical) orbit resonances and are expected to occur in a self-organizing system with stable long-lived orbits (Laplace 1829; Peale 1976), especially in systems with resonant chains (e.g., Mills et al. 2016). One of the main heuristic understandings of chaos and instability is that a planet system is generated by overlapping resonances (Wisdom 1980), which explains why not all (or even the majority of) planet systems have exact (2-body) harmonic resonances (Daniel Fabrycky, private communication).

Recently, the planet spacing has been fitted with 5 low-harmonic ratios (Aschwanden 2018), or with 7 low-harmonic ratios  $q = (2 : 1), (3 : 1), (3 : 2), (4 : 3), (5 : 2), (5 : 3), (5 : 4)$  that were found to fit 648 pairs of exo-planet distances (Aschwanden and Scholkmann 2018), using observations of the KEPLER mission. A distribution of the 7 best-fit harmonic ratios of orbital periods is shown for detected and (interpolated) missing exo-planet pairs in Fig. (1). In other studies with Kepler data, resonances with low-harmonic ratios were found to be uncommon among small planets with periods shorter than a few years (Fabrycky et al. 2014; Winn and Fabrycky 2015). Gaps with ratios  $q > 3$  were interpreted as missing planets and interpolated with low-harmonic ratios in the analysis of Aschwanden and Scholkmann (2018).

Most recently, the Laplacian 3-body resonances have been studied in great detail in the TRAPPIST-1 exo-planet system (e.g., Luber et al. 2017; Scholkmann 2017), which contains 7 planets and is continuously monitored by the Kepler mission. The 6 planet spacings of TRAPPIST-1 closely match the low-harmonic ratios  $q = (4 : 3), (3 : 2), (5 : 3)$  within an accuracy of  $\lesssim 1\%$  (Luger et al. 2017; Scholkmann 2017; Aschwanden and Scholkmann 2017).

Harmonic planet orbits represent a special solution of the general N-body problem in celestial mechanics, which can be expressed by  $n$  second-order differential equations,

$$m_i \frac{d^2 \mathbf{R}_i}{dt^2} = G \sum_{j=1}^n \frac{m_i m_j}{r_{ij}^3} \mathbf{r}_{ij} \quad i = 1, \dots, n, \quad i \neq j, \quad (1)$$

where  $G$  is the Newton gravitational constant,  $m_i$  and  $m_j$  are two different masses,  $\mathbf{R}_i$  and  $\mathbf{R}_j$  are their spatial vectors in a Cartesian coordinate system, and  $\mathbf{r}_{ij} = (\mathbf{R}_j - \mathbf{R}_i)$  are the vectors between two bodies, with  $\mathbf{r}_{ij} = -\mathbf{r}_{ji}$ .

The dynamics of two planets orbiting the Sun can be formulated with a N-body problem (with  $N = 3$ ),

$$\ddot{x}_1 = -Gm_2 \frac{(x_1 - x_2)}{|x_1 - x_2|^3} - Gm_3 \frac{(x_1 - x_3)}{|x_1 - x_3|^3} \quad (2)$$

$$\ddot{x}_2 = -Gm_3 \frac{(x_2 - x_3)}{|x_2 - x_3|^3} - Gm_1 \frac{(x_2 - x_1)}{|x_2 - x_1|^3} \quad (3)$$

$$\ddot{x}_3 = -Gm_1 \frac{(x_3 - x_1)}{|x_3 - x_1|^3} - Gm_2 \frac{(x_3 - x_2)}{|x_3 - x_2|^3}, \quad (4)$$

The 3-body problem is treated in the textbook *Solar System Dynamics* by Murray and Dermott (1999) and recently reviewed in Lissauer and Murray (2007) and Musielak and Quarles (2015), building on the work of Isaac Newton, Jean le Rond d’Alembert, Alexis Clairaut, Joseph-Louis Lagrange, Pierre-Simon Laplace, Heinrich Bruns, Henri Poincaré, and Leonard Euler. Some restricted solutions yield stationary orbits in the Lagrangian points L1 to L5. Numerical searches for periodic orbits and resonances based on approximations to harmonic oscillators (similar to the physical model of coupled pendulums) yield the following nominal resonance location  $a_3$  for a third body that orbits between the primary and secondary body (internal resonance) (Murray and Dermott 1999),

$$a_3 = \left( \frac{k}{k+l} \right)^{2/3} \left( \frac{m_1}{m_1+m_2} \right) a_2, \quad (5)$$

where  $m_1$  is the mass of the first body (e.g., the Sun),  $m_2$  the mass of the secondary body (e.g., Venus),  $a_2$  is the semi-major axis of the secondary body,  $a_3$  the distance of the third body (e.g., Mercury) that orbits between the first and second body,  $l$  is the order of the resonance, and  $(k, l)$  are integer numbers. Since the planet masses are much smaller than the solar mass, the relationship (Eq. 5) simplifies to,

$$a_3 \approx \left( \frac{k}{k+l} \right)^{2/3} a_2, \quad (6)$$

where the exponent  $(2/3)$  results from Kepler’s third law, e.g.,  $a \propto T^{(2/3)}$ , with  $T$  the orbital period, while orbital periods have harmonic integer ratios  $q = T_2/T_3 \propto (k+l)/k$ . This yields the ratios  $q = (2 : 1), (3:2), (4:3), (3:1), (5:3), (4:1), (5:2)$  for the lowest orders  $l = 1, 2, 3$ . In Table 3 we list the harmonic ratios (H1:H2) from our solar system, or the order of the resonances  $[l,k]$  that fit the observed orbital periods best, which includes the harmonic ratios  $(2:1), (3:1), (3:2), (5:2)$ , and  $(5:3)$ . The resulting planet distance ratios agree with the observed semi-major axis with an accuracy of about 2%, ( $a_{\text{harm}}/a_{\text{obs}} = 0.99 \pm 0.02$ , i.e., see mean and standard deviation of ratios in last column of Table 3), which clearly demonstrates that the spacing of planets obeys a regular pattern that is not consistent with random locations. In the terminology of self-organizing systems, the driver of the system is the gravitational force, while the feedback mechanism that creates order out of random is the orbit stabilization that occurs at low harmonic ratios. Planets may have been formed initially at “chaotic” distances from the Sun, but the long-term stable orbits survive in the end, which apparently require gravitational resonances at low-harmonic orbital ratios.

The planetary spacing can be described in terms of two hierarchical self-organization processes: (i) the Keplerian orbital motion, and (ii) the secular precession. The Keplerian orbital motion is driven by the gravitational force, while the balance with the centrifugal force represents the feedback mechanism, resulting into an ellipse trajectory with some eccentricity (Appendix A). This can be considered as a self-organizing system with a limit cycle that corresponds to the orbital period. If the planet has a large eccentricity, the Sun-planet distance varies around the equilibrium value, while a circular motion corresponds to a fixed limit cycle with a constant distance from the Sun. We show a phase diagram of the planet velocity  $v$  as a function of the distance  $R$  in Fig. (2). On top of the Keplerian motion we have gravitational disturbances from other planets that vary the secular motion of the planet. Gravitational disturbances are then the driving forces, while the low-harmonic resonances represent the feedback mechanisms that self-organize multiple planet distances into a quantized (non-random) spatial pattern. This is illustrated by the harmonic ratios of the planet distances shown in Fig. (1). In essence, two self-organization mechanisms control the orbits of planets.

Alternative mechanisms besides gravitational N-body resonance self-organization have been proposed also, such as: (i) Hierarchical self-organization processes based on sequential resonance accretion (starting with the accretion of massive objects first) and 2-body resonance capture of planetesimals in the primordial solar nebula (Patterson 1987); (ii) plasma self-organization driven by the development to minimum energy states of the generic solar plasma during protostar formation (Wells 1989a, 1989b, 1990); (iii) susequent mass ejections into planetary rings around a central rotating body with magnetic field properties predicted by stochastic electrodynamics (Surdin et al. 1980), (iv)

retarded gravitational 2-body resonance, i.e., macroscopic quantization of orbital parameters due to finite gravitational propagation speed (Gine 2007); or (v) quantization of orbital periods in terms of the quantum-mechanical Schrödinger equation (Perinov et al. 2007; De Neto et al. 2004; Scardigli 2007; Chang 2013).

*Critical Assessment:* The spacing of planets, moons, or exo-planets exhibit quantized values that correspond to low-harmonic ratios according to some studies, in which large period ratios of planet pairs are interpreted as gaps with missing (un-detected or non-existing) planets. A regular pattern of orbital periods ( $T$ ), produced by low-harmonic ratios of orbital resonances ( $R$ ), causes then also a regular pattern in planetary spacings ( $S$ ), via Kepler's third law. Other studies find that harmonic ratios are rare for exo-planets with orbital periods of less than a few years. The physical model of Lagrangian mean-motion resonances predicts exact harmonic ratios (in resonant chains), but secular disturbances, planet migrations, and overlapping resonances (Wisdom 1980) may cause slowly-varying deviations. Nevertheless, the fact that harmonic ratios fit the planet orbital periods in the order of a few percents, strongly indicates the presence of a self-organizing system, opposed to randomness (Table 1: qualifiers  $R, S, T$ ).

## 2.2. Planetary Rings and Moons

Planetary systems with moons and rings can be considered as miniature versions of solar (or stellar) systems, as noted by Galileo, and thus may have a similar formation process and are governed by the same celestial mechanics. For instance, the mean motions of the inner three Galilean satellites of Jupiter (Io, Europa, Ganymede) exhibit harmonic orbits with a very high precision (by nine significant digits; Peale 1976), a property that has been interpreted by Laplace (1829) as evidence for the high stability of resonant orbits. Besides the Galilean satellites, further orbital resonance commensurabilities were found for Saturn moons (Franklin et al. 1971; Sinclair 1972; Greenberg 1973; Colombo et al. 1974; Peale 1976), and for asteroids-Jupiter resonances such as the Trojans (Brown and Shook 1933; Takenouchi 1962; Schubart 1968; Sinclair 1969; Marsden 1970; Lecar and Franklin 1973; Franklin et al. 1975; Peale 1976). Planetary rings have been found for all giant planets (Jupiter, Saturn, Uranus, and Neptune). A reconstruction of the Saturn ring system from Cassini observations is shown in Fig. (3).

If we hypothesize that planets and moons are preferentially located at low-harmonic orbits, how do we explain the existence of gaps in a ring system, such as the Cassini division or the Encke gap in Saturn's ring system? If moons form by accretion of planetesimals that orbit in close proximity to the accreting moon, a gap will result after sweeping over many nearby orbits, with the growing moon sitting in the middle of the gap. Therefore, gaps and moons are essentially cospatial in a long-term stable system. The most prominent "shepherding moon" in Saturn's ring system is the satellite Mimas, which is responsible for the strongest resonance, i.e., the Cassini Division, a 4700-km gap between Saturn's A and B rings (Porco and Hamilton 2000; McFadden et al. 1999, 2007). The two smaller moons Janus and Epimetheus cause the sharp outer edge of the A ring. The 320-km Encke gap in the outer A ring is believed to be controlled by the 20-km diameter satellite Pan. At Uranus, Cordelia and Ophelia have the role of "shepherding moons". The moon Galatea plays a similar role in Neptune's Adams ring.

The idea of self-organization in planetary rings has already been raised by Gor'kavyji and Fridman (1991). Gravitational forces and collisional deflection represent the drivers, while harmonic orbit resonances produce a feedback mechanism to organize the flat planetary ring plane into discrete rings, mostly because harmonic orbits tend to be more stable statistically. If the phenomenon of harmonic orbit resonances would not exist, randomized collisions only would determine the dynamics of ring particles, leading to a smooth and homogeneous planetary disk (or an asteroid belt or Oort cloud), rather than to quantized rings. The spatial pattern of rings with quantized ratios in their distance from the center of a planet (e.g., Saturn, Jupiter, Uranus, Neptune) thus is a manifestation of a self-organizing "ordered" scheme beyond a random pattern.

*Critical Assessment:* The argument to explain the harmonic structure of planetary rings is identical to the previously discussed case of planetary distances, because both are believed to be produced by the same stabilizing effect of orbital resonances with low-harmonic ratios. The arrangement of rings in quantized distances reveals a regular pattern in space (S) and time (T) that is beyond randomness, governed by mechanical resonances (R). These properties (R,S,T) argue in favor of a self-organization system (Table 1: qualifiers R,S,T).

### 2.3. Protoplanetary Disks

The formation of planets can obviously be seen as a self-organizing process, creating "order out of randomness". The interstellar gas, initially randomly distributed in a molecular cloud, collapses under its own gravity to form a young stellar object. Unless it loses its angular momentum, the gas cannot directly fall onto the newly born star: its angular velocity would increase and matter would be centrifugally expelled at larger radii. In the frame co-rotating with the gas, the effective gravitational potential is minimal in a plane, where dissipative processes allow the protoplanetary (or circum-stellar) disk to form. Dozens of such disks have now been observed over a range of wavelengths (McCaughrean and O'dell 1996), and their link to planet formation casts no doubt, since planets have been observed in older "debris disks" (Kospal et al. 2009). The imaging of dust emission, whether thermal or scattered, has revealed a number of large-scale structures in protoplanetary disks. Such features include spiral arms (Muto et al. 2012; Benisty et al. 2015) or cavities in the innermost regions of the disk (e.g., Andrews et al. 2011). The former are generally attributed to the excitation of density waves by massive planets, while the latter could result from accretion and/or photo-evaporation of the inner disk (Alexander et al. 2006; Koepferl et al. 2013). Horseshoe-shaped dust concentrations have also been identified in several disks (Fukagawa et al. 2013; van der Marel et al. 2013); it is commonly agreed that these could correspond to large-scale anticyclonic vortices in the gas flow (Birnstiel et al. 2013).

The most puzzling structures remain the axisymmetric dust gaps and rings observed in some disks, see Fig. (4). It is tempting to attribute them to gaps carved by protoplanets and their gravitational resonances (Crida et al. 2006; Baruteau and Papaloizou 2013), but it is unclear how several massive planetary bodies could already be formed in such young disks. One class of mechanisms relies on the coupling between the gas and large-scale magnetic fields. Magnetic fields are thought to drive the bipolar jets emitted perpendicularly to the disk plane (Cabrit et al. 2011). The coupling of magnetic fields with the electrically neutral gas in the outer disk is still possible via collisions with the few charged species (e.g., Wardle and Ng 1999). Of particular relevance for this review, the magneto-hydrodynamic (MHD) mechanism identified by Kunz and Lesur (2013) and further investigated by Béthune et al. (2016) generates self-organized, regularly spaced axisymmetric structures in the gas flow. Such structures would affect the migration of dust grains and could produce dust rings and gaps. MHD processes have received an increasing interest after realizing that for perfectly ionized Keplerian disks, arbitrarily weak magnetic fields could trigger a linear instability, the magneto-rotational instability (MRI) (Balbus and Hawley 1991), saturating in a turbulent state. In this turbulent flow, angular momentum could be "viscously" transported outwards (Shakura and Sunyaev 1973), thus allowing the observed accretion of gas onto the star. In weakly ionized plasmas, this instability can be damped (Jin 1996; Kunz and Balbus 2004) or modified in nature (Balbus and Terquem 2001; Kunz 2008). The transport of magnetic field in weakly ionized disks can be described via a modified induction equation:

$$\frac{\partial B}{\partial t} = \nabla \times [v \times B - \eta_O J - \eta_H J \times e_B + \eta_A (J \times e_B) \times e_B] , \quad (7)$$

where  $B$  is the magnetic field locally along  $e_B$ ,  $J = \nabla \times B$  is the electric current density, and  $\eta_{O,H,A}$  are the Ohmic, Hall and ambipolar diffusivities. Ohmic and ambipolar diffusions are indeed dissipative terms, respectively caused by collisions of electrons and ions. The Hall term is not a dissipative one: it describes the collisionless drift between electrons and ions and can only transport magnetic energy via whistler waves. Retaining only the ideal and Hall terms

amounts to neglecting the ion dynamics, following the induction of magnetic field by electrons only. In this limit, a linear instability remains that could sustain the turbulent transport of angular momentum in accretion disks (Wardle 1999). Early simulations including the Hall term showed that the Hall-MRI would still saturate in a turbulent state (Sano and Stone 2002a,b), though with varying effective viscosities. However, the Hall term might largely dominate the ideal induction term in the midplane of protoplanetary disks (Kunz and Balbus 2004). In this regime, the Hall-shear instability still operates in Keplerian disks, but with a different outcome (Kunz and Lesur 2013). After a phase of linear growth, the instability breaks into a non-linear and disordered regime. From this turbulent phase, high magnetic flux regions progressively merge together, ultimately separating contiguous regions of strong magnetic field from regions devoid of magnetic flux.

This behavior can be understood as follows. The linear instability requires a magnetic field that is sufficiently weak, such that the shear rate of the flow is larger than the whistler waves frequency at a given scale. Note, if the flow along  $v_y$  is sheared in the  $x$  direction, then the shear rate is defined as  $\partial_x v_y$ . Besides, the instability generates a magnetic stress  $\mathcal{M} = -B \otimes B$ , i.e. a tension of the magnetic field lines that can exchange momentum with the plasma. Retaining only the Hall term, Eq. (7) can be recast

$$\frac{\partial B}{\partial t} = \ell_H \nabla \times [\nabla \cdot \mathcal{M}] , \quad (8)$$

where  $\ell_H = \eta_H/v_A$ , the effective Hall diffusivity divided by the Alfvén velocity, happens to be independent of the magnetic field intensity (e.g., Lesur et al. 2014); this coefficient, analogous to an ion skin depth, was assumed to be constant for simplicity. Projected on the direction normal to the disk, this equation implies that magnetic flux is transported away from stress maxima, and this opens a route to self-organization. In the limit of weak magnetic flux, the linear instability has accordingly small growth rates and does not generate a significant stress. In the limit of strong magnetic flux, whistler waves can propagate despite the strong shear, when the Keplerian flow becomes linearly stable. For intermediate intensities of the magnetic flux, the instability generates a magnetic stress that effectively pushes magnetic flux away. If the magnetic flux locally increases, the flow can be stabilized, the magnetic stress becomes locally minimal, and therefore the stabilized region becomes a sink for magnetic flux. Eventually, these magnetic concentrations grow and spread in the azimuthal direction. If something tries to spread the magnetic flux radially, this will decrease its intensity down to the point where the linear instability is triggered again; as a feedback, the instability generates magnetic stress, thus confining magnetic flux again. Given the total magnetic flux through the disk, the turbulent and ordered phases are two available outcomes for the flow. The Hall effect, when strong enough, allows a spontaneous transition from the turbulent phase to an ordered equilibrium featuring large-scale and long-lived structures. Its relevance to astrophysical disks is uncertain though. The main caveat of these studies is the neglect of vertical stratification, i.e. the transition from the dense disk to its dilute and strongly magnetized corona. Results from numerical simulations (Fig. 5) including all three non-ideal MHD terms in Eq. (7) suggest that self-organization is inhibited by the density stratification (Lesur et al. 2014; Bai 2015; Béthune et al. 2017). Still, striped structures have been observed in stratified simulations of strongly magnetized disks (Moll 2012); axisymmetric magnetic accumulations could be a generic feature of MHD turbulent disks (Bai and Stone 2014; Ruge et al. 2016), most apparent in the presence of ambipolar diffusion (Béthune et al. 2017; Simon et al. 2017). At the moment, this behavior lacks a robust explanation.

*Critical Assessment: The argument of a self-organization process in the evolution of a protoplanetary disk is mostly made in terms of the spatially emerging order (S), which starts from random-like turbulent flows with a complex fine structure and ends up in almost equidistantly ordered rings. From the 3-D MHD simulations it appears that the Hall-shear instability (I) acts as a feedback mechanism to organize an initially “chaotic” axis-symmetric disk into an ordered system of bands. These properties (I,S) argue for a self-organization process (Table 1: qualifiers I,S).*

## 2.4. Jupiter's Red Spot

Jupiter exhibits a stable *Great Red Spot* since 187 years (or possibly since 350 years), which indicates a high-pressure zone of a persistent anticyclonic storm (Fig. 6). The vortex-like velocity field in Jupiter's Red Spot has been derived and rendered in Fig. (7) by Simon et al. (2014). The temperature of Jupiter's atmospheres above the Great Red Spot is measured to be hundreds of degrees warmer than simulations based on solar heating alone can explain (O'Donoghue et al. 2016). The Great Red Spot has a width of  $\approx 16,000$  km and rotates counter-clockwise with a period of  $\approx 3$  days. The longitude of the Great Red Spot oscillated with a 90-day period (Link 1975; Reese and Beebe 1977). Why can such an ordered, stable, long-lived structure exist in the (randomly) turbulent atmosphere of a gas giant? Why would it not decay into similar turbulent structures as observed in the surroundings? There exists a similar feature in Neptune's atmosphere, visible during 1989-1994, called the *Great Dark Spot*.

Early interpretations associated Jupiter's Great Spot with a Korteweg-de Vries soliton solution (Maxworthy and Redekopp 1976), a solitary wave solution to the intermediate-geostrophic equations (Nezlin et al. 1996), a Taylor column, a Rossby wave, or a hurricane (Marcus 1993). A geostrophic wind or current results from the balance between pressure gradients and Coriolis forces. One theoretical explanation that was put forward is the self-organization of vorticity in turbulence: The Jovian vortices reflect the behavior of quasi-geostrophic vortices embedded in an east-west wind with bands of uniform potential vorticity (Marcus 1993). Numerical simulations based on the quasi-geostrophic equations for a Boussinesq fluid in a uniformly rotating and stably stratified environment indicated the self-organization of the flow into a large population of coherent vortices (McWilliams et al. 1994). This scenario suggests an evolution from initial turbulent (random) to coherent (ordered) large-scale structures.

The vortex-solution of the Rossby wave equation gives not only a solution resembling of the Great Red Spot but is also similar to a drift soliton in plasma where the Coriolis force (in a rotating atmosphere) is replaced by the Lorentz force (in a magnetized plasma) (Petviashvili, 1980). The similarity of these phenomena not only indicates similar self-organizing principle behind them, but also may hint that the Great Dark Spot is the result of a MHD process.

*Critical Assessment: The argument of Jupiter's Great Red Spot being a self-organizing structure is mostly based on the emergence of a stable ordered large-scale structure (S), which is opposite to random-like turbulent small-scale structures. It is also the longevity of this large-scale structure that sets the Great Red Spot apart from short-lived small-scale turbulent structures. The physical process has been modeled with MHD simulations, essentially showing an inverse MHD turbulent cascade (from small to large scales), as it is known in 2-D turbulence (I). Thus, self-organization is established based on the properties I,S (Table 1: qualifiers I,S).*

## 2.5. Saturn's Hexagon

Saturn's north pole exhibits at  $77^\circ$  N a hexagonal cloud pattern that was first discovered in the 1980s by the Voyager mission (Godfrey 1988), which was later imaged with high resolution by the Cassini Orbiter (Baines et al. 2009). The images obtained by Cassini revealed that the structure consists of two elements: a hexagonal circumpolar jet-stream and a North Polar vortex (NPV), see Fig. (8). Recently, Rostami et al. (2017) showed by computational simulations that the cloud pattern can be described as a coupled dynamical system consisting of the hexagonal circumpolar jet-stream and the NPV, resulting in a self-organized stable hexagonal pattern. The hexagonal shape is formed in a specific region of the turbulent flow between the jet-stream and the NPV that rotate with different speeds; the hexagonal shape is stabilized by the NPV. The concentric ring structure surrounding the vortices at the north and south pole and their peculiar temperature distribution (Fletcher et al. 2008), the occurrence of auroras at the poles (Dyudina et al. 2016), as well as an electrodynamic coupling of Saturn with his moons, e.g. Enceladus (Pontius and Hill 2006;

Tokar et al. 2006), indicate that the cloud structures seem on the poles may be also related to plasma-physical and electrical phenomena. Indeed, laboratory studies of plasma discharge showed structures occurring at the diocotron instability (analogous to the Kelvin-Helmholtz instability in fluid mechanics) that resemble structures (discharge and cloud formations) at planetary poles (Parett et al., 2007).

*Critical Assessment: The argument of Saturn’s hexagon self-organizing structure is, as in the case of Jupiter’s Great Spot, mostly based on the emergence of a stable ordered large-scale structure (S), which is opposite to random-like turbulent small-scale structures. The modelling of the cloud structures based on fluid dynamics or plasma physics shows that instabilities (I) are involved in the organization process. The self-organization is thus established by properties I and S.*

## 2.6. Planetary Entropy

Random processes increase the entropy according to the second thermodynamic law, while self-organizing processes decrease the entropy, which is also expressed as an increase of negentropy (negative entropy). The entropy of a nonequilibrium system can be defined by the Gibbs formula,

$$dS = \frac{dE}{T} + \frac{pdV}{T}, \quad (9)$$

where  $dS$  is the entropy flux of an open system,  $E$  is the internal energy flux,  $T$  is the temperature,  $p$  is the pressure, and  $V$  is the volume. For planets, volume changes  $dV$  can be neglected. For energy balance one needs to include the solar radiation (or energy flux)  $E_s$  absorbed by the planet, and the infrared radiation (or energy flux)  $E_p$  emitted by the planet (Izakov 1997),

$$dE = E_s - E_p = f_s(1 - A)\pi r^2 - 4\pi r^2 f_p, \quad (10)$$

where  $f_s$  is the incident solar radiation per unit area (or irradiance),  $E_s$  is the incident energy flux from the Sun,  $E_p$  is the outgoing energy flux from the planet,  $f_p \approx \sigma_B T_e^4$  is the infrared radiation emitted from the unit area of the planet’s surface,  $T_e$  is the equilibrium temperature,  $A$  is the integral spherical albedo of the planet, and  $r$  is the radius of the planet. The average energy flux imbalance  $dE$  of the Earth at the top of the atmosphere is a crucial number characterizing the status of climate change. In practice, it is very difficult to measure the imbalance accurately. For the approach here, it is sufficient to note that it is found to be approximately zero. The energy flux balance of incoming and outgoing energy fluxes in the Earth’s atmosphere is depicted in Fig. (9) (energy flux imbalance numbers at lower left).

An interesting consequence of the energy flux balance  $dE \approx 0$  is the amount of negentropy flux that flows into a planet system. The difference of the entropy flux input from the Sun and the entropy flux output from the planet, representing the amount that goes into self-organization processes, can be estimated to be

$$dS = \frac{4}{3} \left( \frac{E_s}{T_s} - \frac{E_p}{T_p} \right), \quad (11)$$

which is found to be negative ( $dS < 0$ ) for energy flux balance  $E_p \approx E_s$  and blackbody equilibrium temperatures  $T_s \gg T_p$ , since the Sun is much hotter than the planet. In the following estimates we adapt nominal solar and terrestrial quantities from Prša (2016). Approximating with blackbody temperatures, we have  $T_s = 5772$  K for the Sun,  $T_p = 255$  K for the temperature of the Earth’s thermal radiation,  $f_s = 1361$  W m<sup>-2</sup> for the solar irradiance, and  $A = 0.29$  for the albedo, yielding a negentropy flux of  $-dS = 9 \times 10^{14}$  W K<sup>-1</sup>. The greenhouse effect, which yields a higher temperature of  $T_0 = 288$  K near the surface than the equilibrium temperature  $T_e = 255$  K, ensures the existence of water and the biosphere on the Earth. About 70% of the negentropy flux inflowing to Earth accounts for

the maintenance of the thermal regime on the planet. About 25% of the negentropy flux is spent on the evaporation of water, mostly from the surface of the oceans, supplying clouds and rainfall for the vegetation. Only a small fraction of about 5% goes into flows of mass and heat, tsunamis, hurricanes, etc. On Venus, where no water is, a larger fraction of negentropy flux goes into the dynamics of the atmosphere. Therefore, *the greenhouse effect, the hydrologic cycle of water, the global circulation of the atmosphere and oceans, are essentially dissipative structures supported by the supply of negentropy and making up the global self-organizing system whose characteristic is the climate on the Earth* (Izakov 1997).

Global energy flux budgets and *Trenberth diagrams* for the climates of terrestrial and gas giant planets are given in Read et al. (2016).

*Critical Assessment: Since the entropy flux is increasing in random processes, we can conclude that processes with decreasing entropy fluxes are non-random processes, which is one of the definitions of self-organization here. The entropy flux calculation of the Earth's atmosphere is made by assuming energy flux balance between the incoming solar radiation and the outgoing infrared emission from Earth. Based on this estimate of the entropy flux change (E) we can conclude that the atmosphere including its weather and climate changes have self-organizing capabilities (Table 1: qualifier E).*

### 3. SOLAR PHYSICS

#### 3.1. Photospheric Granulation

The solar photosphere exhibits a pattern of “bubbling” cells (like boiling water in a frying pan), which is called “photospheric granulation” (Fig. 10) and has been interpreted in terms of hydrodynamic convection cells. The central part of a granulation cell is occupied with upflowing plasma, which then cools down and descends in the surrounding edges, which consequently appear to be darker than the center, because a cooler temperature corresponds to fainter white-light emission. The photospheric temperature is  $T_s = 5780$  K, the typical size of a granule is  $w \approx 1500$  km, and the life time is about 8-20 min.

The underlying physical mechanism of convection has been studied in great detail in terms of the Rayleigh-Bénard instability, known as Lorenz model (Lorenz 1963), described also in the monographs of Chandrasekhar (1961) and Schuster (1988). The basic ingredients of the (hydrodynamic) Lorenz model are the Navier-Stokes equation, the equation for heat conduction, and the continuity equation,

$$\rho \frac{d\mathbf{v}}{dt} = \mathbf{F} - \nabla p + \mu \nabla^2 \mathbf{v} \quad (12)$$

$$\frac{dT}{dt} = \kappa \nabla^2 T \quad (13)$$

$$\frac{d\rho}{dt} = -\nabla \cdot (\rho \mathbf{v}) \quad (14)$$

where  $\rho$  is the density of the fluid,  $\mu$  is the viscosity,  $p$  is the pressure,  $\kappa$  is the thermal conductivity,  $\mathbf{F} = -\rho g \mathbf{e}_z$  is the external force in the  $e_z$  direction due to gravity, and the boundary conditions are  $T(x, y, z = 0, t) = T_0 + \Delta T$  and  $T(x, y, z = h) = T_0$  for a temperature gradient in vertical direction. For the special case of translational invariance in  $y$ -direction, using the Boussinesq approximation, and retaining only the lowest order terms in the Fourier expansion, we obtain the much simpler form of the Lorenz model,

$$\begin{aligned} \dot{X} &= -\sigma X + \sigma Y \\ \dot{Y} &= -XZ + rX - Y \quad , \\ \dot{Z} &= +XY - bZ \end{aligned} \quad (15)$$

which is a system of three coupled first-order differential equations, with  $X$  the circulatory fluid flow velocity,  $Y$  the temperature difference between ascending and descending fluid elements,  $Z$  the deviations of the vertical temperature profile from its equilibrium value, and  $r$  is the control parameter measuring the magnitude of the temperature difference  $\Delta T$ . The Lorenz model can describe the transition from heat conduction to convection rolls, where Lorenz discovered the transition from deterministic to chaotic system dynamics.

Thus, the Lorenz model demonstrates that a temperature gradient (for instance below the photosphere) transforms (a possibly turbulent) random motion into a highly-organized rolling motion (due to the Rayleigh-Bénard instability) and this way organizes the plasma into nearly equi-sized convection rolls that have a specific size (such as  $w \approx 1500$  km for solar granules). The self-organization process thus creates order (of granules with a specific size) out of randomness (of the initial turbulent spectrum).

Since convection is the main energy transport process inside the Sun down to  $0.7R_\odot$ , larger convection rolls than the granulation pattern can be expected. Krishan (1991, 1992) argues that the Kolmogorov turbulence spectrum  $N(k) \propto k^{-5/3}$  extends to larger scales and possibly can explain the observed hierarchy of structures (granules, mesogranules, supergranules, and giant cells) by the same self-organization process.

At smaller scales, a subpopulation of mini-granular structures has been discovered, in the range of  $w \approx 100 - 600$  km, (Fig. 11), predominantly confined to the wide dark lanes between regular granules, often forming chains and

clusters, but being different from magnetic bright points (Abramenko et al. 2012). A set of TiO images of solar granulation acquired with the 1.6 meter New Solar Telescope at Big Bear Solar Observatory was utilized. The high-contrast speckle-reconstructed images of quiet-sun granulation (Fig. 11), allowed to detect, besides the regular-size granules, the small granular-like features in dark inter-granular lanes, named as *mini-granules*. Mini-granules are very mobile and short-lived. They are predominantly located in places of enhanced turbulence and close to strong magnetic fields in inter-granular lanes. The equivalent size of detected granules was estimated from the circular diameter of the granula’s area. The resulting *probability density functions (PDF)* for 36 independent snapshots are shown in gray on the left frame of Fig. (12). The average PDF (the red histogram) changes its slope in the scale range of  $\approx 600 - 1300$  km. This varying power law PDF is suggestive that the observed ensemble of granules may consist of two populations with distinct properties: regular granules and mini-granules. A decomposition of the observed PDF showed that the best fit is achieved with a combination of a power law function (for mini-granules) and a Gaussian function (for granules). Their sum fits the observational data. Mini-granules do not display any characteristic (“dominant”) scale. This non-Gaussian distribution of sizes implies that a more sophisticated mechanism with more degrees of freedom may be at work, where any small fluctuation in density, pressure, velocity and magnetic field may have significant impact and affect the resulting dynamics. It is worth to note that a recent direct numerical simulation attempt (Van Kooten and Cranmer 2017) produced the PDF of granular size in agreement with the observed one in Fig. (12). The authors concluded that the population of mini-granules is intrinsically related to non-linear turbulent phenomena, whereas Gaussian-distributed regular granules originate from near-surface convection.

*Critical Assessment: The size distribution of granulation cells in the solar photosphere does not form a power law distribution, but clearly shows a preferred spatial scale of  $\approx 1000$  km, which renders a regular spatial pattern (S), rather than a scale-free distribution. However, a power law distribution has been found for the newly discovered “mini-granules” in a size range of 100-600 km, which contradicts a self-organizing convective process that creates bubbles of equal sizes. The physical process of convection that is driven by a temperature gradient and the Rayleigh-Bénard instability (I) is well-understood and known as the Lorenz model. A caveat is how much the magnetic field plays a role in the solar convection zone, requiring a model with magneto-convection and hydromagnetic (Parker and Kruskal-Schwarzschild) instabilities. Anyway, a self-organization process is warranted based on the preferred scale of convective rolls (Table 1: qualifiers I,S).*

### 3.2. Magnetic Field Self-Organization

How is the solar magnetic field organized and how does the resulting magnetic field self-organize into stable structures? It is said that sunspots and pores represent the basic stable structures that are visible in the photosphere, but their sub-photospheric formation (driven by the solar dynamo) and stability are long-standing problems. In the following we discuss a few papers that explicitly use the term “self-organization” in this context.

Takamaru and Sato (1997) propose a self-organization system that evolves intermittently and undergoes self-adaptively local maxima and minima of energy states. The nonlinear interactions of twisting multiple flux tubes lead to local helical kink instabilities, resulting in the formation of a knotted structure. Intermittent reconnection with neighbored flux tubes in the knotted structure releases energy and restores the original configuration, a process that exhibits self-organization in an open complex nonlinear system where energy is externally and continuously supplied.

Vlahos and Georgoulis (2004) state that non-critical self-organization appears to be essential for the formation and evolution of solar active regions, since it regulates the emergence and evolution of solar active regions, perhaps characterized by a percolation process (Schatten 2007; 2009), while the energy release process is governed by self-organized criticality. Georgoulis (2005, 2012) explores various (scaling and multi-scaling, fractal and multi-fractal)

image-processing techniques to measure the expected self-organization of turbulence in solar magnetic fields. However, no difference was found in the turbulence spectrum between flaring and non-flaring active regions.

Chumak (2007) proposes a dynamic self-organization model of the active region evolution in terms of a diffuse aggregation process of magnetic flux tubes in the upper levels of the solar convection zone. The physical model is governed by hydrodynamics, magnetic forces, and additional random forces.

Kitiashvili et al. (2010) describes the process of magnetic field generation as a self-organization process: *The simulations reveal two basic steps in the process of spontaneous formation of stable structures that are the key for understanding the magnetic self-organization of the Sun and the formation of pores and sunspots: (1) formation of small-scale filamentary magnetic structures associated with concentrations of vorticity and whirlpool-type motions, and (2) merging of these structures due to the vortex attraction, caused by converging downdrafts around magnetic concentration below the surface, reaching magnetic field strengths of  $B \approx 1500$  G at the surface and  $B \approx 6000$  G in the interior. The structure was found to remain stable for at least several hours. Examples of the simulated formation and evolution of magnetic structures are shown in Fig. (13).*

Although the term “self-organization” is not explicitly mentioned in recent (realistic) radiative 3-D MHD simulations of Abbett (2007), Cheung et al. (2007), Martinez-Sykora et al. (2008, 2009, 2011), Tortosa-Andreu and Moreno-Insertis (2009), Stein et al. (2011), Stein (2012), and Rempel and Cheung (2014), we can interpret the generation of stable coherent magnetic structures in the turbulent convection zone as a manifestation of a self-organizing process. Basically, these global MHD dynamo models generate coherent flux ropes that rise towards the solar surface (Fig. 14). There is no need to insert sub-photospheric flux ropes in the simulation box as done earlier, because recent 3-D MHD simulations added the evolution of realistic magneto-convection as a time-dependent boundary to drive the flux emergence process (Cheung and Isobe 2014; Cheung et al. 2017). The fact that sunspots always appear within a time scale comparable to the flux emergence time of an active region, providing magnetic flux to the sunspot, indicates that coherent magnetic structures self-organize deep in the convection zone. There the Rossby number is less than unity and convection is constrained by differential rotation and meridional flows.

As a disclaimer, we have to be aware that these 3-D MHD simulations capture a local box only, rather than being global. A self-consistent generation of magnetic flux, simulated on a global scale that includes the entire spherical convection zone of the Sun, is presented in Miesch et al. (2000), which produces laminar and turbulent states, driven by the differential solar rotation. Related work describes convection and dynamo action in rapidly rotating suns (Brown et al. 2010), or in large-scale dynamos with turbulent convection and shear (Käpylä et al. 2012). In order to understand the basic mechanism of the formation of magnetic flux concentrations, numerical 3-D MHD simulations were performed that study the turbulence contributions to the mean magnetic pressure in a strongly stratified isothermal layer with a large plasma beta (Brandenburg et al. 2012). By applying a weak uniform horizontal mean magnetic field, the *negative effective magnetic pressure instability (NEMPI)* is activated, which reduces the turbulence and thus the turbulent pressure. If this reduction is more than the magnetic pressure, then the weakly magnetized region will have a reduced total pressure, which leads to a collapse of the field into a stronger tube. Since this mechanism generates order from turbulence, it can be considered to be a self-organizing process (Robert Cameron, private communication). In the global 3-D MHD simulations of Hotta et al. (2015), an efficient small-scale dynamo generates the magnetic field, which has a feedback on the poleward meridional flows, and thus displays the characteristic feedback feature of a self-organizing process. A simulation of the convective dynamo in the solar convective envelope has been conducted by Fan and Fang (2014), which is driven by the solar radiative diffusive heat flux, exhibiting irregular cyclic behavior with oscillation time scales ranging from about 5 to 15 yr and undergoes irregular polarity reversals, as it is typical for self-organizing limit cycles far off a stationary equilibrium.

*Critical Assessment: Ideas of applying self-organization processes to generate the magnetic field in the solar con-*

vection zone or in the solar corona are mentioned only briefly in the reviewed papers (or not at all), but no quantitative models or measurements are presented that would allow us to discriminate which magnetic structures have a random pattern and which ones exhibit some ordered pattern. The magnetic flux on the solar surface was found to have a power law size distribution (Parnell et al. 2009), which is rather consistent with a self-organized criticality process. The envisioned feedback mechanisms include the kink instability, the NEMPI instability, percolation, diffuse aggregation, and vortex attraction, but none of these processes has been characterized in emerging flux simulation in terms of self-organization. So, we can observe spatial patterns of photospheric magnetic flux patches (S), but are not sure which instability (I) enacts self-organization (Table 1: qualifiers I(?),S).

### 3.3. The Hale Cycle

The global magnetic field of the Sun undergoes a cyclic transition from a global poloidal field to a highly-stressed toroidal field in 11 years, switching the magnetic polarity during this process, so that the original polarity is restored after two cycles, yielding a 22-yr cycle that is called the (magnetic) ‘‘Hale cycle’’. There exist over 2000 publications about the solar magnetic activity cycle. A recent review can be found in Hathaway (2015).

A physical model of the Hale Cycle is the Babcock-Leighton dynamo model (Babcock 1961; for a review see Charbonneau 2014), which explains the winding-up of the highly-stressed toroidal field as a consequence of the differential rotation (during the rise phase of the cycle), and is followed by a gradual decay with decreasing sunspot number and meridional diffusion of the magnetic field, leading to a relaxed poloidal field during the solar cycle minimum. An example of a 3-D MHD simulation of the solar convection zone is shown in Fig. (15). The observed variation of the sunspot number between the years 1870 and 2017 is shown in Fig. (16).

The variability of the solar cycle can be understood in terms of a weakly nonlinear limit cycle affected by random noise (Cameron and Schüssler 2017), quantified in normal form in terms of the Hopf bifurcation (Fig. 17, 18, Appendix C). The presence of a limit cycle is a common property in coupled nonlinear dissipative systems, which is most easily understood in terms of the Lotka-Volterra equation system (Haken 1983), known as the predator-prey equation in ecology (Fig. 18 bottom; Appendix D),

$$\begin{aligned}\dot{X} &= k_1 X - k_2 XY \\ \dot{Y} &= -k_3 Y + k_2 XY\end{aligned}\tag{16}$$

This equation system has a periodic solution, which is called the limit cycle. Critical points occur when  $dX/dt = 0$  and  $dY/dt = 0$ , which yields a stationary point in phase space at  $X = k_3/k_2$  and  $Y = k_1/k_2$ . Applying the Lotka-Volterra equation system to the solar cycle,  $X$  represents the poloidal field and  $Y$  the toroidal field,  $k_1$  the growth rate of the poloidal field,  $k_3$  the growth rate of the toroidal field, and  $(k_2)$  a nonlinear interaction term between the two field components. The Lotka-Volterra equations describe the emergence and sustained oscillation in an open system far from equilibrium, as well as emergence of spontaneous self-organization (Demirel 2007). An application of the Lotka-Volterra system to the complex system of the solar cycle is discussed in Consolini et al. (2009), where a double dynamo mechanism is envisioned, one at the base of the convection zone (tachocline), and a shallow subsurface dynamo. The deeper dynamo dominates the poloidal field, while the shallower dynamo controls the toroidal field. In summary, the limit cycle represents a highly-ordered self-organizing 11-year (22-year) pattern of the solar magnetic activity, which cannot be explained with a random process.

A chaotically modulated stellar dynamo was modeled also based on bifurcation theory, where modulation of the basic magnetic cycle and chaos occur as a natural consequence of a star that is in transition from a non-magnetic state to one with periodically reversing fields (Tobias et al. 1995).

*Critical Assessment:* The solar cycle is a very periodic phenomenon with little variation in each cycle, which

is a classic example of a nonlinear dissipative system with limit-cycle behavior (LC), such as the Hopf bifurcation (Appendix C) or Lotka-Volterra equation system (Appendix D). The limit cycle produces a regular temporal pattern (T), and the cycle variation modulates the magnetic flux and area on the solar surface like-wise (S). The physics of the solar cycle is also well-understood in terms of the Babcock-Leighton model, where the differential solar rotation is the driver, and a twisted magnetic field relaxation mechanism acts as the feedback mechanism. The underlying instability still needs to be identified and may depend on both the shallow dynamo or the deep dynamo in the tachocline at the bottom of the convection zone (Table 1: qualifiers LC,I[?],S,T).

### 3.4. Evaporation-Condensation Cycles

Solar observations show that coronal loops routinely harbor flows that result from the complex physics of the solar transition region (e.g., Peter et al. 2006). Upflows can generally be understood as the result of heated plasma from the chromosphere ascending into coronal loops (chromospheric evaporation), as modeled from EUV, soft X-ray, and hard X-ray observations. These upflows frequently happen during solar flares, but equally occur as a consequence of other coronal heating mechanisms also, in active regions, in Quiet Sun regions (explosive events, EUV brightenings), and even in coronal holes (plumes, jets). At the same time there is numerous evidence for downflows, also called “coronal rain” or “coronal condensation”, mostly observed in H $\alpha$  (first reported by Leroy 1972) and UV lines of cooler temperatures (Schrijver et al. 2001; De Groof et al. 2005). The combined pattern of upflows and downflows is also referred to as “evaporation-condensation cycle” (Krall and Antiochos 1980), which we consider under the aspect of a self-organization process here.

The earliest physical interpretation of evaporation-condensation cycles has been modeled in terms of the thermal instability, which constitutes a chromosphere-corona coupling or feedback mechanism between the heating rate and the cooling rate in a coronal loop (Kuin and Martens 1982). Such a system can exhibit a stable static equilibrium if the coupling between the chromosphere and the corona is sufficiently strong, but for typical coronal loop conditions the system is expected not to be stable, resulting into a cyclic solution that corresponds to the limit cycle of a coupled nonlinear system. The physical model predicts that a temporal excess of heating leads to an excess conductive flow at the loop base, which results into chromospheric evaporation with increasing pressure and density, and in turn amplifies the radiative loss, leading to a thermal (or radiative) instability with subsequent condensation or downflow of cool material. Kuin and Martens (1982) use the following form of the hydrodynamic equations for a 1D loop,

$$\frac{\partial n}{\partial t} = -\frac{\partial}{\partial z}(nv) \quad (17)$$

$$\frac{dv}{dt} = -\frac{2}{m_H n} \frac{\partial p}{\partial z} - g_{\parallel} \quad (18)$$

$$\frac{3}{2} \frac{dp}{dt} = -\frac{5}{2} \frac{\partial v}{\partial z} - \frac{\partial}{\partial z} \left[ \kappa_0 T^{5/2} \frac{\partial T}{\partial z} \right] + E_H - n^2 \Psi(T) \quad (19)$$

$$p = nk_B T = \mu m_H n c_s^2 \quad (20)$$

where  $p$  is the pressure,  $n$  the particle density,  $v$  the plasma velocity,  $T$  the electron temperature,  $t$  the time,  $k_B$  the Boltzmann constant,  $m_H$  the hydrogen mass,  $g_{\parallel}$  the gravitational acceleration along the loop,  $c_s$  the isothermal sound speed,  $\mu = 0.5$  the molecular weight,  $\kappa_0$  the Spitzer conductivity,  $E_H$  the heating rate (assumed to be spatially constant), and  $\Psi(T)$  is the radiative loss function (approximated with a power law  $\Psi(T) = \Psi_0 T^{-\gamma}$ ). Kuin and Martens (1982) find static solutions for some parameters of the loop length  $L$  and heating rates  $E_H$ . The time-dependent solutions can be approximated by the following coupled equation system for the dimensionless temperature

$X = T/T_0$  and density  $Y = n_e/n_0$  parameters,

$$\frac{dX}{dt} = \frac{1}{Y} [1 - Y^2 \Psi(X) - \alpha(X - 1)] \quad (21)$$

$$\frac{dY}{dt} = f\alpha(1 - X^{-1}) \quad (22)$$

Similar to the Lotka-Volterra equation system (Eq. 16), this rate equation system has a limit cycle at the critical point  $dX/dt = 0$  and  $dY/dt = 0$ , requiring  $f\alpha(1 - X^{-1}) = 0$  and  $[1 - Y^2 \Psi(X) - \alpha(X - 1)]/Y = 0$ , which yields the solution  $X = 1$  and  $Y = 1/\sqrt{\Psi(X = 1)}$  for the limit cycle at the attractor point. The X-Y phase diagram of some quasi-stationary solutions is shown in Fig. (19).

Numerical 1-D hydrodynamic simulations of the condensation of plasma in loops of wide ranges of lengths and temperatures ( $10 \text{ Mm} \leq L \leq 300 \text{ Mm}$ ;  $0.2 \text{ MK} \leq T \leq 2 \text{ MK}$ ) reproduce the cyclic pattern, starting with chromospheric evaporation, followed by coronal condensation, then motion of the condensation region to either side of the loop, and finally loop reheating with a period of 1h to 4 days (Müller et al. 2003, 2004, 2005). It is found that the radiatively-driven thermal instability occurs about an order of magnitude faster than the Rayleigh-Taylor instability, which can occur in a loop with a density inversion at its apex also (Müller et al. 2003). Simulations with different heating functions reveal that the process of catastrophic cooling is not initiated by a drastic decrease of the total loop heating rate, but rather results from a loss of equilibrium at the loop apex as a natural consequence of quasi-steady footpoint heating (Müller et al. 2004; Peter et al. 2012). The same effect of a loss of equilibrium can occur in the case of repetitive impulsive heating (e.g., Mendoza-Briceno et al. 2005; Cargill et al. 2013).

EUV intensity pulsations with periods from 2 to 16 hrs have been discovered to be quite common in the solar corona and especially in coronal loops (Auchère et al. 2014; Froment et al. 2015). The three loop events shown in Fig. (20), studied in detail by Froment et al. (2015), have time periods of 3.8, 5.0 and 9.0 hrs and are lasting over several days. They were interpreted in terms of thermal non-equilibrium evaporation and condensation cycles (Froment et al. 2015, 2017). In Fig. (20) the temperature and the total emission measure are shown, extracted from a DEM analysis using the method developed by Guennou et al. (2012,a,b; 2013). The temperature corresponds to the peak temperature of the DEM, and the total emission measure is proportional to the squared density along the line-of-sight.

Uzdensky (2007a,b) proposes a similar self-organization process for coronal heating. This self-regulating process keeps the coronal plasma roughly marginally collisionless. The driver of the self-organization process is the magnetic reconnection in the collisional Sweet-Parker regime. The feedback mechanism is the inhibition of magnetic reconnection triggered by density increases due to chromospheric evaporation. After some time, the conductive and radiative cooling lowers the density again below the critical value and fast reconnection sets in again. Thus, the self-organization process is made of repeating cycles of fast reconnection, evaporation, plasma cooling, and re-building of magnetic stress. A similar self-regulation mechanism controlled by marginal collisionality in magnetic reconnection is explored in Cassak et al. (2008) and Imada and Zweibel (2012). The cyclic behavior has been simulated with a 1-D hydrodynamic model that is driven by gravity and the density dependence of the heating function (Imada and Zweibel 2012).

*Critical Assessment:* The evaporation-condensation scenario of coronal loops predicts a quasi-periodic time pattern, but not much is known about the degree of periodicity, and whether this corresponds to a quasi-periodic self-organizing limit cycle. The quasi-periodic patterns discovered by Froment et al. (2015, 2017), which exhibit phase-shifted oscillations between the emission measures and temperatures in active regions, reveal large fluctuations in the emission measure versus temperature diagram (Fig. 20), which may indicate strong nonlinearities near the limit cycle or inadequate background subtraction in the differential emission measure analysis. Although the physics of the evaporation-condensation cycle is well understood, to deduce the time evolution of the heating rate, electron density,

and temperature from observational data, adequate background subtraction needs to be performed in order to establish whether the observations are well described by a limit-cycle system (Table 1: qualifiers I,LC[?],T[?]).

### 3.5. Quasi-Periodic Radio Bursts

We identify more than 150 publications that report or model periodic (oscillatory) or quasi-periodic solar radio bursts. Many of these quasi-periodic solar radio emissions are believed to be generated by various plasma instabilities (Benz 1993). The degree of periodicity was found to vary from random to strictly periodic (e.g., Aschwanden et al. 1993). In an early review, solar radio pulsations were classified into three different models: (1) MHD oscillation eigenmodes; (2) cyclic self-organizing systems; and (3) modulation of magnetic reconnection, particle injection, or acceleration (Aschwanden 1987). Here we discuss only the second group in terms of self-organization mechanisms, which observationally can be easily distinguished from the first group: MHD oscillations are strictly periodic, while limit cycles in self-organizing systems produce less regular quasi-periodic pulse patterns. We have also to be aware that the periodicity of solar radio bursts can only be inferred from time profiles (Figs. 21, 22), while spatial fine structures mostly cannot be resolved by *remote-sensing* observations with current radio instruments.

Self-organizing systems with limit cycles were initially applied to loss-cone instabilities occurring in the aurora, where two types of waves (electrostatic and upper hybrid waves) exchange energy in a limit cycle, driven by the loss-cone instability (Trakhtengerts 1968), a concept that was then applied to solar radio pulsations also (Zaitsev 1971; Zaitsev and Stepanov 1975; Kuijpers 1978; Bardakov and Stepanov 1979; Aschwanden and Benz 1988). The two-component nonlinear systems of self-organization are controlled either by wave-wave interactions, or by wave-particle interactions (also called a *quasi-linear diffusion* process).

The process starts with the development of a nonthermal particle distribution (such as electron beams, loss-cones, pancakes, or rings), which then become unstable and transform kinetic energy into various waves (such as whistler waves, upper-hybrid waves, Langmuir waves, or electron-cyclotron maser emission), relaxing the unstable particle distribution then (in form of a plateau for beams or a filled loss-cone). After this feedback, when new particles arrive, the relaxed particle distribution becomes unstable again and the entire nonlinear cycle starts over. For the case of electron-cyclotron emission, for instance, the dynamics of the wave-particle interaction can be described by the following system of coupled equations (e.g., Aschwanden and Benz 1988),

$$\frac{\partial N(\mathbf{k}, t)}{\partial t} + \mathbf{v}_g(\mathbf{k}) \frac{\partial N(\mathbf{k}, t)}{\partial \mathbf{r}} = \Gamma(\mathbf{p}, \mathbf{k}, f)N(\mathbf{k}, t) - \gamma(\mathbf{p}, \mathbf{k}, f)N(\mathbf{k}, t), \quad (23)$$

$$\frac{\partial f(\mathbf{p}, t)}{\partial t} + \mathbf{v}(\mathbf{p}) \frac{\partial f(\mathbf{p}, t)}{\partial \mathbf{p}_j} = \frac{\partial}{\partial j} \hat{D}_{ji}(\mathbf{p}, \mathbf{k}, N) \frac{\partial f(\mathbf{p}, t)}{\partial p_i} + \frac{\partial f(\mathbf{p}, f)}{\partial t} \Big|_{source} + \frac{\partial f(\mathbf{p}, f)}{\partial t} \Big|_{loss}, \quad (24)$$

where the waves are represented by the photon number density  $N(\mathbf{k}, t)$  in  $\mathbf{k}$ -space, the particle system is described by its density distribution  $f(\mathbf{p}, t)$  in momentum space,  $\Gamma(\mathbf{p}, \mathbf{k}, f)$  is the wave growth rate,  $\gamma(\mathbf{p}, \mathbf{k}, f)$  is the wave damping rate,  $\mathbf{v}_g(\mathbf{k})$  is the group velocity of the emitted waves, and  $\hat{D}_{ji}(\mathbf{p}, \mathbf{k}, N)$  is the quasi-linear diffusion tensor. Eq. (23) is the wave equation that describes the balance between emission and growth and damping rate, while Eq. (24) describes the evolution of the particle distribution. The interaction between waves and particles is expressed by the quasi-linear diffusion tensor. In addition, there is a source term of particles (with large pitch angles), as well as a loss term (which quantifies the precipitating particles with small pitch angles out of the loss-cone.)

A complete analytical solution of this coupled integro-differential equation system is not available, but a limit-cycle solution applied to the case of electron-cyclotron maser emission has been calculated (Aschwanden and Benz 1988). The pulse period  $\tau_{lc}$  of the limit cycle has been found to be the geometric mean of the wave growth time  $\tau_g$

and the particle diffusion time  $\tau_d$ ,

$$\tau_{lc} = 2\pi\sqrt{\tau_g\tau_d}, \quad (25)$$

which is a close analogy to the limit cycle of the Lotka-Volterra equation system (Eq. 16 and Appendix D) or a coupled differential equation system (Appendix B). In summary, such a self-organizing system is driven by coherent wave growth stimulated by an unstable (loss-cone) particle distribution via the relativistic (cyclotron or gyro-magnetic Doppler resonance condition), while the feedback mechanism represents the back reaction that flattens the unstable particle distribution (via quasi-linear diffusion), which in turn quenches coherent wave growth until the loss-cone is filled again with new particles and the cyclic wave-particle interaction starts over. The result is a stationary quasi-periodic pattern of coherent radio emission, which is strictly periodic in the limit cycle only, but becomes aperiodic depending on the inhomogeneity, anisotropy, time-dependence, and noise of the control parameters. Dabrowski and Benz (2009) find generally a good correlation between decimetric pulsations and hard X-rays.

*Critical Assessment: The quasi-periodicity of solar radio bursts as observed in dynamic spectra is the most convincing signature of a self-organizing process, in contrast to a time series with random time intervals, as it would be expected for self-organized criticality models. The spatial counterpart (S) of the quasi-periodic temporal scales (T) is generally not observed due to the lack of radio images with high spatial resolution. Nevertheless, quasi-periodic time intervals are consistent with a limit cycle (LC) of a nonlinear dissipative system, but there are many plasma instabilities that can operate as a positive feedback mechanism, either in terms of wave-particle interactions (e.g., loss-cone or beam instabilities), or wave-wave interactions. Thus, more data modeling, possibly with high-resolution imagery and magnetic field modeling is required to identify the relevant instabilities that control a self-organizing process in the generation of quasi-periodic radio bursts (Table 1: qualifiers T, LC, I[?]).*

### 3.6. Zebra Radio Bursts

While the existence of self-organizing systems observed in solar radio bursts is mostly inferred from the quasi-periodicity of observed temporal patterns, there exists another category of solar radio bursts that exhibits very regular periodic patterns in the frequency domain. The most striking example is the so-called *zebra burst* (Fig. 23), which reveals drifting parallel bands of quasi-stationary radio emission with harmonic frequency ratios. Theoretical interpretations include (i) models with interactions between electrostatic waves and whistlers, and (ii) radio emission at the double-plasma resonance (Kuijpers 1975, 1980; Zheleznykov and Zlotnik 1975a,b; Mollwo 1983; Winglee and Dulk 1986; Chernov 2006; Chen et al. 2011),

$$\omega_{UH} = (\omega_{Pe}^2 + \omega_{Be}^2)^{1/2} = s \omega_{Be}, \quad (26)$$

where  $\omega_{UH}$  are upper hybrid waves,  $\omega_{Pe}$  is the electron plasma frequency,  $\omega_{Be}$  is the electron cyclotron frequency, and  $s$  is the integer harmonic number, which introduces a periodic pattern in the resonance frequency. If the magnetic field structure  $B(h)$  with altitude  $h$  is known, the harmonic frequencies can be mapped onto a periodic spatial pattern (Fig. 23, right panel). Either way, harmonic resonances (of the gyrofrequency) create order out of randomness for this type of radio bursts, in analogy to mechanical resonances that produce harmonic patterns of planet orbits.

In recent models, the double-plasma resonance mechanism faces a number of difficulties in explaining the dynamics of zebra stripes (i.e., sharp changes of the frequency-drift rate, a large number of stripes, frequency splitting of stripes, super-fine millisecond structure), because the magnetic field and density cannot change as rapidly. Improved models are in progress (Karlicky et al. 2001; LaBelle et al. 2003; Kuznetsov and Tsap 2007; Karlicky and Yasnov 2015). New calculations concern the increments of the upper-hybrid waves under double-plasma resonance conditions, the ring distribution of high-speed electrons with relativistic corrections, different temperatures of the background plasma, and optimum wave numbers (Benacek et al. 2017). It has been shown that the optimum increment for

electron velocities is  $v \approx 0.1 c$ , with a narrow dispersion. If the speed is  $\approx 0.2 c$ , the increment sharply decreases and the flux maxima are washed out in the continuum for several cyclotron harmonic numbers  $s$ . Thus, these calculations show the inefficiency of the double-plasma resonance mechanism. Under such conditions it becomes clear, that the double-plasma resonance mechanism cannot explain the majority of zebra stripes. An additional complication is the simultaneous occurrence of decimetric millisecond spikes.

In the whistler model, all the aforementioned properties of zebra burst stripes have been explained by physical processes that occur during the coalescence of Langmuir waves ( $l$ ) with whistler waves ( $w$ ), producing transverse waves,  $l + w \mapsto t$  (Kuijpers, 1975; Chernov 1976; 1990; 2006; 2011). Langmuir waves and whistlers can be generated by the same fast particles trapped in magnetic islands (Berney and Benz, 1978).

The spatial structure of zebra radio bursts is believed to originate in magnetic islands after coronal mass ejections. Therefore the close connection of zebra bursts with fiber bursts is simply explained by the acceleration of fast particles in magnetic reconnection regions in the lower or upper part of magnetic islands.

A wavelike or saw-tooth frequency drift of stripes was explained by the switching of the whistler instability from the normal Doppler-cyclotron resonance into the anomalous one (Fig. 2b in Chernov 1990). Such switching should lead to a synchronous change of the frequency drift of stripes and spatial drift of the radio source, since whistlers generated at normal and anomalous resonances move in opposite directions. New injections of fast particles cause sharp changes in the frequency drift rate and oscillation pattern of zebra stripes. Low frequency absorption (i.e., black stripes of zebra bursts) are explained by quenching of the plasma wave instability due to diffusion of fast particles by whistler waves.

The superfine structure is generated by a pulsating regime of the whistler instability with ion-sound waves (Chernov et al. 2003). Rope-like chains of fiber bursts are explained by a periodic whistler instability between two fast shock fronts in a magnetic reconnection region (Chernov 2006). In the whistler model, zebra-stripes can be converted into fiber bursts and back (Fig. 24), which exhibits morphological changes from chaos to order, and in reverse direction. A comparative discussion of observations of zebra and fiber bursts and different theoretical models can be found in the reviews of Chernov (2012; 2016).

*Critical Assessment: The most striking pattern that hints to a self-organization process is the periodic appearance of bands in dynamic spectra of some solar radio bursts, which is interpreted in terms of gyroharmonic resonances (R). In principle, a periodic pattern in radio frequency can be mapped to a periodic pattern in spatial structures (S), using the plasma frequency relationship  $f_p \propto \sqrt{n_e}$  and a density model  $n_e(h)$  as a function of the altitude  $h$ , while there is no obvious periodic pattern of temporal structures (T) expected. The driver mechanism that produces zebra bursts is likely to be a population of nonthermal particles, while the counter-acting feedback mechanism has been modeled in terms of electrostatic waves, whistler waves, or the double-plasma resonance. The observational verification of any of these wave types is still very challenging with remote-sensing techniques (Table 1: qualifiers R,S,I[?] ). — Note that the spatial pattern of a zebra skin has also been classified as a self-organization process in biology (e.g., Camazine et al. 2001), where the light and dark pigmentation is created by the diffusive interaction of chemical activation (driver) and inhibition (feedback) during the embryonic development.*

## 4. STELLAR PHYSICS

### 4.1. Star formation

The spatial distribution of star formation in a galaxy is not uniform but is concentrated in a number of small localized areas in galaxies. Young stellar associations with their H II regions and molecular clouds (Fig. 25) are manifestations of the ordered distribution of matter participating in the star formation processes, governed by self-organization in a nonequilibrium system (Bodifée 1986). A star formation region can be modeled by the following system of coupled equations (Bodifée 1986):

$$\frac{dA}{dt} = K_1 S + K_2 S - K_3 M^2 A \quad (27)$$

$$\frac{dM}{dt} = K_3 M^2 S - K_4 S M^n \quad (28)$$

$$\frac{dS}{dt} = K_4 S M^n - K_1 S - K_2 S \quad (29)$$

$$\frac{dR}{dt} = K_1 S, \quad (30)$$

where  $A$  is the mass of the interstellar atomic gas,  $M$  is the mass of the interstellar molecular gas (with dust),  $S$  is the mass of the stellar material (young stars with their associated H II regions),  $R$  represents the total mass of “old” stars (stellar remnants and low-mass main-sequence stars), and  $n$  is a stability parameter. (Stability is granted for  $n \geq 2$  for any  $[k_1, k_2]$  pair, see Fig. 3 in Bodifée 1986). A graphic representation of the star formation process is depicted in Fig. (26). This coupled system of differential equations, after elimination of  $S$  and the introduction of dimensionless variables, can be simplified to

$$\frac{da}{d\tau} = 1 - a - m - k_1 m^2 a \quad (31)$$

$$\frac{dm}{d\tau} = k_1 m^2 a - k_2 m^n + k_s m^n a + k_2 m^{n+1}, \quad (32)$$

where  $a$  is the fractional mass of atomic gas,  $m$  is the fractional mass of molecular gas,  $\tau = (K_1 + K)t$  is a dimensionless time variable,  $k_1$  is the efficiency of production of molecules, and  $k_2$  is the efficiency of triggered star formation. It is found that this coupled equation system has three stationary states, two of them trivial (all mass contained in either atomic or molecular gas), and a non-trivial stationary solution (Bodifée 1986). The latter solution is not necessarily stable against perturbations, but can evolve into a limit-cycle oscillation, constrained by the conditions  $da/d\tau = 0$  and  $dm/d\tau = 0$  in Eqs. (31-32). Near the limit cycle, the oscillation is maintained without an external periodic driving force, producing repetitive violent bursts of star formation, separated by long quiescent periods. Similar limit-cycle solutions were found by Ikeuchi and Tormita (1983), where supernova remnants control the hot, warm, and cold gas, and a diffusion transport term is added. The main spatial manifestation of this self-organizing mechanism is the spiral structure of galaxies, in analogy to rotating spiral vortices formed in chemical auto-catalytic oscillations (Zaikin and Zhabotinsky 1970; Winfree 1972, 1973; Cox et al. 1985).

Subsequent simulations of interstellar turbulence and star formation include isothermal models of molecular clouds and larger-scale multi-phase models to simulate the formulation of molecular clouds. They *show how self-organization in highly compressible magnetized turbulence in the multi-phase interstellar medium can be exploited to generate realistic initial conditions for star formation* (Kritsuk et al. 2011). Multiple states of star-forming clouds have been identified in 3-D MHD simulations: gravity splits the clouds into two populations, one low-density turbulent state, and one high-density collapse state (Collins et al. 2012).

*Critical Assessment:* The evidence for self-organization in the star formation process is the morphological change from an initial randomized molecular cloud to concentrations in a number of small localized (H II) zones in galaxies, which represent spatially ordered structures (S), in contrast to the initially uniform randomness of the interstellar gas. A size distribution of ordered structures, however, has not been quantified yet. The corresponding ordered time structures (T) are produced by repetitive violent bursts of star formation. The physical process of self-organization in star formation is modeled in terms of highly compressible magnetized turbulence, which can trigger instabilities ending with high-density collapses (I) (Table 1: qualifiers I,S,T).

#### 4.2. Stellar and other Quasi-Periodic Oscillations

The origins of quasi-periodic oscillations (QPO) observed from various stellar sources (pulsars, cataclysmic variable stars, neutron stars, binary stars, active galactic nuclei, etc.) are largely not understood. Interpretations have focused on attributing the overall variability to accretion fluctuations, with the QPO produced by modulation of the accretion, for example by resonance-like interactions between natural rotational and orbital frequencies or – more germane to this article – nonlinear chaotic dynamics perhaps with modulated limit cycles, which point to self-organizing systems.

A number of attempts to detect and characterize deterministic chaos from astronomical time series data have been made. For example, the irregular X-ray variability of the neutron star Her X-1 has been analyzed with the method of Procaccia (1985) and detection of a low-dimensional attractor ( $D \approx 2.3$ ) and some higher-dimensional chaos was inferred for the accretion disk (Voges et al. 1987). The light curves of three long-period cataclysmic variable stars have been analyzed with the technique of Grassberger and Procaccia (1983a,b) in the search of an attractor dimension, but the light curves could be modeled with a periodic and a superimposed random component (Cannizzo et al. 1990). Evidence for a low-dimensional attractor with a dimension of  $D \approx 1.5$  was found in the Vela pulsar with a correlation sum technique (Harding et al. 1990).

However, much of this earlier work has proved to be questionable. For example the result found by Voges et al. (1987) was disputed by Norris and Matilsky (1989), who concluded that the insufficient signal-to-noise ratio does not allow to distinguish from an ordinary attractor contaminated with noise. Since the attractor dimension is equivalent to the number of coupled differential equations, we would expect a lowest attractor dimension of  $D = 2$  for the Lotka-Volterra equation system, or  $D = 3$  for the Lorenz model. Based on a careful simulation study of non-chaotic random data Harding et al. (1990) questioned the significance of their own result quoted above. They concluded “It appears that the correlation sum estimator for dimension is unable to distinguish between chaotic and random processes.”

This important cautionary remark is reinforced by at least two key theoretical results. Eckmann and Ruelle (1992) presented an elementary proof that the correlation dimension estimated with the Grassberger-Procaccia algorithm cannot exceed the value  $2 \log_{10}(N)$ , where  $N$  is the number of points in the time series. (One finds in the astronomical literature a number of dimension estimates approximating this value, suggesting that they are entirely spurious.) Osborne and Ruelle (1992) disproved several then traditional views in this context, showing that essentially any correlation dimension can be found for entirely random (i.e. lacking any “deterministic chaos”) colored random data simply by choosing the appropriate index for the power-law power spectrum of the data. They concluded “These results have implications on the experimental study of deterministic chaos as they indicate that the sole observation of a finite fractal dimension from the analysis of a time series is not sufficient to infer the presence of a strange attractor in the system dynamics.”

All in all, these theoretical limits and the realities of signal-to-noise and length of available time series cast a pall on the quest for evidence of nonlinear dynamics in astronomical systems that continues to some extent today.

However the landscape of time domain astronomy is improving with respect to time coverage, sampling cadence and signal-to-noise, and perhaps prospects for more definitive characterization of underlying dynamics of variable objects will improve accordingly.

Based on a more elaborate and physically motivated approach, a time series from the R Scuti star, a RV Tau type star, was found to exhibit deterministic chaos (with an embedding dimension of 4), because it was not multi-periodic and could not be generated by a linear stochastic process (Buchler et al. 1996). The quasi-periodic light curve is shown in Fig. 27 (top panel), along with a synthetic light curve generated with a corresponding low-dimensional (strange) attractor (Fig. 27 middle and bottom). However, Mannattil et al. (2016) offer a detailed criticism of this methodology, albeit in the different context of X-ray variability.

On the other side of the theory-observation coin, two simple physical metaphors incorporating self-organization ideas have inspired independent quasi-stochastic models reproducing some features of the observed variability of accretion sources. The dripping handrail (Scargle et al. 1993) evokes an analogy between astrophysical accretion on the one hand and the accumulation, flow, and dripping of moisture on a stairway’s handrail on the other hand. These authors quantified the quasi-periodic oscillations (QPO) of the low-mass X-ray binary star (LMXB) Scorpius X-1 with a wavelet based power spectrum that was found to be consistent with the spectrum computed for a dripping handrail accretion model, a simple dynamical system that exhibits transient chaos (Scargle 1993; Young and Scargle 1996). This highly oversimplified picture nevertheless explains the  $1/f$  and QPO features — typically though to be separate phenomena — as two aspects of a single physical process, notably ascribing the variability as quasi-random due to non-linear dynamics in a constant external accretion flow (and not due to a postulated random accretion).

The sandpile metaphor independently inspired a self organization model (Mineshige et al. 1994a,b; Mineshige and Negoro 1999), similar to the dripping handrail, physically somewhat more realistic in that its 2D geometry allowed treatment of angular momentum transport within the accretion disk. On the other hand these authors postulated randomness for accretion, although quasi-randomness is generated automatically by nonlinearities in their model even with steady accretion, for the same reasons as with the dripping handrail model.

The fluctuation power spectra of accreting black holes, neutron stars, and white dwarfs that are accreting gas from a stellar companion sometimes exhibit peaks at certain frequencies (Remillard and McClintock 2006; van der Klis 2006). These are also seen from some supermassive black holes powering active galactic nuclei (Smith et al. 2018). These peaks are called “*quasi-periodic oscillations*” (QPOs), since they are usually not very narrow. The frequencies observed in the neutron star and white dwarf sources are time-dependent, usually being positively correlated with the luminosity (proportional to the mass-accretion rate). The black hole sources exhibit two classes of QPOs, separated in frequency by a factor of at least 30. Only the *high-frequency quasi-periodic oscillations* (HFQPOs) have a fixed frequency, which is slightly below that of the innermost stable orbit in the accretion disk (and therefore inversely proportional to the mass of the black hole). However, these HFQPOs have a relatively small duty cycle. A mysterious property of many of them is the 3:2 ratio of the two highest frequencies (Wagoner 2008). There is no complete physical theory that can explain this fact, and no numerical simulations reproduce the observed QPOs. The accretion disks are very turbulent, driven by the conversion of the differential rotational energy via the magneto-rotational instability. In addition, they are subject to viscous and thermal instabilities, on time scales greater than the orbital period at that radius. The hotter “corona” of the neutron star and black hole disks appears to up scatter the cooler thermal photons from the disk into X-rays, without seriously demodulating them.

*Critical Assessment:* A number of oscillatory light curves from various types of stars have been recorded, which clearly establish the presence of non-random ordered time structures ( $T$ ). The spatial counterparts ( $S$ ), of course, cannot be resolved in stellar distances. The time evolution is generally quasi-periodic, which is typical for nonlinear dissipative systems with limit cycles ( $LC$ ), and low-dimensional attractors have been identified from those time series.

*The physical mechanism or instability (I) that is responsible for stellar quasi-periodic oscillations is less clear, but an accretion model (i.e., the dripping handrail model) has been proposed (Table 1: qualifiers T, LC, I[?]).*

### 4.3. Pulsar Superfluid Unpinning

In the crust of a neutron star or pulsar, the neutron superfluid coexists with a lattice of nuclei (Fig. 28). The rotation in a superfluid occurs along quantized vortex lines only, which must be able to move outward freely, in order that the superfluid can follow the observed, electromagnetically driven braking of the pulsar’s rotation. However, there are pinning centers in the neutron star crust that inhibit free vortex motion. Therefore the vortex lines could be pinned to the nuclei in certain layers of the crust (Anderson et al. 1981). An angular velocity lag builds up between the crust and superfluid as a consequence. When the lag exceeds a threshold, vortex lines unpin catastrophically and move outward, transferring angular momentum from the superfluid to the crust and producing an observable impulsive spin-up of the star, known as a “pulsar glitch”.

Pulsar glitches are generally interpreted in terms of the self-organized criticality model, due to the scale-invariant, power law-like distributions of sizes and exponential waiting time distributions (Melatos et al. 2008; Espinoza et al. 2011). In this scenario, superfluid vortices pin metastably in macroscopic domains and unpin collectively via nearest-neighbor avalanches. Recent quantum mechanical simulations, in which the evolution of the pinned, decelerating superfluid is described by the time-dependent Gross-Pitaevskii equation, have identified two knock-on processes responsible for mediating vortex avalanches: local, hydrodynamic, nearest-neighbor repulsion and nonlocal, acoustic-wave unpinning (Warszawski et al. 2012). The simulations also reproduce the size and waiting-time statistics in observational data, albeit over a relatively small dynamic range because computational limitations restrict the simulated system to  $< 200$  vortex lines at present (Warszawski and Melatos 2011; Melatos et al. 2015). Alternatively, Melatos and Warszawski (2009) propose a noncritical self-organization process (which they call “coherent noise” according to Sneppen and Newman 1997), where the global Magnus force acts uniformly on vortices trapped in a range of pinning potentials and undergoing thermal creep. In this scenario, Melatos and Warszawski (2009) find that vortices again unpin collectively, without nearest-neighbor avalanches, but still produce a scale-free size distribution as observed. The microscopic self-organization processes of nuclear matter in neutron star crusts has also been simulated in crystalline lattices, *where the system organizes itself into exotic structures* (Sebille et al. 2011; Caplan and Horowitz 2017). When the magnetic field in the superconducting stellar interior is included, the vortex lines and magnetic flux tubes self-organize into a turbulent, reconnecting tangle, sustained by stellar braking (Drummond and Melatos 2017). The flux tubes act as pinning centers as well, widening the scope for vortex line avalanches to occur.

In the pulsar glitch self-organization process, the driver is the electromagnetic braking of the star, while the feedback mechanism is the local interplay between the superfluid Magnus force and the pinning potentials, which regulate semi-coherent unpinning (Cheng et al. 1988). An alternative yet analogous scenario involving elastic stresses (star quakes) has also been proposed (Middleditch et al. 2006). A promising theoretical framework that is applicable to a wide variety of self-organizing systems of this kind is the mean-field model of a state-dependent Poisson process, introduced originally in the context of forest fires (Daly and Porporato 2006), and solar flares (Wheatland 2008), and generalized recently to neutron stars (Fulgenzi et al. 2017) and biological applications (Miles and Keener 2017). The model makes quantitative predictions of size and waiting time distributions and size-waiting time correlations as a function of the driving rate, independent of the detailed microphysics.

*Critical Assessment: One manifestation of self-organization is the lattice grid of nuclei in the neutron superfluid zone of a neutron star, which is a highly ordered spatial (S) structure (like a crystal), opposed to a random-like thermodynamic fluid in normal stars. The physical model involves the rapid rotation of a pulsar (driver), and a feedback*

*mechanism is given by the inhibition of vortex motion in the superfluid unpinning potentials (I). The feedback mechanism maintains a semi-coherent unpinning, which represents a spatial ordered structure (S) also. A caveat of this model is that observations of neutron star glitches exhibit scale-free power law distributions, which are typical for self-organized criticality models (Table 1: qualifiers S[?], I[?]).*

## 5. GALACTIC PHYSICS

Observable galaxies arise when gas (“baryons”) flows into concentrations (“halos”) of dark matter and forms stars, which themselves radiate and excite residual gas to radiate in a number of ways. The morphologies of the galaxies we now see is a time-slice of ongoing processes that include: (i) build-up of halos massive enough to retain gas within a framework of intersecting cell-walls and filaments; (ii) continuing gas inflow (only about half of the baryons are currently within star-forming halos); (iii) outflow of gas (and some recycling) driven by winds and jets from bursts of star formation, supernovae, and central supermassive black holes; (iv) gravitationally driven encounters between halos, described as major mergers (when the masses are comparable), producing spiral arms and disks), and minor mergers or captures of little galaxies by large ones (which can make star streams, rings, disks, and central bulges, and in the process initiate driving of spiral arms). The starting point is a random distribution of small ( $\approx 10^{-5}$ ) density fluctuations in the distribution of dark matter through the universe, with the spectrum of those fluctuations described by  $N(\delta\rho) \propto (\delta\rho)^{-1}$  (the Harrison-Zeldovich spectrum). A constraint throughout is that the mass of central black holes is close to  $\approx 0.8 \cdot 10^{-3}$  of the mass of stars through much of the cosmic history.

Over several decades now, many groups have modeled this scenario of a universe with N-body simulations (with N gradually increasing from  $10^6$  to  $10^{10}$  and more), and a brief summary of the results is “*Any correct description of our universe must look very much like  $\Lambda$ CDM on large scales, seeded by a nearly scale-invariant fluctuations spectrum that is dominated by dark energy*” (Bullock and Boylan-Kolchin 2017). That is, theory and observations agree well for length scales of a megaparsec and more. The situation on small scales is very much less satisfactory (Bullock and Boylan-Kolchin 2017; Naab and Ostriker 2017; Freeman 2017; Concelice 2014). One approach has been the “zoom simulation” (Springel et al. 2005) that switches from large scale considerations to something like the size of a galaxy and includes gas processes, star formation, and dust attenuation within either an adaptive mesh refinement or a smoothed particle hydrodynamic code. Naab and Ostriker (2017) show results (2011-2015) from six groups. Each resembles some real galaxy (e.g., see figures in Concelice 2014), but resemble all to the scenario called “floculent” (Elmegreen and Elmegreen 1987), rather than the “grand design” (Elmegreen 2011). In addition, it is a general principle that a theoretical process that mimics the real world, does not proof its correctness (an argument often used in discussions of biological evolution).

The next question is what physical model can produce spirals (at least numerically calculated), and which scenario can be described in terms of self-organization? Binney and Merrifield (1998) state that the arms nearly always trail; they are bright because the young stars have formed there, but there is some enhanced density of old stars as well ( $\approx 40\%$ ). Gas is needed to sustain the process, so galaxies of the Hubble type S0 generally do not show arms, and bars and companions can be drivers. However Binney and Merrifield (1998) consider spiral arms, although appearing as prominent features, not to be very important in the great scheme.

First, it is necessary to understand how some galaxies develop disks. Jeans (1915), starting with methods due to Boltzmann and treating stars as the gas particles, concluded that a non-spherical system with stellar motions describable as gas streams could not be static. Bertil Lindblad (1926, 1927, 1925) recognized that the Milky Way, or at least the parts of it he could study, is rotating, that spiral arms seen in the newly-recognized extragalactic nebulae would wind up fairly quickly, and that a pattern of higher density in the arms, rotating more slowly than matter, could be more stable. Lindblad describes his mathematical methods as deriving from work by Poincare, also applied to gases.

Sufficient angular momentum produces disks. Lindblad thought the rotation might arise from galaxy encounters or mergers, though we now associate mergers with destruction of disks and formation of ellipticals. Instabilities tend to form warps and bars (which the Milky Way has both) (Bland-Hawthorn and Gerhard 2016), and it is true that while 2/3 of S-type galaxies now have bars, they were rare at  $z = 1$ , but disks still survive. Ostriker and Peebles (1973) proposed in their highly-cited paper that an extended, dark, spheroidal halo would permit survival. Bland-Hawthornie

and Gerhard (2016) show NGC 3 spirals rectified to face-on might be confused with the Milky Way if we could see it face-on from outside. None has two dominant arms of the type of M51 galaxy, but none shows the complexity as the products of “Zoom-in simulations” (Springel et al. 2005). It is perhaps significant that the Milky Way also belongs to the rare “green valley” category of galaxies that are neither blue, vigorous star formers, nor red and dead.

Comments specific to the Milky Way include that it reached its mostly 2-armed state about 9 Gyrs ago (Francis and Anderson 2009), that its present conditions was probably triggered by a first encounter with the Sagittarius dwarf spheroidal galaxy (Purcell and Bullock 2011). M31 incidentally also has a “driving companion” and both galaxies have their dwarf spheroidal companions largely organized in a planar thin structure that is also not understood.

According to Freeman (2017) true bulges come from mergers, while instabilities in disks provide bars and pseudo bulges as in the Milky Way. Our thick disk (which does not have arms, nor do other thick disks (they are nearly but not quite ubiquitous) formed 11-12 Gyrs ago, at  $z = 2 - 2.5$  equivalent time, which is very close to the peak of the star formation rate for the local universe as a whole (Madau and Dickinson 2014) and probably also for the Milky Way (though we expect to know more about this topic when the Gaia data are fully in and analyzed), but it is likely that the Milky Way spiral pattern requires more than one mechanism. The oldest spiral reported so far (in a sea of dwarf irregular structures imaged by HST in its deep field) is labeled as Q2343-BX442 (Law et al. 2015) and is of the “companion driven” variety, being seen at a redshift that corresponds to an age near 11 Gyrs, and evolution tends to move galaxies from *flocculent* to *grand design* (Francis and Anderson 2009).

There are also many galaxy-evolution issues that do not obviously interact with spiral structure, for instance the correlation of stellar masses with central *Super Massive Black Hole* masses (Heckman and Best 2014) and deciding whether they radiate enough ultraviolet to re-ionize the universe at  $z \approx 6$  (Stark 2016). Locally first, if not temporally first, come perturbations exerted on disks by a companion galaxy or bar. The former, with a swing amplifier, undoubtedly makes things to start as tidal distortions and end up looking like grand design spirals (Toomre 1981). And an ensemble of molecular clouds in the potential of a barred galaxy comes to trace out a spiral type S with their star formation (energy dissipation) (Combes and Gerin 1985). But see Toomre (1977) for how far the purely gravitational processes had come 40 years ago. Woltjer (1965), on the other hand, was certain (and has been since at least Woltjer 1959) that magnetic fields had to be part of the answer, since the energy densities in the Galactic plane in field, cosmic rays, and random gas motions are roughly equal, and both field lines and gas motions seemed to be at least partially along the arms.

This brings us to the density wave theory of Lin and Shu (1964) and Shu (2016). They decided to tackle the problem for the middle, that is, to impose pitched arms on the disk density structure and gravitational potential and see what happened. The short answer was “Not much”; That is the pattern persisted, soliton-like, for several times the rotation period of the model galaxy, and the pitch-angles of real galaxies look like the calculated ones (Pour-Imani and Kenefick et al. 2016). The modern version naturally looks a good deal more complex than the 1964 original, but also has some applicability to the rings of Saturn and hot-Jupiter formation around other stars (Shu 2016).

The chief competing theory for some years, applicable particularly to spiral in the past and to flocculent ones in *Stochastic Self-Propagating Star Formation (SSPSF)*, but forward by Mueller and Arnett (1976) and further developed by Gerola and Seiden (1978). The idea is that a random fluctuation in gas density yields a small burst or star formation; winds from the stars and supernovae move outward, compressing gas, which, in turn, forms stars. Differential rotation in the disk, which will eventually wind up and spoil arms, in the short term ( $\approx 10^8$  years), so the galactic rotation period stretches out those regions of propagating star formation into arc-shaped features. Thus SSPSF is a possible “starter” to establish S-shaped perturbations to the the Lin and Shu (1964) process started. Auer (1999) combined the processes in roughly this fashion and regarded the result as a good way of looking at the initiation, development, and eventual washing out of spiral structure. Since all processes (Naab and Ostriker gas outflows, Lin and Shu magnetic

confinement, SSPSF, and event companion driving) require the presence of gas to form new stars and make the arms visible spiral arms necessarily transient, on time scale from  $10^8$  to  $10^{10}$  years.

In summary, the structure of our Milky Way was triggered when the Sagittarius dwarf first passed through the disk about 9 Gyrs ago (Purcell et al. 2011). The arms have been preserved by a density wave (Lin and Shu 1964) with a swing amplifier (Toomre 1981, 1977), but an image reconstructed from HI data and starcluster information suggests with the bar as a likely additional driver (Combes and Gerin 1985), but an image reconstructed from HI and starclusters data (Bland-Hawthorn and Gerhard 2016; Elmegreen 2011) that we also have transient, flocculent spurs and other structures (Elmegreen and Elmegreen 1987). Gas inflow, which continues along the filaments that connect galaxies (Faucher-Giguere and Angles-Alcazar 2017), tends to make the disk larger and less dense and capable of continuing star formation (Nabb and Ostriker 2017).

We turn now to the four cases of spiral formation or preservation that appear to be most closely connected with self-organization.

The spiral pattern of differentially rotating galactic disks represents a self-organization process (Fig. 29). Nozakura and Ikeuchi (1988) model irregular and regular spiral patterns of the interstellar medium with a reaction-diffusion process (Fig. 30), which is a self-organization process known in chemistry (e.g., Bray, W.C. 1921; Cox et al. 1985).

The physical model of a differentially rotating galactic disk of Nozakura and Ikeuchi (1988) contains the following assumptions: (i) The interstellar medium has two components  $\rho_1(\mathbf{r}, t)$  and  $\rho_2(\mathbf{r}, t)$ ; (ii) The interstellar medium exhibits a limit-cycle behavior around a steady point  $(\rho_{10}, \rho_{20})$  in the  $\rho_1 - \rho_2$  phase space; (iii) the galactic disk is 2-dimensional and infinitely extended; (iv) the rotation curve of the galactic disk is flat,  $V(\mathbf{r}) = const = V_0$  throughout the disk ( $0 \leq r < \infty$ ); and (v) the propagation of the local interstellar medium is expressed by the scalar diffusion matrix  $\mathbf{D} = diag(D, D)$ , where  $D > 0$  is a diffusion coefficient. The model with the following reaction-diffusion equations with advective terms satisfies these 5 conditions:

$$\frac{\partial}{\partial t} \begin{pmatrix} \rho'_1 \\ \rho'_2 \end{pmatrix} + \frac{V_0}{r} \frac{\partial}{\partial \theta} \begin{pmatrix} \rho'_1 \\ \rho'_2 \end{pmatrix} = \begin{bmatrix} \lambda(\rho') & -\omega(\rho') \\ \omega(\rho') & -\lambda(\rho') \end{bmatrix} \begin{pmatrix} \rho'_1 \\ \rho'_2 \end{pmatrix} + \mathbf{D} \nabla_r^2 \begin{pmatrix} \rho'_1 \\ \rho'_2 \end{pmatrix}, \quad (33)$$

where  $\rho'_i(\mathbf{r}, t) = \rho_i(\mathbf{r}, t) - \rho_{i0}$ ,  $i = 1, 2$  are the deviations of  $\rho_1$  and  $\rho_2$  from their steady values  $\rho_{10}$  and  $\rho_{20}$ .  $\lambda(\rho')$  and  $\omega(\rho')$  are the nonlinear reaction terms concerning mainly with the stability and the oscillation frequency of the system, and  $\mathbf{D}$  is the diffusion matrix. Nozakura and Ikeuchi (1988) found nonlinear rigidly-rotating spiral wave solutions for this analytical model, which is designed to have limit-cycle solutions. In this model, rigidly-rotating spiral structures are a consequence of the balance between the winding effect of differential rotation and the straightening effect of diffusive propagation.

More complex galactic models with chaotic orbits and massive central masses (possibly attributed to a central black hole) were investigated by Kalapotharakos et al. (2004). Small central masses with a ratio of  $m < 0.005$  were found to organize chaotic orbits with Lyapunov exponents too small to develop chaotic diffusion during a Hubble time. Large central masses ( $m \gtrsim 0.004$ ), produce about the same amount of chaotic orbits, but the Lyapunov exponents are larger, so that the secular evolution evolves into a new equilibrium. The underlying self-organization mechanism converts chaotic orbits into ordered orbits of the *Short Axis Tube* type (Kalapotharakos et al. 2004).

A spatio-temporal self-organization in galaxy formation has been found from a relationship between the number of star formation peaks (per unit time) and the size of the temporal smoothing window function (used to define the peaks), holding over a range of  $\Delta t = 10 - 1000$  Myr (Cen 2014). *This finding reveals that the superficially chaotic process of galaxy formation is underlined by temporal self-organization up to at least one Gyr* (Cen 2014).

The observed hierarchy of galactic structures, from giant cellular voids to enormous superclusters, with galaxies distributed within intricate networks of arcs and cells, clearly indicates some self-organizing process that is not con-

sistent with a random distribution (Krishan 1991, 1992). Two different scenarios are usually considered: (i) the hot dark matter (HDM) scenario with initial large-scale structures that fragment into smaller ones, and (ii) the cold dark matter (CDM) scenario where the smaller structures form first, coalescing then to larger galactic structures. However, besides the self-organization of structures seen in luminous matter, the existence of dark matter (Trimble 1987) may have its own “dark self-organization”. Related self-organization processes may drive gravitational clustering and/or turbulent cascading (Krishan 1991, 1992).

*Critical Assessment: According to the Hubble galaxy classification, galaxies can be formed in different morphologies, from ellipticals (type E0-E7) to normal spirals (type Sa-Sc) and barred spirals (SBa-SBc), which all represent a spatial pattern (S) observed in our present time-slice. The evolution from an initial random-like state to a well-ordered spatial structure (S) with a spiral pattern reveals the action of a self-organization process. Physical models of galaxy formation include at least three scenarios that are more or less consistent with the  $\Lambda$ CDM cosmology: (i) Interaction with a nearby companion, (ii) the Lin-Shu density wave theory, or (iii) flocculent bursts of star formation that get dragged out by differential rotation. Thus, a combination of gravity and rotation is a most likely driving force, while the feedback force or self-organizing instability is still open and is currently investigated with large-scale numerical N-body simulations. (Table 1: qualifiers S, I[?]).*

## 6. COSMOLOGY

Self-organization inherently involves regulated change. That is, it must be dynamical, involving driver forces and positive feedback mechanisms. Each of these features has an associated scale. When looking for the self-organizational aspects of cosmology, relevant scale sizes run from (at least) as small as the Planck scale ( $\approx 10^{-33}$  cm) to the size of the observable Universe ( $\approx 10^{28}$  cm), spanning over 60 orders of magnitude. Perhaps even more challenging, modern science has yet to reveal exactly whether and how one may correctly separate our understanding of particles and fields from that of the space-time in which they exist, especially at scales near to and less than the Planck scale. For the purposes of this review, we will simply focus on the organizational aspects of mainstream cosmology.

### 6.1. Einstein-de Sitter and $\Lambda$ CDM Models

The first goal of cosmology is to understand how space changes with time. Einstein “interpreted gravity as a manifestation of geometry” (Misner et al. 1973). He showed us that a “4-D space-time” formed by merging 3-D space and the time dimension into one continuum (space-time), can respond to any form of energy. Einstein’s equation couples the curvature of space-time, i.e. gravity, to the stress-energy inside it. Therefore, placing energy sources inside a well-chosen unified 4-D space-time geometry is the best way to quantify how they coevolve. To examine how order developed, we recognize that the expansion dynamics of space-time sensitively depends upon the amount(s) of each energy component inside it, and the evolving organization of those energy components depends upon the expansion dynamics. Such coupling or “feedback” can lead to an evolution that “self-organizes”. Thus, when space-time contains matter and/or vacuum energy, interesting processes can emerge.

Einstein’s first solution to his equation assumed that space-time contained uniformly distributed normal matter, but was static; however, quickly realizing that space-time containing only matter would collapse, unless another component was included to resist it, he added a positive “cosmological constant term”. This is the equivalent of a uniform vacuum energy that counter-balances the curvature-producing effect of matter. Soon thereafter de Sitter produced a model envisioning a maximally symmetric space whose “metric” (curvature) is the same *at all times and all places*, which also included both uniformly distributed matter and a cosmological term to balance it. For such a space-time (de Sitter model 1), one may choose a time coordinate and its associated family of space like coordinates (“slicings”) that correspond to specific values of that time coordinate, to thereby represent geometrically flat (Euclidean), positively-curved, or negatively-curved 3-D spaces. However, the de Sitter (model 1) space does not restrict this choice, so it does not select a specific cosmology, *per se*. In other words, maximally symmetric de Sitter (model 1) space may just rest! However, *maximally symmetric space-times are ... not reasonable models of the real world* (Carroll 2004). Then, de Sitter found that in a space-time with only a cosmological constant and no matter, test particles would accelerate away from one another! It is this second version (de Sitter model 2) with accelerating expansion that is normally associated with the “de Sitter space”. This was progress.

In the 1920s, Alexander Friedman and Georges LeMaitre further studied how the inclusion of matter in Einstein’s Equation could affect things, but this time their independently derived solutions narrowed down the space-time symmetries to yield a cosmological model of a universe that can undergo smooth expansion (Fig. 31). More importantly, if one assumes that space-time contains a homogeneous and isotropic cosmic fluid composed of given matter, radiation and/or vacuum energy densities, the Friedman-LeMaitre solutions will: (i) limit its geometrical possibilities by selecting slicings from among the flat, positively, and negative curvature options for the 3-D spatial part of the metric, and (ii) determine its expansion dynamics! Matter and radiation resist or slow down the expansion rate, while vacuum energy does the opposite. In addition, initial densities of radiation and matter decrease with volume, while vacuum energy normally stays constant, all the while remaining isotropic and homogeneous. Their model is reflected in the

following two equations known as the “Friedman Equations”:

$$\left(\frac{\dot{a}}{a}\right)^2 = \frac{8\pi G}{3}\rho - \frac{k}{a^2}, \quad (34)$$

$$\left(\frac{\ddot{a}}{a}\right) = -\frac{4\pi G}{3}(\rho + 3p), \quad (35)$$

where changes in the scale factor  $a$  are related to total energy density  $\rho$  (which can include matter, radiation, and vacuum), the overall geometrical curvature  $k$  (can be positive, negative, or zero), and pressure  $p$ . Note that the term in parentheses in Eq. 34 is the “Hubble parameter”. These equations were derived by inserting the “Robertson-Walker metric” into Einstein’s Equation, which then expresses how the scale factor (size) of 3-D space changes with time. This combination successfully related the scale factor to the evolving stress-energy of the Universe.

It was eventually recognized that our actual Universe (i) is geometrically flat ( $k = 0$ ), (ii) has been expanding for almost 14 billion years, (iii) its cosmic fluid has passed through stages where its dominant component was radiation, then matter, and then vacuum energy, and (iv) we have been in a quasi-de Sitter accelerating expansion stage for the last 6 billion years! (Fig. 31). There is compelling evidence that the cosmic fluid is made up of normal matter and radiation, a form of matter that does not emit or absorb electromagnetic radiation (*Cold Dark Matter* or “*CDM*”), and vacuum energy (“*Dark Energy*”). It is then no surprise that the current cosmological model (“ $\Lambda$ CDM”) is based upon the Friedman Equations, although it is still undecided whether the vacuum energy component has a constant value ( $\Lambda$ ) or is changing with time (Fig. 31).

## 6.2. Evolution of Matterless Space-Time

The self-organizational concepts have been applied to the creation of de Sitter (model 2) space-time (only vacuum energy) and to the more relevant Friedman-LeMaitre space-time that obeys the Friedman equation. Creation of de Sitter (model 2) space-time from quantum fluctuations, combining causality and gravity with quantum theory, was discussed by Ambjorn et al. 2008. Viewed as a self-organization process, many microscopic constituents exhibit a collective behavior and give rise to a unified, smooth space-time macrostructure in this model. However, one must keep in mind that this pure de Sitter (model 2) space-time, without matter, is maximally symmetric and too broad to reflect the real Universe.

In another approach quantum gravity is described as a network that self-organizes into a discrete 4-D universe, in analogy to the ferro-magnetic Ising model for space-time vertices with an anti-ferromagnetic Ising model for the links. The ground state self-organizes as a new type of low-clustering graph with finite Hausdorff dimension 4 (Trugenberger 2015). Once again, this work does not appear to directly lead to the  $\Lambda$ CDM model.

## 6.3. Evolution of Space-Time with Matter and Radiation

The largest order out of random process in astrophysics today is the production of the observed large scale structure of galaxies and clusters of galaxies throughout the cosmos. The  $\Lambda$ CDM model, together with the theory of cosmic inflation, lay the foundation (i) for generating the initial conditions for structure formation, (ii) for creating matter and radiation, and (iii) for the subsequent hierarchical growth of the structure of matter via gravitational instability.

Because Einstein’s Equation relates space-time curvature (i.e., gravity) to the stress-energy of its contents, fluctuations of energy density will generate fluctuations of curvature. “Inflation theory” envisions a very early burst of

quasi-de Sitter (model 2) expansion during near-Planck scale stochastic quantum fluctuations of the inflation-driving scalar energy field (“inflaton”), and generates the corresponding space-time curvature fluctuations that expand superluminally to semi-classical scales. As inflation ends, the inflaton transfers its remaining energy into radiation and particles that, during the first few minutes of the Big Bang, evolve through a nucleosynthesis stage into a plasma of “normal matter” (comprised primarily of hydrogen and helium atoms and electrons) and gravitationally-interacting-only Dark Matter. As the continuing expansion further cools the cosmic fluid (plasma) further, the theory goes, it is attracted by the curvature fluctuations (gravitational potentials) originating from the inflaton field, and ultimately collapse into the structure we see today.

In a very recent paper, Ge and Wang (2017) set forth an approach to derive cosmological dynamics starting with the physics of quantum entanglement. Building upon earlier ideas that space-time geometry could be the result of the entanglement of macroscopic quantum states, together with recent work by Jakobson hypothesizing a relationship between Einstein’s equation for gravity and vacuum entanglement of quantum states, Ge and Wang (2017) were able to derive the flat-Universe Friedman equations (34) and (35) above. It will be interesting to see if further work exploiting the apparent deep connection between quantum information theory and the emergence of space-time will successfully be applied to the entire  $\Lambda$ CDM Universe paradigm with its inflaton field, dark matter, and dark energy.

#### 6.4. The Cosmic Microwave Background

Measurements of the *Cosmic Microwave Background (CMB)* over the past 25 years strongly support the idea that at about 400,000 years into the Big Bang the temperature of the H/He plasma dropped to around 3000 degrees K, allowing the electrically charged free electrons and nuclei to then combine into neutral atoms. At this point, known as “recombination”, electromagnetic radiation (photons) that had previously enabled the plasma to resist, gravitational collapse was released, carrying the image of the last surface from which it scattered. Continued expansion of the Universe then caused the wavelengths of the released photons to stretch from visible to microwave values.

The revolutionary and Nobel Prize winning (Smoot and Mather) *Cosmic Background Explorer (COBE)* satellite work (Mather et al. 1991; Boggess et al. 1992), followed by the *Wilkinson Microwave Anisotropy Probe (WMAP)* (Bennett et al. 2013; Hinshaw et al. 2013), and Planck satellites (Planck Collaboration 2016), with increasing sensitivity and resolution, precisely mapped that 13.8-billion-year-old microwave image of the celestial sphere of the cosmos which encoded much of the physics of the early Universe (Fig. 32).

The CMB revealed that the H/He plasma had begun to form slight over densities and under densities (anisotropies), i.e., clouds, of a range of sizes that reflected a Gaussian random distribution, just as predicted by inflation theory. The CMB analysis also revealed the relative amounts of normal matter, dark matter, and vacuum energy contained in the “cosmic fluid” at that time, and therefore the geometry and age of the currently observable Universe. This information combined with the distance-marking capability, demonstrated for Type Ia supernovae in Nobel Prize winning work (Riess et al. 1998; Perlmutter 1999), together with other measures of the expansion history of the Universe, provided the initial and continuing conditions that determined large scale structure. Fig. (33) depicts the overall evolution.

Interestingly, when the inflaton field transfers its energy into radiation and particles and the Universe then re-heats to thermal equilibrium to continue the hot Big Bang, the cosmic fluid may be treated as a perfect fluid undergoing an adiabatic expansion. As the temperature drops with expansion and matter is created, the big picture is still isotropic and homogeneous. At the time of the CMB release, the curvature fluctuations had caused anisotropies in the matter distribution on the order of one part in 100,000. Long before resolution of the CMB image, astronomers knew from observation that anisotropies at least this large were needed to “make structure on time”. Thereafter these wispy but critically important over-densities of matter underwent rapid local amplification via linear fluctuations, and then

collapsed by non-linear gravitational forces into structures. So here, the inflaton field served to generate both the driving force of the process as well as the primordial quantum fluctuations that seeded the gravitational feedback needed for structure formation from the thermally equilibrated and cooling cosmic fluid. Recent galaxy surveys clearly show a distribution pattern (Fig. 34).

### 6.5. Formation of Large Scale Structure

N-body simulations of the post-CMB evolution of dark matter into large scale structure were carried out by the Virgo Consortium (Millenium Simulation or MS) in 2005 (Springel et al. 2005). The basic simulation, including only dark matter, successfully reproduced the “cosmic web” topology (Libeskind et al. 2017) of a  $\Lambda$ CDM Universe, with its known clusters and filaments of size  $\approx 100$  Mpc and its essentially isotropic homogenous matter distribution on larger scales (Fig. 35 bottom to top). The formation of galaxies and quasars was then separately accounted for by adding semi-analytic modeling to test the importance of “baryonic effects”, such as gas cooling, star formation, feedback, etc., within the simulated dark matter substructures. Then, the group examined galaxy clustering, luminosities and colors (star formation rate and age) and compared these with observations.

More recently, the Illustris Simulation (IS) carried out a series of large-scale simulations of galaxy formation that included both gravity and hydrodynamics to directly account for the baryonic component (gas, stars, supermassive black holes, etc.). The  $\Lambda$ CDM model and recent CMB derived cosmological parameters were again used to set the initial conditions of the simulation, which began 12 million years after the Big Bang and ran forward for about 14 billion years. As seen in Fig. (36 from bottom to top), the IS depicts the evolution of dark and baryonic matter from the linear through the non-linear collapse stages, and beautifully reproduces the growth of structure that favorably compares with observations. Using short time steps, the IS was also able to show the time evolution of baryon parameters (gas temperature, density and metallicity) associated with simulated Active Galactic Nuclei explosions (Fig. 37 from left to right).

So how do the MS and IS relate to the theme of this review? They show that the  $\Lambda$ CDM model, including inflation, well describes the physical evolution of the large-scale structure of the Universe to the present time. The most interesting feature of the underlying cosmological model is that a period of exponential inflation can temporarily remove all disorder within the causal speck of space-time that then grows into our current observable Universe. At the end of inflation, the matter content of the cosmic fluid is created from the remaining inflaton energy and re-heats to a temperature at or above that envisioned by grand unified particle theories. Then, the “Big Bang” ensues. This model ensures that the post-inflation evolution of the Universe is basically isotropic and homogenous, as the Friedman Equation assumes. However, it is most fortunate for us that the large-scale structure is not perfectly isotropic and homogeneous, but exhibits a definite ordering into filaments, cluster nodes and voids on scales smaller than  $\approx 100$  Mpc where galaxies and stars, heavier elements, and life came to be.

### 6.6. Self-Organization and Logistic Growth

The topology of the large-scale structures of our Universe can be characterized by fractal geometry (Murdzek and Iftimie 2008). Using the recently completed redshift surveys (e.g., Fig. 34), which provide galactic right ascension ( $l$ ), declination ( $b$ ), and redshift ( $z$ ), one can transform the redshift  $z$  into a distance  $r$ ,

$$r = \frac{c}{H} \int_0^z \frac{dz}{\sqrt{\Omega_M(1+z)^3}}, \quad (36)$$

where  $c$  is the speed of light,  $H$  is the Hubble constant,  $H = 70 \text{ km s}^{-1} \text{ Mpc}^{-1}$ , and  $\Omega_M = 1$  is the the Einstein-de Sitter model, which then yields the 3-D space coordinates  $(l, b, r)$ , from which the fractal (Hausdorff) dimension  $D$  can be obtained, which defines a fractal volume  $V_{fractal} \propto r^D$  that is smaller than the Euclidean volume  $V \leq r^3$ , since  $D \leq 3$ . Murdzek and Ifimie (2008) find this way a lowest fractal dimension of  $D \approx 1.3$  for nearby galaxies ( $r = 25 \text{ Mpc}$ ), which monotonously grows and saturates at a value of  $D \lesssim 2.0$  at the largest distances ( $r \gtrsim 250 \text{ Mpc}$ ). They interpret the distance-dependent fractal dimension function  $D(r)$  as a radial (or temporal) evolution that can be modeled with a logistic curve (or Verhulst equation),

$$\frac{dD(r)}{dr} = \Gamma D(r) \left( 1 - \frac{D(r)}{D_\infty} \right), \quad (37)$$

where  $\Gamma$  is the exponential growth rate, and  $D_\infty = D(r = r_\infty)$  is the asymptotic limit at an infinite distance, also known as *carrying capacity* (or maximum amount of resources) in ecological models. The authors argue that the logistic growth model (Verhulst law), which describes nonlinear growth phenomena in a closed system with a limited total resource quantity ( $D_\infty$ ), is a concept that agrees with the nonlinear theory of structure formation, and thus indicates a self-organized universe. The self-organizational aspect is the predicted feedback that the growth rate  $dD(r)/dr$  of the fractal dimension  $D$  is decreasing to zero (in the asymptotic limit) when the scale is increased  $r \mapsto \infty$  (in Eq. 37). Interestingly, this model predicts an almost finite universe, where the mass or energy asymptotically vanishes at large distances ( $r \gtrsim 250 \text{ Mpc}$ ). It also predicts 2-D galactic structures at large distances, and 1-D structures (filaments or curvi-linear threads) at nearby galactic distances of  $r \lesssim 25 \text{ Mpc}$ .

## 6.7. Self-Organization of Interacting Cosmic Fluid Components

Self-organization of components of the cosmic fluid into stars and galaxies was covered earlier in this review where dark and baryonic matter are assumed to only interact gravitationally. However, non-gravitational interactions of dark matter and dark energy have also been studied in a cosmological model with diffusion (Szydlowski and Stachowski 2016). The state variables of the density parameter for matter (dark and visible) and of the rate of growth of energy transfer between the dark sectors can be coupled using the Lotka-Volterra framework, from which it was demonstrated that the de Sitter solution is a global attractor for all trajectories in the phase space (Szydlowski and Stachowski 2016). In a related approach, called the “Jungle Universe”, the dynamics of homogeneous and isotropic Friedman-Lemaitre universes are considered as a special case of a generalized Lotka-Volterra system, where the competitive species are the barotropic fluids that fill the universe (Perez et al. 2014).

*Critical Assessment: The large-scale structure of the Universe is seen to have resulted from a combination of quantum-fluctuation-seeded gravitational collapse and more complex particle physics, all the way back to the Big Bang. Self-organization concepts applied to cosmology are extremely scanty in literature (amounting to a few sentences in a few cosmology papers) and appear not to relate to the  $\Lambda$ CDM model. Quantitative measurements of spatial (S) or temporal structures (T) that discriminate against random patterns, identification of nonlinear dissipative systems with driver and positive feedback mechanisms, critical instabilities (I), and possible limit-cycle (LC) equilibria need to be identified. In conclusion, there is a lot of room for modeling of cosmological models in terms of self-organization (Table 1: qualifiers S[?], T[?], [I?], LC[?]).*

## 7. DISCUSSION

In this interdisciplinary review we aim to point out some universal properties of nonlinear systems governed by self-organization. We discussed 6 cases in planetary physics, 6 cases in solar physics, 3 cases in stellar physics, one case in galactic physics, and some tentative ideas in cosmology, amounting to 17 systems in the field of astronomy and astrophysics (Table 1). Self-organizing systems, however, have been found in many more scientific disciplines, such as in ionospheric physics, magnetospheric physics, plasma physics, physics, chemistry, biology, social science, and computer science, as the 51 examples compiled in Table 2 demonstrate.

In Table 4 we juxtapose the system characteristics of self-organizing systems to random systems, as well as to self-organized criticality systems. The three different dynamic system types are visualized also for the same medium, such as sand, in Fig. (38). In the following we characterize each system in turn.

### 7.1. Characteristics of Random Processes

Random or stochastic processes can be characterized with the statistics of independent events. The mathematical distribution of independent events can be derived from rolling dices, which leads to a binomial distribution and can be approximated by a Gaussian function (also called normal distribution) in the limit of an infinite number of dices, or with a Poisson distribution or exponential distribution in the limit of rare events. A time series of random events consists of irregular, intermittent events and the resulting power spectrum is characterized by white noise (i.e., a flat power spectrum  $f(\nu) = const$ ). We can consider random processes in time or in space. If spatial structures are produced by a random process, their size distribution is theoretically a Gaussian function, with a well-defined mean and standard deviation, where the mean defines a specific preferred spatial scale. From the thermodynamic or information (theory) point of view, the entropy is increasing with time in random processes. Examples of random processes are Brownian motion of gas molecules, diffusion processes, the detected photons from a star, electrical current fluctuations due to thermal noise, or patterns of sand at the beach (Fig. 38a). (For a concise summary of the statistics of random processes see Section 4 in Aschwanden 2011).

### 7.2. Characteristics of Self-Organized Criticality

Self-organized criticality systems (Bak et al. 1987; Pruessner 2012; Aschwanden et al. 2016) are completely different from random processes, which is experimentally and observationally demonstrated by the appearance of scale-free power law distributions of spatial and temporal sizes. Avalanches in self-organized criticality systems represent coherent structures in the time domain ( $1/f$ -noise), in contrast to incoherent noise in random systems. Quantitatively, a size distribution of avalanches in a self-organized criticality system can be simulated from chain reactions of nearest-neighbor interactions in a lattice grid, where a critical threshold of the gradient (or curvature radius) between next-neighbor interactions has to be exceeded, before an avalanche can start. The avalanches occur intermittently in such a complex system, and the intervening time intervals (waiting times) obey an exponential random distribution function. The spatial structure of the avalanches is fractal (or multi-fractal), which corresponds to a power law distribution also. The reason why such a dissipative nonlinear system is called “self-organizing”, (e.g., the critical slope of a sandpile) is the fact that the system automatically maintains the critical state of avalanching without external control, as long as the energy input into this open system is steady and stochastic. The microscopic structure of a self-organizing system is maintained in the time average, and thus the entropy of the system is invariant when averaged over many avalanches. Examples of self-organizing systems are sand piles (Fig. 38c), earthquakes, solar flares, forest fires, stock

market fluctuations, etc. (see a representative list of phenomena in Section 1 of Aschwanden 2011).

### 7.3. Characteristics of Self-Organization

Although the two terms “self-organization” and “self-organized criticality” sound confusingly similar, they characterize two completely different types of dissipative nonlinear systems, to which terminology we will adhere for historical reasons. The only commonality between the two systems is that both are open nonlinear dissipative systems with external energy input, and that both maintain some system property in an automated way without external control. A self-organizing system has always a primary driving force, and a secondary counter-acting force that acts as a stabilizing positive feedback reaction to the driving force. A system can only be called to be a self-organization process, when the feedback mechanism leads to a quasi-stationary stabilization of the combined system. Otherwise, a system with a negative feedback (or none) will evolve away from a stationary state and end in a catastrophic way.

What sets a self-organizing system apart from a random system is the ability to create “*order out of chaos*”, or better “*order out of randomness*”, since the term “chaos” is already used in nonlinear physics to characterize a particular type of nonlinear system behavior that is non-deterministic. Therefore, the property of self-organization is also called spontaneous order, a process where some form of overall order arises from local interactions between parts of an initially disordered system. In principle, every ordered structure that is significantly different from randomized distributions requires an ordering mechanism, or a self-organizing process. We have seen in this review that every self-organizing mechanism observed in astrophysics can be modeled by a system of coupled differential equations, among which the type of a Lotka-Volterra system is most prominent. These differential equations describe the interaction between a driving force and a positive feedback force, which generally have a limit-cycle solution, and therefore can sustain a quasi-stationary oscillation near the limit cycle, which is also called attractor (or strange attractor if it has a fractal structure). The quasi-stationary, quasi-periodic system dynamics near a limit cycle is the essential characteristic of self-organization processes.

What are the size distributions of a self-organizing system? Since the limit cycle represents a fixed value of a time period (which often corresponds also to a fixed value of a spatial structure), the size distribution is expected to be peaked or quantized at this particular value. For instance, the solar granulation exhibits a fixed spatial scale of  $w \approx 1500$  km for convection cells (granules), and a temporal scale (or life time) of  $\tau \approx 8 - 10$  min. In the case of planetary systems, each planet has its own attractor and limit-cycle dynamics, which are moreover weakly coupled by harmonic ratios in a N-body system. Since the limit-cycle solution often contains some random noise, the size distribution is generally not sharply quantized like a delta-function, but rather broadened to a single or multiple Gaussian functions, see Gaussian distribution of granules in Fig. (12, right panel).

Since self-organizing systems create “*order out of randomness*”, the entropy is decreasing during the evolution from an initially disordered system to a self-organized limit-cycle behavior. It is also said that self-organizing systems evolve into a dynamics far away from thermal equilibrium. A limit cycle is defined by a critical point (in phase space) around which the quasi-stationary oscillation dynamics occurs, where the amplitude of the oscillation is a measure how far off the system evolves from a system equilibrium solution. The thermal equilibrium therefore corresponds to the asymptotic limit of a vanishing limit-cycle amplitude, where every dynamic system variable becomes constant.

In Fig. 38b) we show the pattern of sand dunes, which self-organized in an interplay between gravity and wind, forming ripple patterns with a fixed ripple separation scale, which is distinctly different from sand piles generated by self-organized criticality avalanching (Fig. 38c), or from a sand beach shaped by random processes.

#### 7.4. The Physics of Self-Organization Systems

It should be clear by now that the term “self-organization” merely expresses a category of a nonlinear dissipative system behavior, which is a general property of complex system behavior, but does not define a specific physical model for an observed phenomenon. The choice of a particular physical model that is applied to an observed phenomenon is a matter of interpretation. We can study the dynamic system behavior with purely mathematical models (of coupled differential equation systems) without specifying a physical application (e.g., see examples in textbook by Strogatz 1994, Chapter 7). However, since we are most interested in obtaining physical insights from the observed phenomena, we identified the underlying driving forces and positive feedback mechanisms for each of the 17 studied astrophysical phenomena (Table 1).

A summary of observed astrophysical phenomena and the self-organizing driver forces and feedback mechanisms is given in Table 1, based on the concepts offered in the reviewed publications. Drivers can be the gravitational force, the centrifugal force (from rotation), differential rotation, solar radiation, temperature gradients, convection, magnetic stressing, plasma evaporation, acceleration of nonthermal particles, or the cosmic expansion. Feedback mechanisms involve mostly instabilities (i.e., the magneto-rotational or Balbus-Hawley instability, the Rayleigh-Bénard instability, turbulence, vortex attraction, magnetic reconnection, plasma condensation, loss-cone instability), but also resonances (mechanical orbit resonance, double plasma resonance). While instabilities mostly evolve into limit-cycle behavior, which constrains one specific time scale, resonances can produce ordered structures at multiple quantized values (such as harmonic orbit resonances of planets, or magnetic harmonics in upper hybrid waves of solar radio bursts).

We described the underlying physical models with systems of coupled differential equations in this review. Very few equation systems can be analytically solved, if at all. For instance, even the basic Lotka-Volterra equation system has a transcendental (implicit) solution (Appendix D). Consequently, the more complex cases that involve a hydrodynamic approach (photospheric granulation, chromospheric evaporation, star formation, galaxy formation), an MHD approach (protoplanetary disks, solar magnetic fields, the Hale cycle), or N-body problems (planetary spacing, planetary rings and moons), have to be studied by numerical simulations. Numerical solutions of coupled differential equation systems can now easily be obtained with numerical minimization algorithms (in form of time profiles  $X(t)$ ,  $Y(t)$ , or phase diagrams  $Y(X)$ , see Fig. (18).

### 8. CONCLUSIONS

In this multi-disciplinary review we provide, for the first time, a compilation of 17 astrophysical phenomena that have been associated with self-organization mechanisms. The conclusions of this study are:

1. Self-organization is a very multi-disciplinary subject that has been applied in planetary physics, solar physics, stellar physics, galactic physics, cosmology, ionospheric physics, magnetospheric physics, laboratory plasma physics, condensed matter physics, chemistry, biology, social science, and computer science.
2. Self-organizing systems in astrophysics create spontaneous *order out of randomness*, during the evolution from an initially disordered system to an ordered and more regular quasi-stationary system, via: (i) quasi-periodic limit-cycle dynamics, and/or (ii) resonances (i.e., harmonic mechanical resonances, or harmonics of the gyrofrequency).
3. Self-organizing processes are not controlled from outside, but are driven by global forces (inside an open dissipative system), such as gravity, rotation, thermal pressure, or acceleration of nonthermal particles, in the case of astrophysical applications.

4. The limit-cycle behavior of astrophysical self-organization processes occurs due to a positive feedback mechanism that couples with the primary driver. This feedback mechanism is often an instability, such as the magneto-rotational instability, the Rayleigh-Bénard convection instability, turbulence, vortex attraction, magnetic reconnection, plasma condensation, or a loss-cone instability.
5. Physical models of an astrophysical self-organization process require a hydrodynamic approach (photospheric granulation, chromospheric evaporation, star formation, galaxy formation), an MHD approach (protoplanetary disks, solar magnetic field, Hale cycle), or N-body simulations (planetary spacing, planetary rings and moons).
6. The entropy in self-organization processes is decreasing during the evolution from an initially disordered system to a self-organized limit-cycle behavior, in contrast to random processes where the entropy increases, or to self-organized criticality systems where the entropy remains invariant in the long-term time average.
7. The Lotka-Volterra equation system represents a useful tool to study the dynamical behavior of nonlinear dissipative systems, which are likely to evolve into a limit-cycle behavior for long-lived quasi-stationary phenomena.

While the modeling of systems with self-organization was severely hampered in the past, due to the mathematical difficulty of finding analytical solutions for coupled integro-differential equation systems, it is expected that the use of numerical computer simulations will be capable to produce realistic models in the future, for hydrodynamic, MHD, and N-body problems.

### APPENDIX A: Keplerian Orbits

In principle, the Keplerian orbits of planets can be understood as a limit cycle of a self-organizing system. The dynamics of two planets can be written in a Hamiltonian form (Nesvorny and Vokrouhlick 2016),

$$H = H_K + H_{per} = \sum_{j=1}^2 \left( \frac{p_j^2}{2\mu_j} - G \frac{\mu_j M_j}{r_j} \right) + H_{per} , \quad (A1)$$

where  $H$  is the total Hamiltonian,  $H_K$  is the Keplerian part,  $H_{per}$  is the perturbation part,  $M_*$  is the solar mass,  $M_j = m_j + M_*$  and  $\mu_j = m_j M_*/M_j$  the reduced masses. If we neglect the perturbations, the Hamiltonian form is equivalent to the conservation of kinetic and gravitational potential energy,  $E_{kin} + E_{grav} = (1/2)mv^2 - GM_*m/r = 0$ , from which the following relationship between the distance  $r$  and velocity  $v$  results,

$$v(r) = \sqrt{\frac{2GM}{r}} \quad (A2)$$

We show this relationship between the planet distance  $r$  and the planet velocity  $v(r)$  in the phase space  $[r, v]$  in Fig. (2 dotted curve). For each of the 10 planets (including Ceres and Pluto), there is a fixed point  $[r_i, v_i], i = 1, \dots, 10$  that represents an attractor for the planet motion in phase space. For planets that have a circular orbit with no eccentricity, the Keplerian planet motion is confined to a constant single fixed point in phase space ( $r_i = const, v_i = const$ ). However, all planet orbits move on ellipses with some eccentricity  $e$ , in the cartesian space  $[x, y]$ . The minimum  $r_{min}$  and maximum distance  $r_{max}$  are given by the eccentricity  $e = c/a$ ,

$$\begin{aligned} r_{min} &= a(1 - e) \\ r_{max} &= a(1 + e) \end{aligned} , \quad (A3)$$

where  $a$  is the major axis of the ellipse,  $b$  is the minor axis,  $c = \sqrt{a^2 - b^2}$  is the distance of one ellipse focal point (where the Sun is) from the center of the ellipse, and  $e = c/a$  is the eccentricity. Defining the mean distance with  $a$  and the orbital period with  $T$ , we retrieve Kepler's third law,  $a^3 \propto T^2$ , using  $v = 2\pi R/T$  and Eq. (A2).

We show the planet motion in phase space  $[r_i, v_i]$  in Fig. (2 thick curve segments), which cover the range of  $r_{min} \leq r \leq r_{max}$  for each planet. We see that only Mercury and Pluto cover an appreciable distance in phase space, because they have the largest eccentricities of  $e_{mercury} = 0.2056$  and  $e_{pluto} = 0.2488$ . Therefore, every planet performs an oscillatory motion around their mean distance (from the Sun) with an orbital period  $T$  that can be considered as a limit cycle. Gravitational perturbations will alter the Keplerian orbits slightly, which we neglected here. The orbital period  $T$  marks the temporal scale that is self-organized in this system. In addition, the system self-organizes low harmonic ratios between adjacent planet pairs, which is necessary to warrant long term stability of the planet system. These quantized harmonic ratios mark the spatial scales. Therefore, a planet system self-organizes both temporal and spatial scales.

### APPENDIX B: Coupled Differential Equations

A basic analytical system that exhibits oscillatory limit-cycle behavior can be described by the following non-homogeneous linear differential equation system (Aschwanden and Benz 1988),

$$\begin{aligned} dX/dt &= b_1 + a_{11}X + a_{12}Y \\ dY/dt &= b_2 + a_{21}X + a_{22}Y \end{aligned} . \quad (B1)$$

This equation system contains linear terms only (in  $X(t)$  and  $Y(t)$ ), which is appropriate for the dynamic system behavior under the influence of small perturbations. The general (complex) solution depends on the value of the discriminant  $D$  and trace  $S$  of the non-homogeneous equation,

$$\begin{aligned} S &= \frac{1}{2}(a_{11} + a_{22}) \\ D &= (a_{11}a_{22} - a_{12}a_{21}) \end{aligned} \quad (B2)$$

The general complex solution of the non-homogeneous differential equation system for  $(S^2 - D) \neq 0$  is given by,

$$\begin{aligned} X(t) &= X_1 \exp^{z_i t} + X_0 \\ Y(t) &= Y_1 \exp^{z_i t} + Y_0 \end{aligned} \quad (B3)$$

where the exponential coefficient has two solutions,

$$\begin{aligned} z_1 &= S + [(S^2 - D)]^{1/2} \\ z_2 &= S - [(S^2 - D)]^{1/2} \end{aligned} \quad (B4)$$

For the linearly dependent case of  $(S^2 - D) = 0$  the general solution is given by

$$\begin{aligned} X(t) &= (X_2 t + X_1) \exp^{St} + X_0 \\ Y(t) &= (Y_2 t + Y_1) \exp^{St} + Y_0 \end{aligned} \quad (B5)$$

The non-homogeneous coefficients are,

$$\begin{aligned} X_0 &= (b_2 a_{12} - b_1 a_{22}) / D \\ Y_0 &= (b_1 a_{21} - b_2 a_{11}) / D \end{aligned} \quad (B6)$$

Using  $X_1$  and  $X_2$  as free parameters, the coefficients  $Y_1$  and  $Y_2$  are,

$$\begin{aligned} Y_1 &= \frac{1}{a_{12}} \left( \frac{a_{22} - a_{11}}{2} \right) X_1 \\ Y_2 &= \frac{1}{a_{12}} \left( \frac{a_{22} - a_{11}}{2} \right) X_2 + \frac{1}{a_{12}} X_1 \end{aligned} \quad (B7)$$

Since the exponential coefficient  $z_i$  is a complex number, one can split it into a real part  $\rho_i$  and an imaginary part  $\omega_i$ ,

$$\begin{aligned} z_i &= \rho_i + i \omega_i \\ \rho_i &= \text{Re}[S \pm (S^2 - D)^{1/2}] \\ \omega_i &= \text{Im}[S \pm (S^2 - D)^{1/2}] \end{aligned} \quad (B8)$$

Physically,  $\omega_i$  describes the frequency of the oscillations, and  $\rho_i$  denotes the growth (or negative damping) rate of the perturbation. Using these variables, the time-dependent solution is the classical solution of two coupled oscillators:

$$\begin{aligned} X(t) &= X_1 \exp^{\rho_i t} \cos(\omega_i t) + X_0 \\ Y(t) &= Y_1 \exp^{\rho_i t} \cos(\omega_i t - \delta) \left[ \frac{(\rho_i - a_{11})^2 + \omega_i^2}{a_{12}^{1/2}} \right]^{1/2} + Y_0 \end{aligned} \quad (B9)$$

The phase difference  $\delta$  is

$$\tan(\delta) = \frac{-\omega_i}{\rho_i - a_{11}} \quad (B10)$$

The special case of an undamped oscillation ( $\rho_i=0$ ) requires  $S = 0$  and  $D > 0$ . The temporal functions  $X(t)$  and  $Y(t)$  of the two coupled oscillators is then

$$\begin{aligned} X(t) &= X_1 \cos(\omega_i t) + X_0 \\ Y(t) &= X_1 \cos(\omega_i t - \delta) \left( \frac{-a_{21}}{a_{12}} \right)^{1/2} + Y_0 \\ \omega_i &= \pm \sqrt{D} = \pm (a_{11}a_{22} - a_{12}a_{21})^{1/2} \\ \tan(\delta) &= \omega_i / a_{11} \end{aligned} \quad (B11)$$

which corresponds to a limit cycle with period  $\omega_i$ , fixpoint  $(X_0, Y_0)$ , and phase delay  $\delta$ .

### APPENDIX C: The Hopf Bifurcation

Another nonlinear system that predicts limit-cycle behavior is the so-called *Hopf bifurcation* (Hopf 1942), which is described in many textbooks (e.g., Schuster 1988). A simple Hopf bifurcation generates a limit cycle starting from a fixed point. A differential equation of the Hopf bifurcation can be written in polar coordinates  $[r, \theta]$ ,

$$\begin{aligned} dr/dt &= -(\rho r + r^3) \\ d\theta/dt &= \omega \end{aligned} \quad (C1)$$

which has the following analytical solution,

$$\begin{aligned} r^2(t) &= \frac{\rho r_0^2 \exp(-2\rho t)}{r_0^2 [1 - \exp(-2\rho t)] + \rho} \\ \theta(t) &= \omega t \end{aligned} \quad (C2)$$

for the initial conditions  $r_0 = r(t=0)$  and  $\theta(t=0) = 0$ . For  $\rho \geq 0$ , the trajectory approaches the origin at the fixed point  $r_\infty = 0$  and becomes stationary.

For negative values,  $\rho < 0$ , it converges to a limit cycle  $r_\infty = r(t=\infty) = \sqrt{|\rho|} > 0$ .

The differential equation system in polar coordinates  $[r, \theta]$  can be transformed into Cartesian coordinates  $[X, Y]$  by using

$$\begin{aligned} X &= r \cos(\omega t) \\ Y &= r \sin(\omega t) \end{aligned} \quad (C3)$$

which yields

$$\begin{aligned} dX/dt &= -[\rho + (X^2 + Y^2)]X - Y\omega \\ dY/dt &= -[\rho + (X^2 + Y^2)]Y + X\omega \end{aligned} \quad (C4)$$

Linearizing with respect to the origin yields,

$$\frac{df}{dt} = Af, \quad (C5)$$

with  $f = [\Delta X, \Delta Y]$  and the  $A$  the matrix

$$A = \begin{pmatrix} -\rho & -\omega \\ \omega & -\rho \end{pmatrix}, \quad (C6)$$

which has the eigenvalues,

$$\lambda = -\rho \pm i\omega. \quad (C7)$$

### APPENDIX D: The Lotka-Volterra Equation System

The Lotka-Volterra equation system (Lotka 1925; Volterra 1931) is a paradigm of a nonlinear dissipation process, with cyclic (oscillatory) behavior in some parameter space. In the simplest terms it can be written as a coupled first-order, nonlinear, differential equation system containing the time-dependent variables  $X(t)$  and  $Y(t)$ , and coefficients  $k_1, k_2, k_3$ ,

$$\begin{aligned} dX/dt &= k_1 X - k_2 XY \\ dY/dt &= k_2 XY - k_3 Y \end{aligned} \quad (D1),$$

with  $k_1, k_2, k_3$  being positive coefficients. The rate of change in the first variable  $X(t)$  is specified by a growth rate  $k_1$ , while the (negative) dissipation rate  $k_2$  is coupled to the product of both variables,  $X(t)Y(t)$ . The rate of change in the second variable  $Y(t)$  is specified by a decay rate  $k_3$ , while the (positive) dissipation rate  $k_2$  has the opposite sign.

In ecology (e.g., May 1974), the two variables were designated to some predator and pray populations that compete for life, such as foxes and rabbits.

This equation system has a periodic solution, which is called the limit cycle, also called a critical point or attractor. Critical points occur when  $dX/dt = 0$  and  $dY/dt = 0$ , which yields a stationary point in phase space at  $(X_0, Y_0)$ , representing a non-vanishing stationary solution,

$$\begin{aligned} X_0 &= (k_3/k_2) \\ Y_0 &= (k_1/k_2) \end{aligned} \quad (D2)$$

For small perturbations not too far off the limit cycle, we can describe the cyclic dynamics with,

$$\begin{aligned} X(t) &= X_0 + x \exp(\omega t) \\ Y(t) &= Y_0 + y \exp(\omega t - \delta) \end{aligned} \quad (D3)$$

where the small amplitudes obey  $|x/X_0| \ll 1$  and  $|y/Y_0| \ll 1$ , and  $\delta$  represents a phase delay. One can then derive the following dispersion relation,

$$\omega^2 + k_1 k_3 = 0. \quad (D4)$$

The real part of the frequency is zero,  $Re(\omega_n) = 0$ , while the imaginary part characterizes an oscillation,  $Im(\omega) = \pm \sqrt{k_1 k_3}$ . The dynamics is essentially a circular motion in phase space  $Y(X)$ , which corresponds to  $X(t) = X_0 + x \sin \omega t$  and  $Y(t) = Y_0 + y \sin \omega(t - t_0)$ .

Many nonlinear systems, however, are far off an equilibrium state. In order to study the nonlinear behavior of the Lotka-Volterra equation system, we can transform the variables in terms of the limit-cycle fixpoint  $(X_0, Y_0)$ ,

$$\begin{aligned} X &= X_0 x = (k_3/k_2)x \\ Y &= Y_0 y = (k_1/k_2)y \end{aligned} \quad (D5)$$

Inserting this parameterizaion (D5) into the original Lotka-Volterra equation system (D1), multiplying them with  $(y - 1)$  and  $(x - 1)$ , and subtracting them from each other yields then

$$\left[ (x - 1) \frac{dy}{dt} - (y - 1) \frac{dx}{dt} \right] = k_3(x - 1)^2 y + k_1(y - 1)^2 x \quad (D6)$$

Substituting the variables  $(x, y)$  with polar coordinates  $(\rho, \omega)$  according to,

$$\begin{aligned} (x - 1) &= \rho \cos \omega \\ (y - 1) &= \rho \sin \omega \end{aligned} \quad (D7)$$

yields then the function,

$$\Phi(\omega) := \frac{d\omega}{dt} = k_1 x \sin^2 \omega + k_3 y \cos^2 \omega \quad (D8)$$

which can be integrated to obtain the time dependence of the polar coordinate  $\omega(t)$

$$\omega(t) = \int_0^{t'} \Phi(\omega) dt', \quad (D9)$$

The  $(x, y)$  coordinates are found by the transcendental solution of the Lotka-Volterra equation,

$$x^{-k_3} e^{k_3 x} = C y^{k_1} e^{-k_1 y} \quad (D10)$$

We show a typical dynamic solution in Fig. (18 bottom), computed by a numerical code that obtains solutions for  $X(t)$  and  $Y(t)$  directly by minimizing the coupled first-order, nonlinear, differential equation system given in Eq. (D1), for the coefficient  $k_1 = 0.5, k_2 = 2.0, k_3 = 0.5$ . The time-dependent solutions  $X(t)$  and  $Y(t)$  are shown in the bottom left panel of Fig. (18), and a phase plot  $Y(X)$  is shown in the top right panel of Fig. (18). We see that the trajectory in phase space is convergent towards the limit-cycle solution, starting from highly nonlinear amplitude oscillations far off the equilibrium, while the system asymptotically converges towards the attractor  $(X_0, Y_0)$ , with gradually diminishing amplitude.

*Acknowledgements:* The author acknowledges the hospitality and partial support for two workshops on “Self-Organized Criticality and Turbulence” at the *International Space Science Institute (ISSI)* at Bern, Switzerland, during October 15-19, 2012, and September 16-20, 2013, as well as constructive and stimulating discussions (in alphabetical order) with Robert Cameron, Sandra Chapman, Paul Charbonneau, Cavid Collins, Daniel Fabrycky, Clara Froment, Hermann Haken, Henrik Jeldtoft Jensen, Lucy McFadden, Maya Paczuski, Jens Juul Rasmussen, John Rundle, Loukas Vlahos, and Nick Watkins. This work was partially supported by NASA contract NNX11A099G “Self-organized criticality in solar physics”.

## REFERENCES

- Abbett, W.P. 2007, ApJ 665:1469.
- Abramenko, V.I., Yurchyshyn, V.B., Goode, P.R., Kitiashvili, I.N., and Kosovichev, A.G. 2012, ApJ 756, L27.
- Aburjania, G.D., Kharshiladze, O.A., and Chargazia, Kh.Z. 2013, Geomagnetism and Aeronomy 53/6, 750.
- Alexander, R.D., Clarke, C.J., and Pringle, J.E. 2006, MNRAS 369, 216.
- ALMA Partnership, Brogan, C.L, Perez, L.M. et al. 2015, ApJL 808, L3.
- Ambjorn, J., Jurkiewicz, J., and Loll, R. 2008, Internat J. Modern Phys. D, 17/13-14, 2515.
- Anderson, P.W., Alpar, M.A., Pines, D., and Shaham, J. 1981, in *Pulsars* (eds. Sieber, W. and Wielebinski, R.), IAU, P. 299.
- Andrews, S.M., Wilner, D.J., Espaillat, C., et al. 2011, ApJ 732, 42.
- Aqua, J.N., Berbezier, I., Favre, L., Frisch, T., Ronda, A. 2013, Phys. Rep. 522/2, 59.
- Aschwanden, M.J. 1987, SP 111, 113.
- Aschwanden, M.J. and Benz, A.O. 1988, ApJ 332, 466.
- Aschwanden, M.J., Benz, A.O., Dennis, B.R. and Gaizauskas, V. 1993, ApJ 416, 857.
- Aschwanden, M.J., Benz, A.O., and Montello, M.L. 1994, ApJ 431, 432.
- Aschwanden, M.J. 2011, *Self-organized criticality in astrophysics. The statistics of nonlinear processes in the universe*, New York: Springer/PRAXIS.
- Aschwanden, M.J., Crosby, N., Dimitropoulou, M., et al. 2016, Space Science Reviews 198, 47.
- Aschwanden, M.J. 2018, New Astronomy 58C, 107, <https://doi.org/10.1016/j.newast.2017.08.002>
- Aschwanden, M.J. and Scholkmann, F. 2017, Galaxies 5(4), 56.
- Ashby, W.R. 1947, J. Gen. Psychology 37, 125.
- Auchère, F., Froment, C., Bocchialini, K., et al. 2016, ApJ 825, 110.
- Auer, T. 1999, PhD Thesis, University of Heidelberg, Germany.
- Babcock, H.W. 1961, ApJ 133, 572.
- Bai, X.N. 2015, ApJ 798, 84.
- Bai, X.N. and Stone, J.M. 2014, ApJ 796, 31.
- Baines, K.H., Momary, T.W., Fletcher, L.N., et al. 2009, Planetary and Space Science. 57 (14-15): 1671.
- Bak, P., Tang, C., and Wiesenfeld, K. 1987, PhRvL 59/4, 381.
- Balbus, S.A. and Hawley, J.F. 1991, ApJ 376, 214.
- Balbus, S.A. and Terquem, C. 2001, ApJ 552, 235.
- Bardakov, V.M. and Stepanov, A.V. 1979, Sov. Astron. Lett. 5(5), 247.
- Baruteau, C. and Papaloizou, J.C.B. 2013, ApJ 778, 7.
- Benacek, U., Karlicky, M., Yasnov, L.V. et al. 2017, AA 598, A108.
- Benisty, M., Juhasz, A., Boccaletti, A., et al. 2015, AA 578, L6.
- Bennett, C.L., Larsen, D., Weiland, J.L. 2013, ApJ 208, 20B.

- Benz, A.O. 1993, *Plasma astrophysics, kinetic processes in solar and stellar coronae*, Kluwer Academic Publishers, Dordrecht, The Netherlands.
- Berney, M. and Benz, A.O. 1978, AA 65, 369B.
- Béthune, W., Lesur, G., and Ferreira, J. 2016, AA 589, A87.
- Béthune, W., Lesur, G., and Ferreira, J. 2017, AA 600, A75.
- Binney, J. and Merrifield M. 1998, *Galactic Astronomy*, Princeton University Press: Princeton.
- Bland-Hawthorn, J. and Gerhard, O. 2016, ARAA 54, 529.
- Birnstiel, T., Dullemond, C.P., and Pinilla, P. 2013, AA 550, L8.
- Biskamp, D. 2003, *Magnetohydrodynamic Turbulence*, Cambridge: University of Cambridge.
- Blagg, M.A. 1913, MNRAS 73, 414.
- Bodifee, G. 1986, *Astrophys. Space Sci.* 122, 41.
- Boesiger, P., Brun, E., and Meier, D. 1978, *Phys. Rev. A* 18/2, 671.
- Boggess, N.W., Mather, J.C., Weiss, R., et al. 1992, *ApJ* 397, 420.
- Brandenburg, A., Kemel, K., Kleeorin, N., et al. 2012, *ApJ* 749, 179.
- Bray, W.C. 1921, *J. Amer.Chem.Soc.* 43(6), 1262,
- Brooks, R.R. 2009, *Internat. J. Distr. Sensor Networks* 5, 201.
- Brown, B.P., Browning, M.K., Brun, A.S., et al. 2010, *ApJ* 711, 424.
- Brown, E.W. and Shook, C.A. 1933, *Planetary Theory*, reprinted 1965, New York: Dover.
- Buchler, J.R., Kollath, Z., Serre, T., and Mattei, J. 1996, *ApJ* 462, 489.
- Bullock, J.S. and Boylan-Kolchin, M. 2017, ARAA 55, 343.
- Cabrit, S., Ferreira, J., and Dougados, C. 2011, in *Jet at All Scales* (eds. Romero, G.E., Sunyaev, R.A., and Belloni, T.), IAU Symposium Vol. 275, 374.
- Camazine, S., Deneubourg, J.L., Frank, N.R., Sneyd, J., Theraulaz, G., and Bonabeau, E. 2001, *Self-Organization in Biological Systems*, Princeton University Press.
- Cameron, R.H. and Schüssler, M. 2017, *ApJ* 843/2, id. 111.
- Cannizzo, J.K., Goodings, D.A., and Mattei, J.A. 1990, *ApJ* 357, 235.
- Caplan, M.E. and Horowitz, C.J. 2017, *Rev.Mod.Phys.* 89/4, id. 041002.
- Cassak, P.A., Mullan, D.J. and Shay, M.A. 2008, *ApJ* 676, L69.
- Cargill, P.J. and Bradshaw, S.J. 2013, *ApJ* 772, 40.
- Carroll, S. 2004, *An Introduction to general Relativity Spacetime and Geometry*, Addison Wesley, p.329.
- Cen, R. 2014, *ApJL* 785, L21.
- Chandrasekhar, S. 1961, *Hydrodynamic and Hydromagnetic Stability*, Clarendon Press, Oxford.
- Chang, Y.F. 2013, *Internat. J. Sciences* 2, 58.
- Charbonneau, P. 2014, ARAA 52, 251.
- Chen, B., Bastian, T.S., Gary, D.E. and Ju, J. 2011, *ApJ* 736, 64.
- Cheng, K.S., Pines, D., Alpar, M.A., and Shaham, J. 1988, *ApJ* 330, 835.

- Chernov, G.P. 1976, *Sov. Astron.* 20, 582.
- Chernov, G.P. 1990, *SP* 130, 75.
- Chernov, G.P., Yan, Y., and Fu, Q. 2003, *AA* 406, 1071.
- Chernov, G.P. 2006, *SSRv* 127, 195.
- Chernov, G.P. 2011, *Fine structure of solar radio bursts*, ASSL 375: Springer Heidelberg
- Chernov, G.P. 2012, in *Horizons in World Physics* (Ed. Reiner A.), V 278, Nova Science Publisher: New York, Ch. 1, p.1.
- Chernov, G.P., Fomichev, V.V., Tan, B.L. et al. 2015, *SP* 290, 95.
- Chernov, G.P. 2016, in Chapter 5: *Latest News on Zebra Patterns in the Solar Radio Emission*, p. 101.
- Chernov, G.P., Fomichev, V.V., Yan, Y., et al. 2017, *Geomagnetism and Aeronomy* 57(6), 738.
- Cheung, M.C.M., Sch’ussler, M., and Moreno-Insertis, F. 2007, *A&A* 467, 703.
- Cheung, M.C.M. and Isobe, H. 2014, *Living Rev. Solar Phys.* 11:3.
- Cheung, M.C.M., van Driel-Gesztelyi, L., Martinez Pillet, V., and Thompson, M.J. 2017, *SSRv* 210, 317.
- Chumak, O.V. 2007, *Odessa Astron. Publ.* 20, 27.
- Collins, D.C., Kritsuk, A.G., Padoan, P., et al. 2012, *ApJ* 750:13.
- Colombo G., Franklin, F.A., Shapiro, I.I. 1974, *Astron. J.* 79, 61.
- Combes, F. and Gerin, M. 1985, *A&A* 150, 327.
- Conslice, C.J. 2014, *ARAA* 52, 291.
- Consolini, G., Tozzi, R., and De Michelis, P. 2009, *AA* 506, 1381.
- Cox, M.P., Ertl, G., Imbuhl, R. 1985, *Phys. Rev. Lett.* 54/15, 1725.
- Crida, A., Morbidelli, A., and Masset, F. 2006, *Icarus* 181, 587.
- Daly, E. and Porporato, A. 2006, *Phys.Rev. E* 74/4, id. 041112.
- Dabrowski, B.P. and Benz, A.O. 2009, *AA* 504, 565.
- De Groof, A., Bastiaensen, C., Müller, D.A.N., et al. 2005, *AA* 443, 319.
- Demirel 2007, *Nonequilibrium thermodynamics, Transport and rate processes in physical, chemical, and biological systems*, 2nd ed., Amsterdam: Elsevier.
- DeNeto, M., Maia, L.A., and Carneiro, S. 2007, *Chaos, Solitons, and Fractals* 21(1), 21.
- Drummond, L.V. and Melatos, A. 2017, *MNRAS* 472, 4851.
- Dyudina, U.A., Ingersoll, A.P., Ewad, S.P. et al. 2006, arXiv:1506.00664v1.
- Eckmann, J.P. and Ruelle, D. 1992, *Physica D* 56, 185.
- Elmegreen, D.M. and Elmegreen, B.G. 1987, *ApJ* 314, 3.
- Elmegreen, B.G. 2011, *ApJ* 731, 61.
- Espinoza, C.M., Lyne, A.G., Stappers, B.W., and Kramer, M. 2011, *MNRAS* 414/2, 1679.
- Faucher-Giguere, C.A. and Angles-Alcazar D. 2017, quoted in *New Scientist*, 5 August 2017, p.16.
- Fletcher, L.N., Irwin, P.G.J., Orton, G.S., et al. 2008, *Science* Vol. 319, Issue 5859, 79.
- Francis, C. and Anderson, E. 2009, *Proc. Roy. Soc.* A465, 3425.

- Franklin, F.A., Colombo, G., Cook, A.F. 1971, *Icarus* 15, 80.
- Franklin, F.A., Marsden, B.G., Williams, J.G., Bardwell, C.M. 1975, *Astron. J.* 80, 729.
- Freeman, K.C. 2017, *ARAA* 51, 1.
- Froment, C., Auchère, F., Bocchialini, K. et al. 2015, *ApJ* 807, 158.
- Froment, C., Auchère, F., Aulanier, G. et al. 2017, *ApJ* 835, 272.
- Fulgenzi, W., Melatos, A., and Hughes, B.D. 2017, *MNRAS* 470/4, 4307.
- Fukagawa, M., Tsukagoshi, T., Momose, M., et al. 2013, *PASJ* 65, L14.
- Gacs, P. 2000, *J. Stat. Phys.* 103(1/2), 45.
- Ge, X.H. and Wang, C.C. 2017, eprint arXiv:1709.03290 .
- Geach, J.E. 2012, *MNRAS* 419/3, 2633.
- Georgiev, G., Chatterjee, A., and Iannacchione, G. 2016, eprint arXiv:1612.03727.
- Georgoulis, M.K. 2005, *Solar Phys.* 228, 5.
- Georgoulis, M.K. 2012, *Solar Phys.* 276, 161.
- Gerola, H. and Seiden, P.E. 1978, *ApJ* 223, 129.
- Godfrey, D.A. 1988, *Icarus* 76(2), 335.
- Gor'kavyi, N.N. and Fridman, A.M. 1991, *Priroda* 1, 56.
- Grassberger, P. and Procaccia, I. 1983a, *Phys. Rev. Lett.* 50, 346.
- Grassberger, P. and Procaccia, I. 1983b, *Physica* 9D, 189.
- Greenberg, R. 1973, *Astron. J.* 78, 338.
- Guennou, C., Auchère, F., Soubrie, E., et al. 2012a, *ApJS* 203, 25.
- Guennou, C., Auchère, F., Soubrie, E., et al. 2012b, *ApJS* 203, 26.
- Guennou, C., Auchère, F., Klimchuk, J.A., et al. 2013, *ApJ* 774, 31.
- Haken, H. 1983, *Synergetics, an Introduction: Nonequilibrium Phase Transitions and Self-Organisation in Physics, Chemistry, and Biology*, New York: Springer.
- Haken, H. 2008, *Scholarpedia*, 3(8):1401.
- Hale, G.E. 1908, *ApJ* 28, 315.
- Harding, A.K., Shinbrot, T., and Cordes, J.M. 1990, *ApJ* 353, 588.
- Hasegawa, A. 1985, *Advances Phys.* 34, 1.
- Hathaway, D.H. 2015, *Living Rev. Solar Phys.* 12, 4.
- Heckman, T.M. and Best, P.N. 2014, *ARAA* 52, 589.
- Hinshaw, G.F., Larson, D., Komatsu, E. et al. 2013, *ApJS* 208, 19H.
- Hogan, C.J. 1991, *ApJ* 369, 300.
- Hopf, E. 1942, *Math. Naturwiss. Klasse, Sächs. Akademie der Wissenschaften, Leipzig*, 94, 1.
- Hotta, H., Rempel, M., and Yokoyama, T. 2014, in *Numerical Modeling of Space Plasma Flows* (eds. Pogorelov, N.V., Audit, E., and Zank, G.P.), *ASP Conf. Ser.* 498, 154.
- Ikeuchi, S. and Tormita, H. 1983, *PASJ* 35, 77.

- Imada, S. and Zweibel, E.G. 2012, ApJ 755, id. 93.
- Izakov, M.N. 1997, Physics Uspekhi 40/10, 1035.
- Jeans, J. 1915, MNRAS 76, 60.
- Jin, L. 1996, ApJ 457, 798.
- Kaladze, T.P., Pokhotelov, O.A., Shah, H.A., Khan, M.I., and Stenflo, L. 2008, J. Atmos. Solar-Terr. Phys. 70/13, 1607.
- Kalapotharakos, C., Voglis, N., and Contopoulos, G. 2004, AA 438, 905.
- Käpylä, P.J., Mantere, M.J., and Brandenburg, A. 2012, ApJ 755, 22.
- Karlicky, M., Barta, M., Jiricka, K., et al. et al. 2001, AA 375, 638.
- Karlicky, M. and Yasnov, L.V. 2015, AA 581, A115.
- Kaufman, S.A. 1993, *The origins of order: Self-organization and selection in evolution*, Oxford University Press.
- Kaufman, S.A. 1996, *At home in the universe: The search for the laws of self-organization and complexity*, Oxford University Press.
- Kernbach, S. 2008 *Structural self-organization in multi-agents and multi-robotic systems*, Logos Verlag, Berlin.
- Kitiashvili, I.N., Kosovichev, A.G., Wray, A.A., and Mansour, N.N. 2010, ApJ 719, 307.
- Koepferl, C.M., Ercolano, B., Dale, J., et al. 2013, MNRAS 428, 3327.
- Kohonen, T. 1989, *Self-Organization and Associative Memory* (3rd ed.), Berlin:Springer.
- Kolmogorov, A. et al. (1937), Moscow Univ. Bull. Math A 1: 1.
- Kospal, A., Ardila, D.R., Moor, A., and Abraham, P. 2009, ApJL 700, L73.
- Krall, K.R. and Antiochos, S.K. 1980, ApJ 242, 374.
- Krishan, V. 1991, MNRAS 250, 50.
- Krishan, V. 1992, Indian J. Phys. 66B/5,6, 569.
- Kritsuk, A.G., Ustygov, S.D., and Norman, M.L. 2011, in Computational Star formation, Proc, IAU 270, 179.
- Kuin, N.P.M. and Martens, P.C.H. 1982, AA 108, L1.
- Kuijpers, J. 1975, *Collective wave-particle interactions in solar type IV radio sources*, PhD Thesis, Utrecht University.
- Kuijpers, J. 1978, AA 69, L9.
- Kuijpers, J. 1980, in *Theory of type iV dm Bursts* (eds. M.R. Kundu and T.E. Gergely), Physics of the Sun, p. 341.
- Kunz, M.W. and Balbus, S.A. 2004, MNRAS 348, 355.
- Kunz, M.W. 2008, MNRAS 385, 1494.
- Kunz, M.W. and Lesur, G. 2013, MNRAS 434, 2295.
- Kuznetsov, A.A. and Tsap, Y.T. 2007, SP 241, 127.
- LaBelle, J., Treumann, R.A., Yoon, P.H. et al. 2003, ApJ 593, 1195.
- Laplace, P.S. 1829, *Mechanique Céleste*, Vols. I, IV. Boston: Hillard, Gray, Little and Wilkins.
- Law, D., Shapley, A.E., Checlair, J., and Steidel, C.C. 2015, ApJ 808, 160.
- Lecar, M. and Franklin, F.A. 1973, Icarus 20, 422.
- L'Ecuyer, T.S., Beaudoin, H.K., Rodell, M., et al. 2015, J. Climate 28, 8319.

- Lehn, J.M. 2002, *Science* 295, 2400.
- Leroy, J.O. 1972, *SP* 25, 413.
- Lesur, G., Kunz, M.W., and Fromang, S. 2014, *AA* 566, A56.
- Leydesdorff, L. 1993, *J. Social Evolutionary Systems* 16, 331.
- Leysner, T.B. 2001, *Space Science Rev.* 98/3, 223.
- Libeskind, N.I., van de Weygaert, R., Cautun, M. et al. 2017, *MNRAS* 473, 1195, arXiv:1705.03021v1 .
- Lindblad, B. 1925, *Arkiv for Matematik, Astronomi, och Physik* 19A, 21, 27, 35.
- Lindblad, B. 1926, *Uppsala Medd.* No. 3.
- Lindblad, B. 1927, *MNRAS* 87, 553.
- Lin, C.C. and Shu, F. 1964, *ApJ* 140, 646.
- Link, F. 1975, *Planet. Space Sci.* 23, 805.
- Lissauer, J.J. and Murray, C.D. 2007, *Solar System Dynamics: Regular and Chaotic Motion*, in *Encyclopedia of the Solar System*, Academic Press.
- Lorenz, E.N. 1963, *Deterministic nonperiodic flow*, *J. Atmos. Sci.* 20, 130.
- Lotka, A.J. 1925, *Elements of Physical Biology*, Williams and Wilkins.
- Love, et al. 2005, *Chem Rev.* 105(4), 1103.
- Luger, R., Sestovic, M., Druse, E. et al. 2017, *Nature Astronomy*, Vol. 1, id. 0129.
- Madau, F. and Dickinson, M. 2014, *ARAA* 52, 415.
- Mannattil, M., Gupta, H., and Chakraborty, S. 2016, *ApJ.* 833, 208.
- Marcus, P.S. 1993, *ARAA* 31, 523.
- Marov, M.Y. and Kolesnichenko, V. 2013, *Astrophysics and Space Science Library* 389.
- Marsden, B.G. 1970, *Astron. J.* 75, 206.
- Martinez-Sykora, J., Hansteen, V., and Carlsson, M. 2008, *ApJ* 679, 871.
- Martinez-Sykora, J., Hansteen, V., and Carlsson, M. 2009, *ApJ* 702, 129.
- Martinez-Sykora, J., De Pontieu, B., Testa, P., and Hansteen, V. 2011, *ApJ* 743, 23.
- Mather, J.C., Hauser, M.G., Bennett, C.L., et al. 1991, *Adv. Space Res.* 11(2), 181.
- Maxworthy, T. and Redekopp L.G. 1976, *Icarus* 29, 261.
- May, R.M. 1974, *Model ecosystems*, Princeton.
- McCaughrean, M.J. and O'dell, C.R. 1996, *Astron. J.* 111, 1977.
- McFadden, L.A., Weissman, P.R., and Johnson, T.V. 1999, (second edition 2007), *Encyclopedia of the Solar System*, Academic Press, New York.
- McLean, D.J. and Sheridan, K.V. 1973, *SP* 32, 485.
- McWilliams, J.C., Weiss, J.B., and Yavneh, I. 1994, *Science* 264/5157, 410.
- Melatos, A., Peralta, C., and Wyithe, J.S.B. 2008, *ApJ* 672, 1103.
- Melatos, A. and Warszawski, L. 2009, *ApJ* 700, 1524.
- Melatos, A. and Warszawski, L. 2015, *ApJ* 807, 132.

- Mendoza-Briceno, C.A., Sigalotti, L. Di G., and Erdelyi, R. 2005, ApJ 624, 1080.
- Middleditch, J., Marshall, F.E., Wang, Q.D., et al. 2006, ApJ 652, 1531.
- Miesch, M.S., Elliott, J.R., Toomre, J., et al. 2000, ApJ 532, 593.
- Miles, C.E. and Keener, J.P. 2017, J.Phys. A: Math. Theo. 50/42, id. 425003.
- Mills, S.M., Fabrycky, D.C., Migaszewski, C. et al. 2016, Nature 533, Issue 7604, 509.
- Mineshige, S., Takeuchi, M., and Nishimori, H. 1994a, ApJ 435, L125.
- Mineshige, S., Ouchi, B., and Nishimori, H. 1994b, PASJ 46, 97.
- Mineshige, S. and Negoro, H. 1999, in *High energy processes in accreting black holes*, ASP Conf. Ser. 161, 113.
- Misner, C.W., Thorne, K.S., and Wheeler, J.A. 1973, *Gravitation*, Freeman, p.758.
- Miura, A. 1999, JGR 104/A1, 395.
- Moll, R. 2012, AA 548, A76
- Mollwo, L. 1983, SP 83, 305.
- Müller, D.A.N., Hansteen, V.H., and Peter, H. 2003, AA 411, 605.
- Müller, D.A.N., Peter, H., and Hansteen, V.H. 2004, AA 424, 289.
- Müller, D.A.N., de Groof, A., and Hansteen, V.H. 2005, AA 436, 1067.
- Mueller, M.W. and Arnett, W.D. 1976, ApJ 210, 676.
- Müller S.C. and Parisi, J. 2015, *Bottom-up self-organization in supramolecular soft matter: Principles and prototypical examples of recent advances*, Springer Series in Materials Science, Springer: New York.
- Murdzek, R. and Iftimie, O. 2008, Rom. J. Phys. 53(3-4), 601.
- Murray, C.D. and Dermott, S.F. 1999, *Solar system dynamics*, Cambridge Univ. Press, Cambridge.
- Musielak, Z.E. and Quarles, B. 2015, *The three-body problem*, arXiv:1508.02312v1, astro-ph.EP, 10 Aug 2015.
- Muto, T., Grady, C.A., Hashimoto, J., et al. 2012, ApJL 748, L22.
- Naab, T. and Ostriker, J.P. 2017, ARAA 55, 59.
- Nagy, D., Szirmai, G., and Domokos, P. 2008, arXiv:0801:4771v2.
- Nezlin, M.V., Chernikov, G.P., Rylov, A.Y., Titishov, K.B. 1996, Chaos: Interdisc. J. Nonlinear Science 6/3, 309.
- Nicolis, G. and Prigogine, I. 1977, *Self-organization in nonequilibrium systems*, Wiley: New York.
- Norris, J.P. and Matilsky, T.A. 1989, ApJ 346, 912.
- Nozakura, T. and Ikeuchi, S. 1988, APJ 333, 68.
- O'Donoghue, J., Moore, L., Stallard, T.S., Melin, H. 2016, Nature 536, Issue 7615, 190.
- Osborne, A.R. and Provenzale, A. 1989, Physica D 35, 357.
- Ostriker, J.P. and Peebles, P.J.E. 1973, ApJ 186, 467.
- Parett, A.L. 2007, IEEE Transact. Plasma Science 31/6, 1192.
- Parnell, C.E., DeForest, C.E., Hagenaar, H.J. et al. 2009, ApJ 698, 75.
- Patterson, C.W. 1987, Icarus 70, 319.
- Peale, S.J. 1976, ARAA 14, 215.

- Perez, J., Fuzfa, A., Carletti, T., Melot, L., and Guedezounme, L. 2014, *General Relativity and Gravitation* 46, id. 1753.
- Perinova, V., Luks, A., and Pintr, P. 2007, *Chaos, Solitons, and Fractals* 34(3), 669.
- Perlmutter, S. 1999, *ApJ* 517, 565.
- Peter, H., Gudiksen, B.V., and Nordlund, A.A. 2006, *ApJ* 638, 1086.
- Peter, H., Bingert, S., Kamio, S. et al. 2012, *AA* 537, A152.
- Petviashvili, V.I. 1980, *Soviet J. Exp. Theoret. Phys. Lett.* 32, 619.
- Planck Collaboration 2016, *AA* 594, A1, ..., A28.
- Pontius, D.H.Jr. and Hill, T.W. 2006, *JGR* 111, Issue A9, A09214.
- Pour-Imani H. and Kenefick, D. et al. 2016, *ApJL* 827, L2.
- Porco, C.C. and Hamilton, D.P. 2000, *Planetary Rings* in *Encyclopedia of the Solar System*, Academic Press.
- Procaccia, I. 1985, *Phys. Scripta* T9, 40.
- Prša, A., Harmanec, P., Torres, G., et al. 2016, *AJ* 152, 41.
- Pruessner, G. 2012, *Self-Organized Criticality. Theory, models and characterisation*, Cambridge: University Press.
- Purcell, C., Bullock, J.S., et al. 2011, *Nature* 477, 301.
- Read, P.L., Barstow, J., Charnay, B., et al. 2016, *Quat. J. Royal Meteorol. Soc.* 142, 703.
- Reese, E. and Beebe, R. 1977, *Planet. Space Sci.* 25, 890.
- Rego, J.A., Harvey, J.A.A., MacKinnon, A.L. and Gatdula, E. 2010, *Liquid Crystals* 37, 1.
- Remillard, R. and McClintock, J.E. 2006, *ARAA* 44, 49.
- Rempel, M. and Cheung, M.C.M. 2014, *ApJ* 785:90.
- Riess, A.G., Filippenko, A.V., Challis, P., Clocciatti, A. et al. 1998, *Astron. J.* 116, 1009.
- Ritu, H. 2016, *Sci. Rep.* 6:34095.
- Rohden, M., Sorge, A., Timme, M., Witthaut, D. 2012, *Phys. Rev. Lett.* 109/6, id.064101.
- Rosenberg, H. 1970, *AA* 9, 159.
- Rostami, M., Zeitlin, V., and Spiga, A. 2017, *Icarus* 297, 59.
- Ruge, J.P., Flock, M., Wolf, S., et al. 2016, *AA* 590, A17.
- Sano, T. and Stone, J.M. 2002a, *ApJ* 570, 314.
- Sano, T. and Stone, J.M. 2002b, *ApJ* 577, 534.
- Scardigli, F.A. 2007, *Foundations of Physics* 37, 1278.
- Scargle, J.D., Donoho, D.L., Crutchfield, J.P., et al. 1993, *ApJ* 411, L91.
- Schatten, K.H. 2007, *ApJS* 169, 137.
- Schatten, K.H. 2009, *SP* 255, 3.
- Scholkmann, F. 2017, *Prog. Physics* 13, 125.
- Schrijver, C.J. 2001, *SP* 198, 325.
- Schubart, J. 1968, *Astron. J.* 73, 99.
- Schuster, H.G. 1988, *Deterministic Chaos*, VCH Verlag: Weinheim.

- Sebillie, F., de La Mota, V., and Figuero, S. 2011, Phys. Rev. 84/5, id. 055801.
- Shakura, N.I. and Sunyaev, R.A. 1973, AA 24, 337.
- Sharma, A.S., Sitnov, M.I., Papadopoulos, K. 2001, JASTR 63/13, 1399.
- Shu, F. 2016, ARAA 54, 667.
- Simon, A.A., Wong, M.H., Rogers, J.H., et al. 2014, ApJL 797, L31.
- Simon, J.B., Bai, X.N., Flaherty, K.M. et al. 2017, arXiv 1711.04770.
- Sinclair, A.T. 1969, MNRAS 142 142, 289.
- Sinclair, A.T. 1972, MNRAS 160 142, 169.
- Smith, K.L., Mushotzky, R.F., Boyd, P.T., and Wagoner, R.V. 2017, ApJL (submitted).
- Sneppen K. and Newman M.E.J. 1997, Physica D Nonlinear Phenom., 110, 209.
- Springel, V., White, S.D.M., Jenkins, A. et al. 2005, Nature 435, 629.
- Stark, D.P. 2016, ARAA 54, 761.
- Stein, R.F., Lagerfjerd, A., Nordlund, A. and Georgobiani, D. 2011, SP 268, 271.
- Stein, R.F. 2012, Living Review Solar Physics 9:4.
- Stephens, G.L., Li, J.L., Wild, M., Clayson, C.A., et al. 2012, Nature Geoscience 5, 691.
- Strogatz, S.H. 1994, *Nonlinear dynamics and chaos, with applications to physics, biology, chemistry, and engineering*, Westview, Perseus Books Publishing.
- Surdin, M. 1980, Il Nouovo Cimento C 3(6). 626.
- Szydlowski, M. and Stachowski, A. 2016, Phys. Rev. D 94/4, id. 043521.
- Takamaru, H. and Sato, T. 1997, Phys. Plasmas 4/8, 2845.
- Takenouchi, T. 1962, Ann. Tokyo Obs. 7, 191.
- Tanaka, H.A., Lichtenberg, A.J., Oishi, S.I. 1997, Phys. Rev. Lett. 78/11, 2104.
- Tetreault, D. 1992a, JGR 97/A6, 8541.
- Tetreault, D. 1992b, JGR 97/A8, 8531.
- Tobias, S.M., Weiss, N.O., and Kirk, V. 1995, MNRAS 273, 1150.
- Tokar, R.L., Johnson, R.E., Hill, T.W., et al. 2006, Science 311, Issue 5766, 1409.
- Toomre, A. 1977, ARAA 15, 437.
- Toomre, A. 1981, in *The Structure and Evolution of Normal Galaxies*, (eds. S.M. Fall and D. Lynden-Bell), Cambridge University Press: Cambridge.
- Tortosa-Andreu, A. and Moreno-Insertis, F. 2009, A&A 507, 949.
- Trakhtengerts, V. Yu. 1968, Geomagnetny and Aeronomie 8/2, 776.
- Trenberth, K.E., Fasullo, J.T., and Kiehl, J. 2009, Bull. American Meteorological Society 90, 311.
- Trimble, V. 1987, ARAA 25, 425.
- Trottet, G., Kerdraon, A., Benz, A.O. and Treumann, R. 1981, AA 93, 129.
- Trugenberger, C.A. 2015, Phys. Rev. D 92/8, id. 084014.
- Uzdensky, D.A. 2007a, ApJ 671, 2139.

- Uzdensky, D.A. 2007b, Phys. Rev. Lett. 99/26, id. 261101.
- Valdivia, J.A., Klimas, A., Vassiliadis, D., Uritsky, V., and Takalo, J., 2003, SSRv 107, 515.
- van der Klis, M. 2006, Adv.Space Res. 38, 2675.
- van der Marel, N., van Dishoeck, E.F., Bruderer, S., et al. 2013, Science 340, 1199.
- Van Kooten, S.J., and Cranmer, S.R. 2017, arXiv:1710.04738.
- Vazifeh, M.M. and Franz, M. 2013, Phys. Rev. Lett. 111/20, ie. 206802.
- Vlahos, L. and Georgoulis, M.K. 2004, ApJ 603, L61.
- Vogelsberger, M., Genel, S., Springel, V., et al. 2014, MNRAS, arXiv:1405.2921v2 .
- Voges, W., Atmanspacher, H., and Scheingraber, H. 1987, ApJ 320, 794.
- Volterra, V. 1931, *Variations and fluctuations of the number of individuals in animal species living together*, in Chapman, R.N., Animal Ecology, McGraw-Hill.
- Wagoner, R.V. 2008, New Astron. Rev. 51, 828.
- Wang, Z., Szolnoki, A., and Perc, M. 2014, New J. Phys. 16/3, id. 033041.
- Wardle, M. 1999, MNRAS 307, 849.
- Wardle, M. and Ng, C. 1999, MNRAS 303, 239.
- Wardle, M. 2007, ApSS 311, 35.
- Warnecke, J., Rheinhardt, M., Tuomisto, S. 2017, eprint arXiv:1601.03730.
- Warszawski, L. and Melatos, A. 2011, MNRAS 415, 1611.
- Warszawski, L., Melatos, A., and Berloff, N.G. 2012, Phys. Rev. B 85/10, id. 104503.
- Watts, D.J. and Strogatz, S.H. 1998, Nature 393, 440.
- Wells, D.R. 1989a, IEEE Transactions on Plasma Science 14(6), 865.
- Wells, D.R. 1989b, IEEE Transactions on Plasma Science 17(2), 270.
- Wells, D.R. 1990, IEEE Transactions on Plasma Science 19(1), 73.
- Wheatland, M.S. 2008, ApJ 679, 1621.
- Wild, M. 2017, AIP Conf. Proc. 1810, 0200004-1, AIP Publishing.
- Wild, M., Folini, D., Hakuba, M.Z., et al. 2015, *Climate Dynamics* 44, 3393.
- Winfree, A.T. 1972, Science 175, 634.
- Winfree, A.T. 1973, Science 185, 937.
- Winglee, R.M. and Dulk, G.A. 1986, ApJ 307, 808.
- Winn, J.N. and Fabrycky D.C. 2015, ARAA 53, 409.
- Wisdom, J. 1980, ApJ 85/8, 1122.
- Woltjer, L. 1959, ApJ 130, 30 and 405.
- Woltjer, L. 1965, in *Galactic Structures*, (eds. A. Blaauw and Schmidt, M.), University of Chicago Press, p.531.
- Yamada, M. 2007, Phys.Plasmas 14/5, 058102.
- Yamada, M., Kulsrud, R., and Ji, H.T. 2010, Rev.Mod.Phys. 82, 603.

- Yoshida, Z., Saitoh, H., Morikawa, J., Yano, Y., Watanabe, S., and Ogawa, Y. 2010, *Phys. Rev. Lett.* 104/23, id. 235004.
- Young, K. and Scargle, J.D. 1996, *ApJ* 468, 617.
- Zaikin, A.N., and Zhabotinsky, A.M. 1970, *Nature* 225, 535.
- Zaitsev, V.V. 1971, *SP* 20, 95.
- Zaitsev, V.V. and Stepanov, A.V. 1975, *AA* 45, 135.
- Zeiger, H.J. and Kelley, P.L. 1991, *Lasers*, in *The Encyclopedia of Physics*, 2nd Edition (ed. Lerner, R., and Trigg, G.), VCH Publishers.
- Zhang, Q., Cheng, L., and Boutaba, R. 2010, *J. Internet Services and Applications* 1(1):7.
- Zheleznyakov, V.V. and Zlotnik, E.Ya. 1975a, *SP* 44, 447.
- Zheleznyakov, V.V. and Zlotnik, E.Ya. 1975b, *SP* 44, 461.
- Zweibel, E.G. and Yamada, M. 2009, *ARAA* 47, 291-332.

Table 1. Self-organization processes in astrophysics: The symbols in the last column indicate the following system characteristics: LC= nonlinear systems with limit cycle(s), I = instabilities, R = resonances, E = entropy, S = regular spatial pattern, T = regular temporal pattern, ? = conjectural. The stellar QPOs include also accretion disks and “coronas” of compact objects and supermassive black holes.

Observed Phenomenon	Driver Mechanism	Feedback Mechanism	Characteristics
Planetary spacing	gravity	harmonic orbit resonances	R, S, T
Saturn rings and moons	gravity	harmonic orbit resonances	R, S, T
Protoplanetary disks	rotation	Hall-shear instability	I, S
Jupiter’s red spot	temperature gradient	inverse MHD turbulent cascade	I, S
Saturn’s hexagon	circumpolar jet-stream	diocotron instability	I, S
Planetary entropy	solar radiation	planetary infrared emission	E
Solar photospheric granulation	temperature gradient	Rayleigh-Bénard instability	I, S
Solar magnetic fields	solar dynamo, rotation	bouyancy, kink instability	I(?), S
Solar magnetic Hale cycle	differential rotation	twisted magnetic field relaxation	LC, I(?), S, T
Solar flare loops	chromospheric evaporation	coronal condensation	I, LC[?],T(?)
Solar radio pulsations	nonthermal particles	loss-cone instability	LC, I[?], T
Solar zebra radio bursts	nonthermal particles	double plasma resonance	R, S, IT[?]
	nonthermal particles	Langmuir-whistler coalescence	R, S, IT[?]
Star formation	gravity	radiation and recombination	I, S, T
Stellar quasi-periodic oscillations	rotation	magneto-rotational instability	LC, I(?),T
Pulsar superfluid unpinning	rotation	Magnus force	I(?), S[?]
Galaxy formation	gravity, rotation	density waves, reaction-diffusion	S, I(?)
Cosmology	Big Bang expansion	inflationary $\Lambda$ CDM model	I(?),LC(?),S[?],T[?]

Table 2. Non-astrophysical self-organization processes.

Field	Phenomenon	Reference
Ionosphere	Stimulation of electromagnetic emission	Leyser (2001)
	Internal gravity waves	Aburjania et al. (2013)
	Acoustic gravity waves	Kaladze et al. (2008)
Magnetosphere	Substorm dynamics	Sharma et al. (2001)
	Substorm current sheet model	Valdivia et al. (2003)
	Magnetospheric vortex formation	Yoshida et al. (2010)
	2D MHD transverse Kelvin-Helmholtz instability	Miura (1999)
	Turbulent relaxation of magnetic fields	Tetreault (1992a,b)
Plasma physics	Superconducting ring magnet vortex	Yoshida et al. 2010
	Magnetic reconnection in laboratory	Yamada et al. (2010)
	Magnetic reconnection in laboratory	Zweibel and Yamada (2009)
Physics	Coupled pendulums	Tanaka et al. (1997)
	Spontaneous magnetization	Boesiger et al. (1978)
	Laser	Zeiger and Kelley (1991)
	Superconductivity	Vazifeh and Franz (2013)
	Bose-Einstein condensation	Nagy et al. (2008)
Chemistry	Molecular self-assembly	Lehn (2002)
	Supramolecular soft matter	Müller and Parisi (2015)
	Reaction-diffusion systems	Kolmogorov et al. (1937)
	Oscillating reactions	Bray, W.C. (1921)
	Oscillating catalytic reaction	Cox et al. (1985)
	Liquid crystals	Rego e al. (2010)
	Self-assembled monolayers	Love et al. (2005)
	Langmuir-Blodgett films	Ritu (2016)
	Growth of SiGe nanostructures	Aqua et al. (2013)
	Biology	Biological systems
Pattern formation in slime molds and bacteria		Camazine et al. (2001)
Feeding aggregations of bark beetles		Camazine et al. (2001)
Synchronized flashing among fireflies		Camazine et al. (2001)
Fish schooling		Camazine et al. (2001)
Nectar source selection by honey bees		Camazine et al. (2001)
Trail formation in ants		Camazine et al. (2001)
Swarm raids of army ants		Camazine et al. (2001)
Colony thermoregulation in honey bees		Camazine et al. (2001)
Comb patterns in honey bee colonies		Camazine et al. (2001)
Wall building by ants		Camazine et al. (2001)
Termite mound building		Camazine et al. (2001)

Table 2—Continued

Field	Phenomenon	Reference
Social science	Construction algorithms in wasps	Camazine et al. (2001)
	Dominance hierarchies in paper wasps	Camazine et al. (2001)
	Social evolutionay systems	Leydesdorff (1993)
	Learning algorithms	Geach (2012)
Computer science	Coevolution in interdependent networks	Wang et al. (2014)
	Cybernetics	Ashby (1947)
	Cellular automata	Gacs (2000)
	Random graphs	Brooks (2009)
	Multi-agent systems	Kernbach (2008)
	Small-world networks	Watts and Strogatz (1998)
	Power grid network simulations	Rohden et al. (2012)
	Self-organizing maps	Kohonen (1989)
	Cloud computing systems	Zhang et al. (2010)
	Moore’s Law	Georgiev et al. (2016)

Table 3. Observed orbital periods and distances of the planets from the Sun, and the nearest predicted harmonic orbit resonances ( $H1 : H2$ ) or order of resonances ( $l, k$ ), orbital periods  $T[yr]$ , observed and best-fit semi-major axes  $a_{obs}$  and  $a_{harm}$ , and ratios  $a_{harm}/a_{obs}$ .

Planet	number	l	k	H1	H2	Period [yr]	$a_{obs}$ [AU]	$a_{harm}$ [AU]	Ratio $a_{harm}/a_{obs}$
Mercury	1	3	2	5	2	0.241	0.39	0.391	1.002
Venus	2	2	3	5	3	0.615	0.72	0.711	0.988
Earth	3	1	1	2	1	1.000	1.00	0.958	0.957
Mars	4	3	2	5	2	1.881	1.52	1.504	0.989
Ceres	5	3	2	5	2	4.601	2.77	2.823	1.019
Jupiter	6	3	2	5	2	11.862	5.20	5.179	0.996
Saturn	7	2	1	3	1	29.457	9.54	9.225	0.967
Uranus	8	1	1	2	1	84.018	19.19	18.943	0.987
Neptune	9	1	2	3	2	164.78	30.07	30.129	1.002
Pluto	10					284.40	39.48	.....	.....
Mean									$0.99 \pm 0.02$

Table 4. Characteristics of randomness, self-organization, and self-organized criticality systems or processes.

Parameter	Randomness process	Self-organizing process	Self-organized criticality process
Dynamics :	events	limit cycle	avalanches
Temporal structure :	intermittent	quasi-periodic	intermittent, scale-free
Temporal size distribution :	exponential	quantized	power law
Spatial structure :	random	ordered	fractal, scale-free
Spatial size distribution :	Gaussian	quantized	power law
Entropy evolution :	increasing	decreasing	invariant
Physical condition :	independency	positive feedback	critical threshold

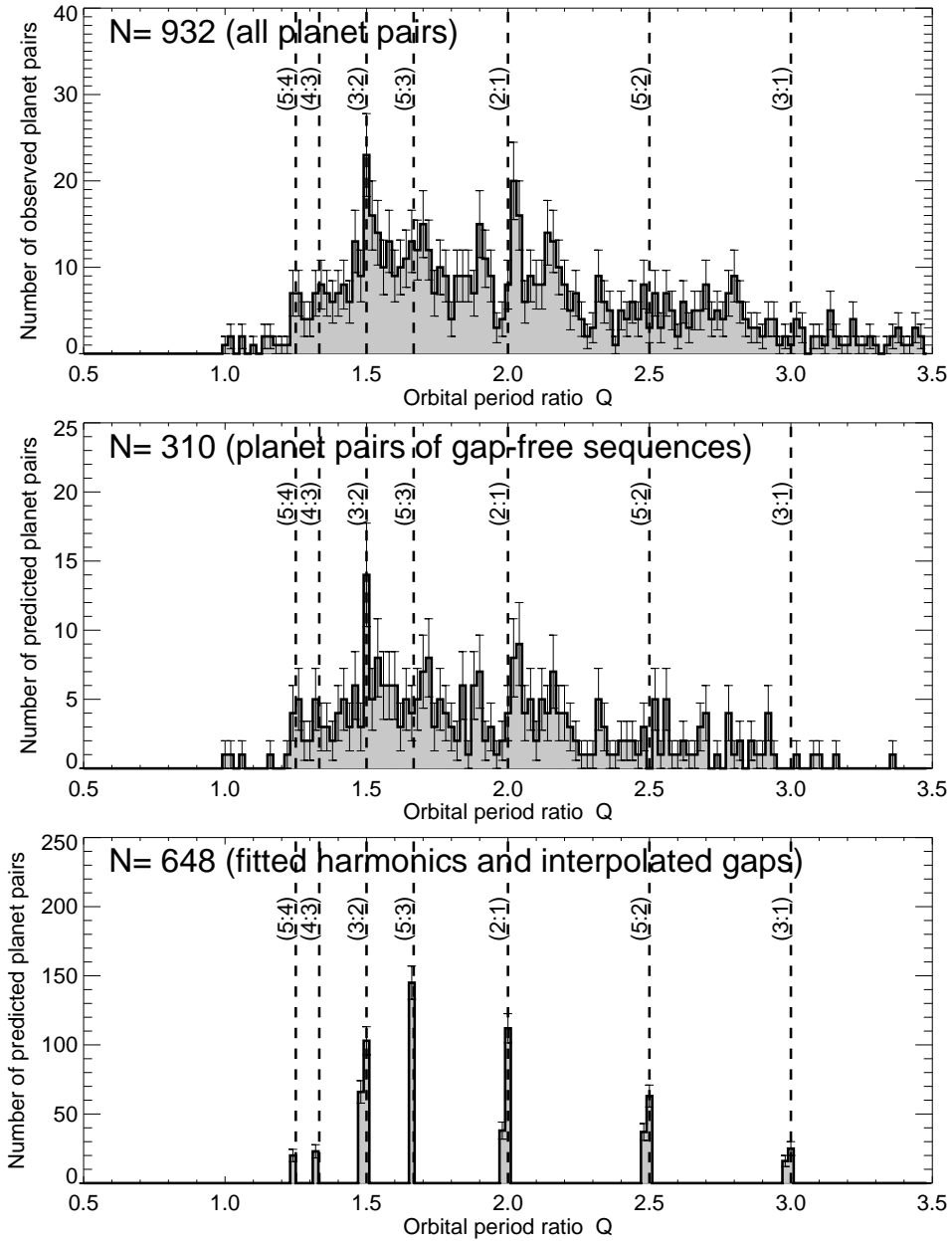


Fig. 1.— *Top*: The distribution of orbital period ratios in 932 pairs of exo-planets observed with the KEPLER mission. *Middle*: The distribution of 310 orbital period ratios in gap-free sequences of exo-planets. *Bottom*: Quantized distribution of best-fit harmonic period ratios, including interpolation in “gappy sequences” [adapted from Aschwanden and Scholkmann 2018].

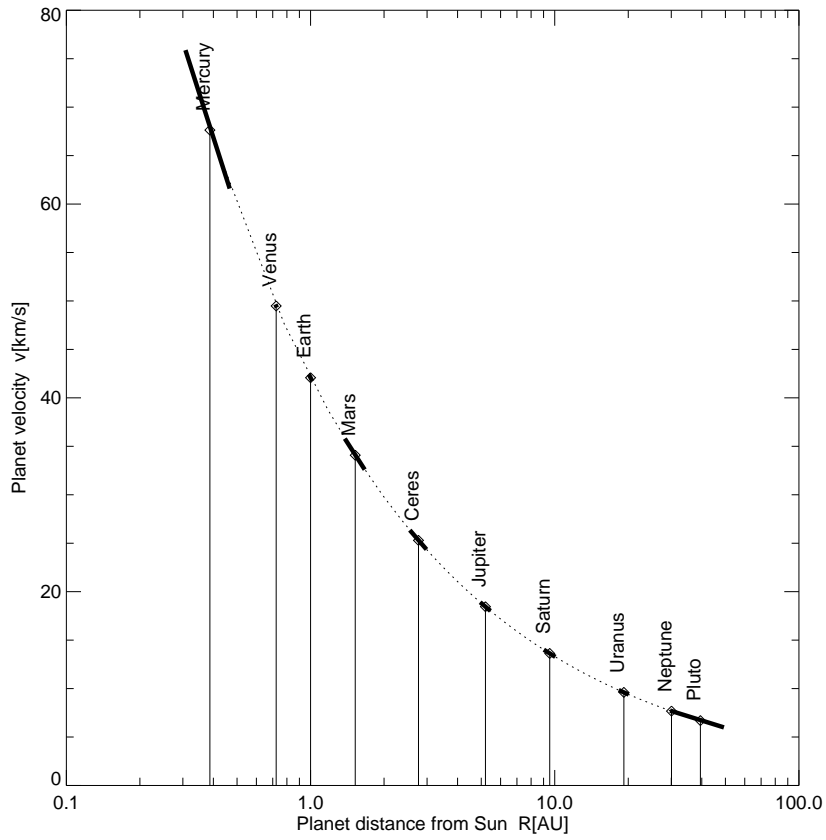


Fig. 2.— Phase-space diagram of planet distances from Sun,  $r$ , and planet velocity,  $v$ , for Keplerian orbits. The Keplerian orbit is marked with a dotted curve, the planet positions in phase space with diamonds, and the planet motions in phase space with thick curve segments. Note that Mercury and Pluto, the two planets with the largest orbit eccentricity, have the largest trajectories in phase space. The mean planet locations (diamonds) in phase space represent attractors of a nonlinear system with limit cycles.



Fig. 3.— First radio occultation observation of Saturn’s rings on 2005 May 3 with the Cassini spacecraft, using the radio bands of 0.94, 3.6, 13 cm. The spatial resolution is  $\approx 10$  km. The largest gap is the Cassini division, and the last outer (spatially resolved) gap is the Encke division [Credit: Cassini-Huygens mission, NASA].

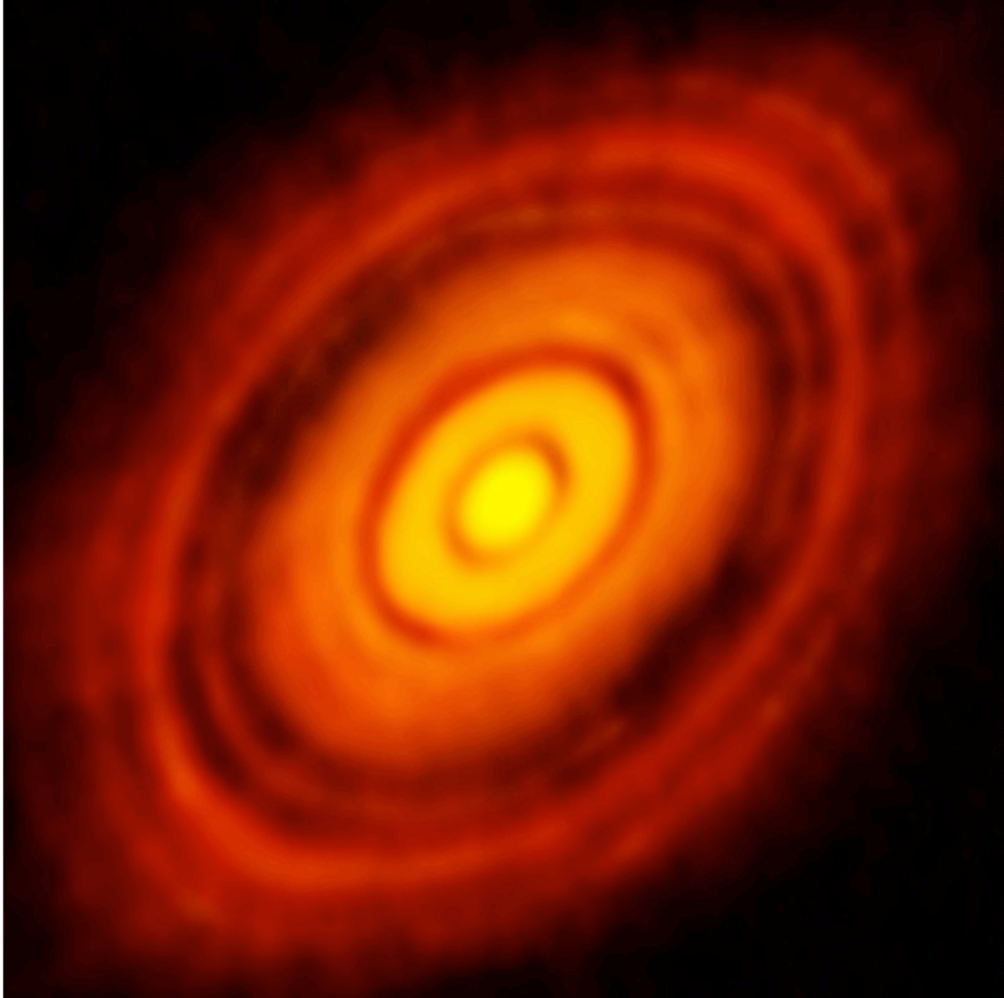


Fig. 4.— Thermal emission from millimeter-sized dust grains settled in the midplane of the HL Tauri disk, featuring a series of axisymmetric rings and gaps [ALMA Partnership 2015].

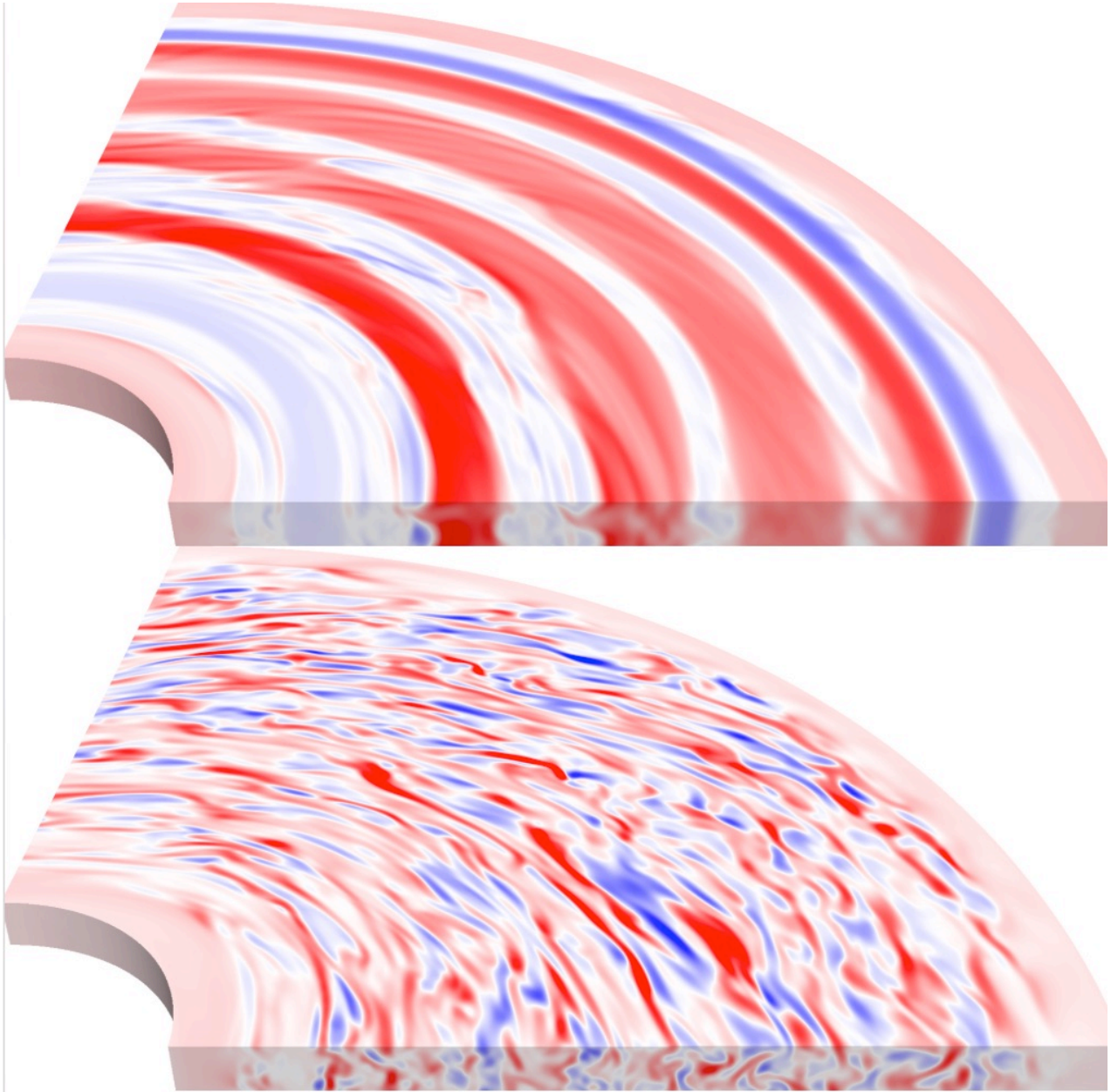


Fig. 5.— Axial magnetic field in two non-stratified simulations of protoplanetary disks. *Bottom*: MRI-driven turbulence in ideal MHD; *Top*: Ordered phase displaying axisymmetric rings of magnetic flux in Hall-MHD [Béthune et al. 2016].

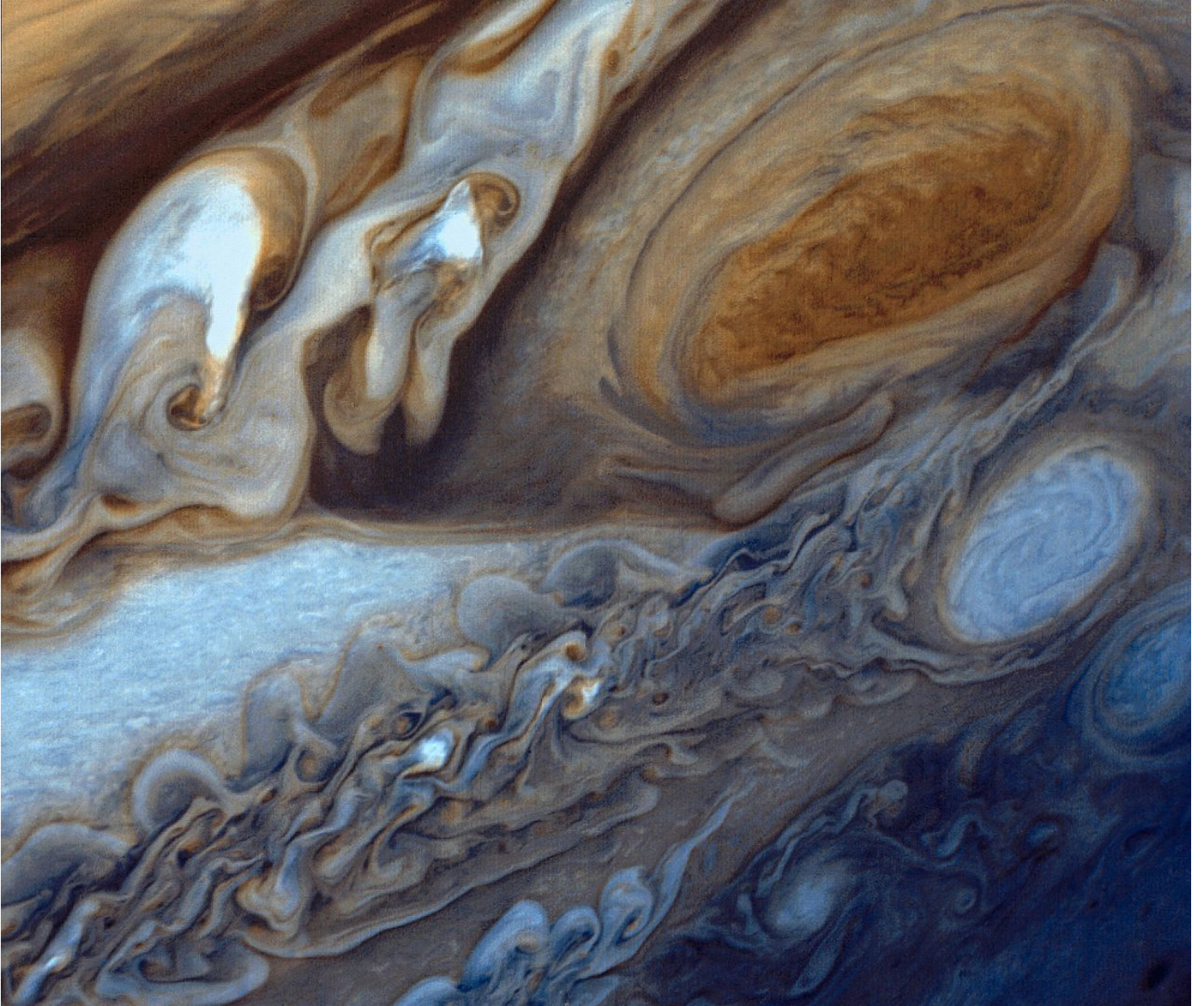
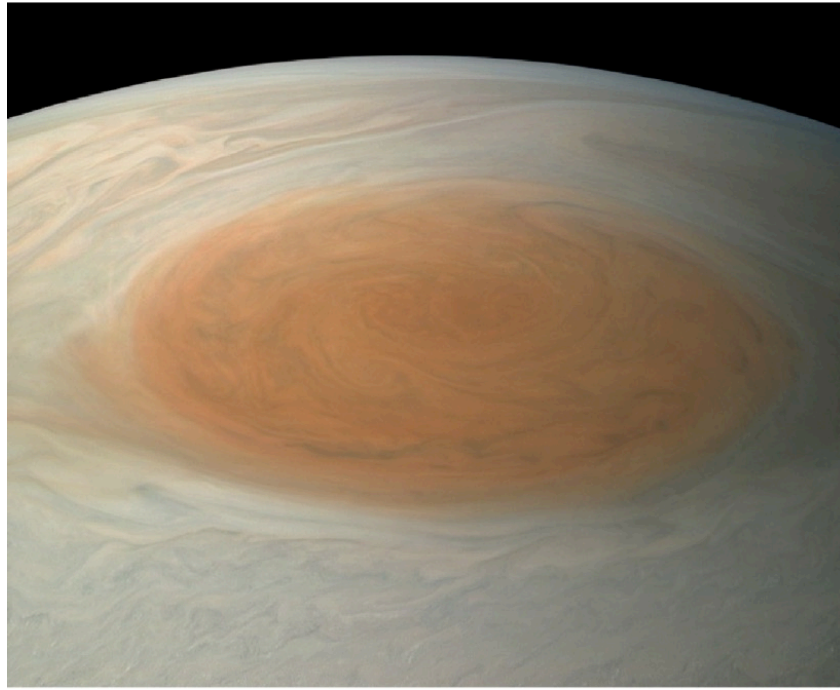


Fig. 6.— False-color image of the Great Red Spot of Jupiter, observed with Voyager [credit: NASA, Caltech/JPL - [http://www.jpl.nasa.gov/releases/2002/release\\_2002\\_166.html](http://www.jpl.nasa.gov/releases/2002/release_2002_166.html)].



Velocity field of the Great Red Spot and its surroundings

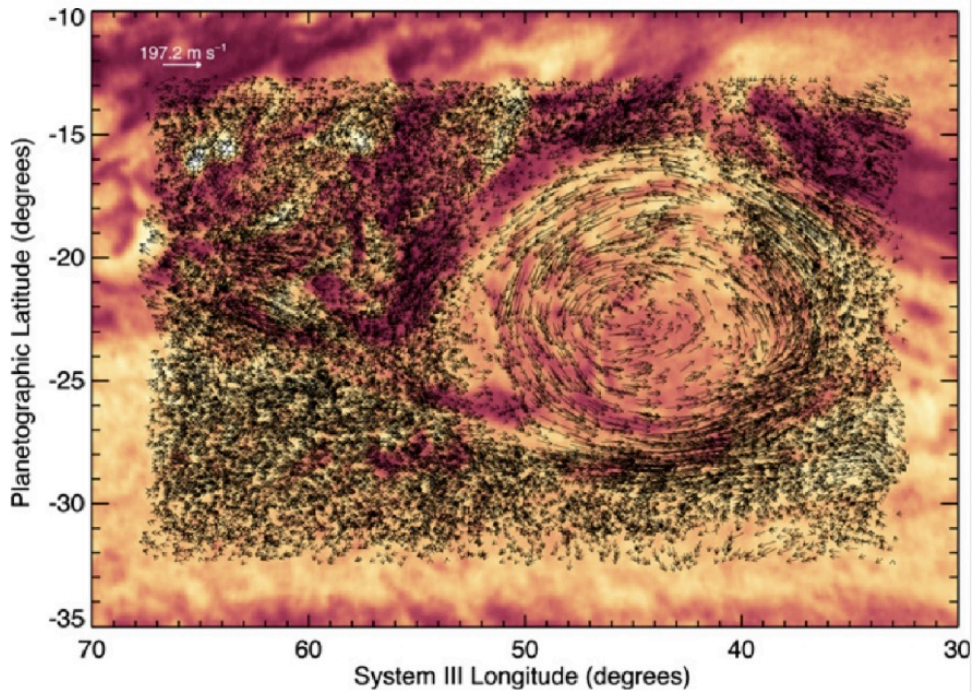


Fig. 7.— *Top*: Great Red Spot rendered in true colors recently obtained by the Juno spacecraft in 2017 [Image credit: NASA/JPL-Caltech/Space Science Institute, SwRI/MSSS, Björn Jonsson]. *Right*: Visualization of the velocity field [Simon et al. 2014].

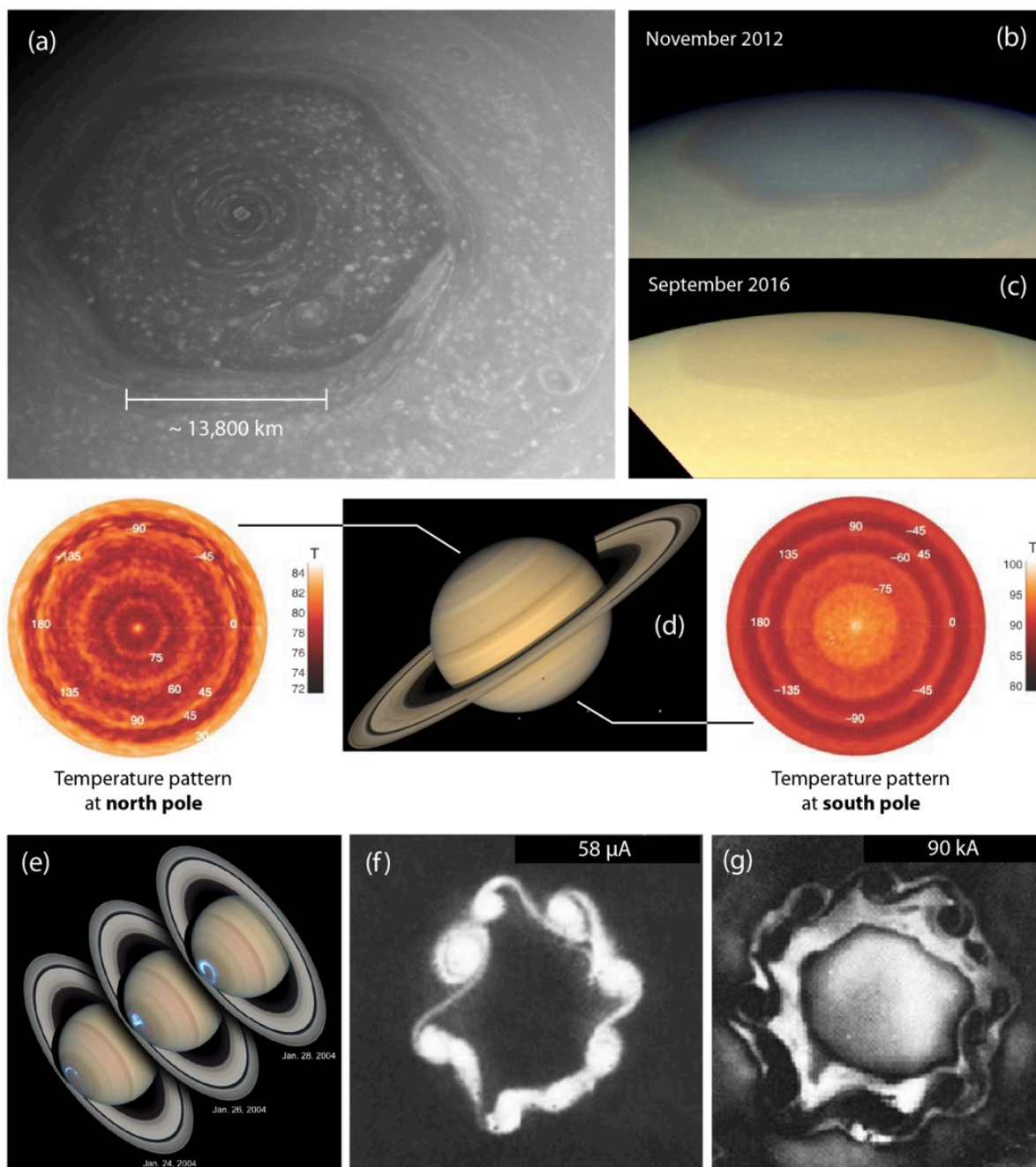


Fig. 8.— (a) Picture of Saturn’s hexagon at the north pole (view:  $53^\circ$  above the ringplane). Image taken by the Cassini spacecraft, 2013. [Image credit: NASA/JPL-Caltech/Space Science Institute]. (b) and (c): Images of the hexagon taken by Cassini in 2012 and 2016. [Image credit: NASA/JPL-Caltech/Space Science Institute.] (d) Temperature distribution at the north and south plane (in the troposphere at 100 mbar) according to Fletcher et al. (2008). (e) Aurora on Saturn [Image credit: NASA]. (f) and (g) show discharge structures of electron beam interactions with a fluorescence screen at  $58 \mu\text{A}$  (f) or with a steel witness plate at 90 kA (g) (Parett et al. 2007).

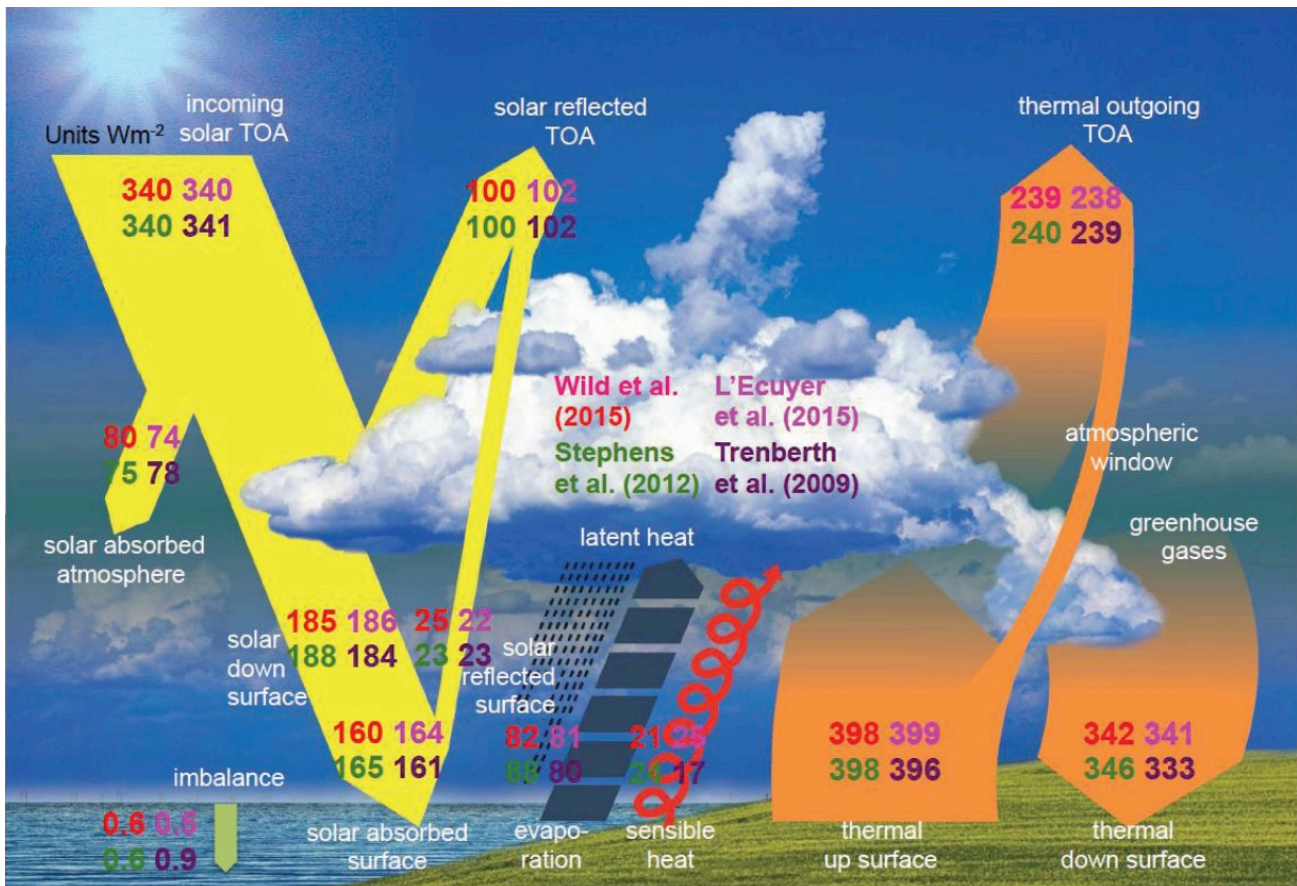


Fig. 9.— Comparison of different recent global annual mean energy balance estimates for present day conditions as published by Wild et al. (2015) (upper left red values), L'Ecuyer et al. (2012) (upper right pink values), Stephens et al. (2012) (lower left green values), and Trenberth et al. (2009) (lower right purple values). Units in  $\text{W m}^{-2}$  [Credit: Figure adapted from Wild 2017].

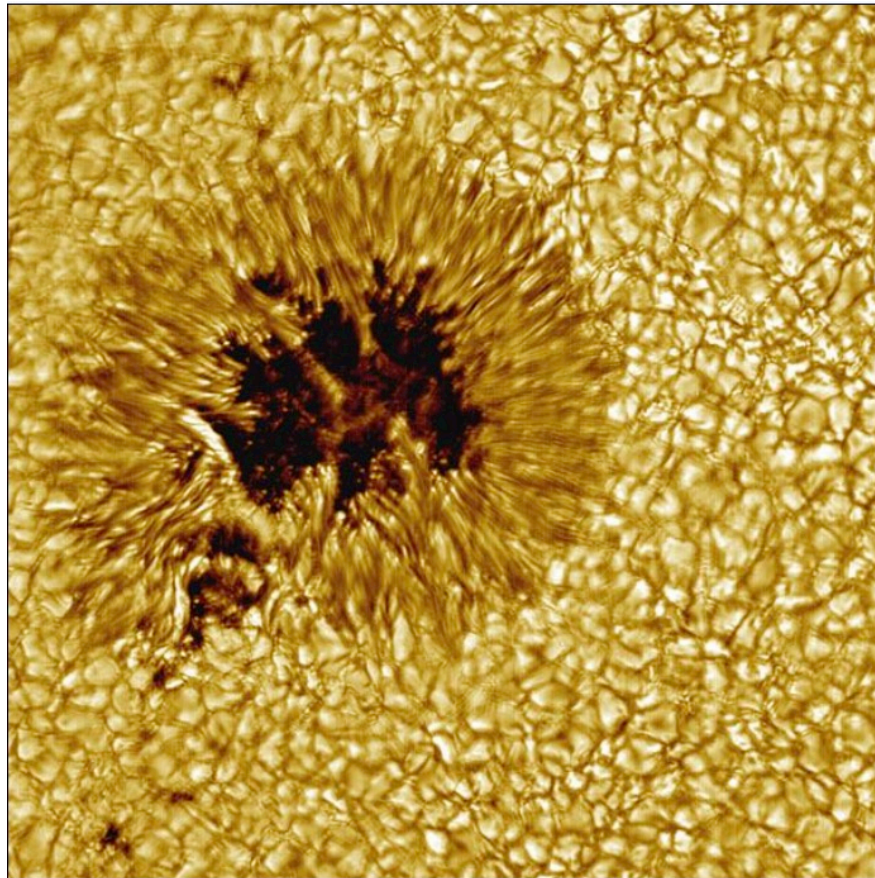


Fig. 10.— Closeup of photospheric granulation pattern and a sunspot near the center of the Sun. Note that the average size of granules has a typical size of  $w \approx 1500$  km [credit: NSO, NOAO, <https://apod.nasa.gov/apod/ap051106.html>].

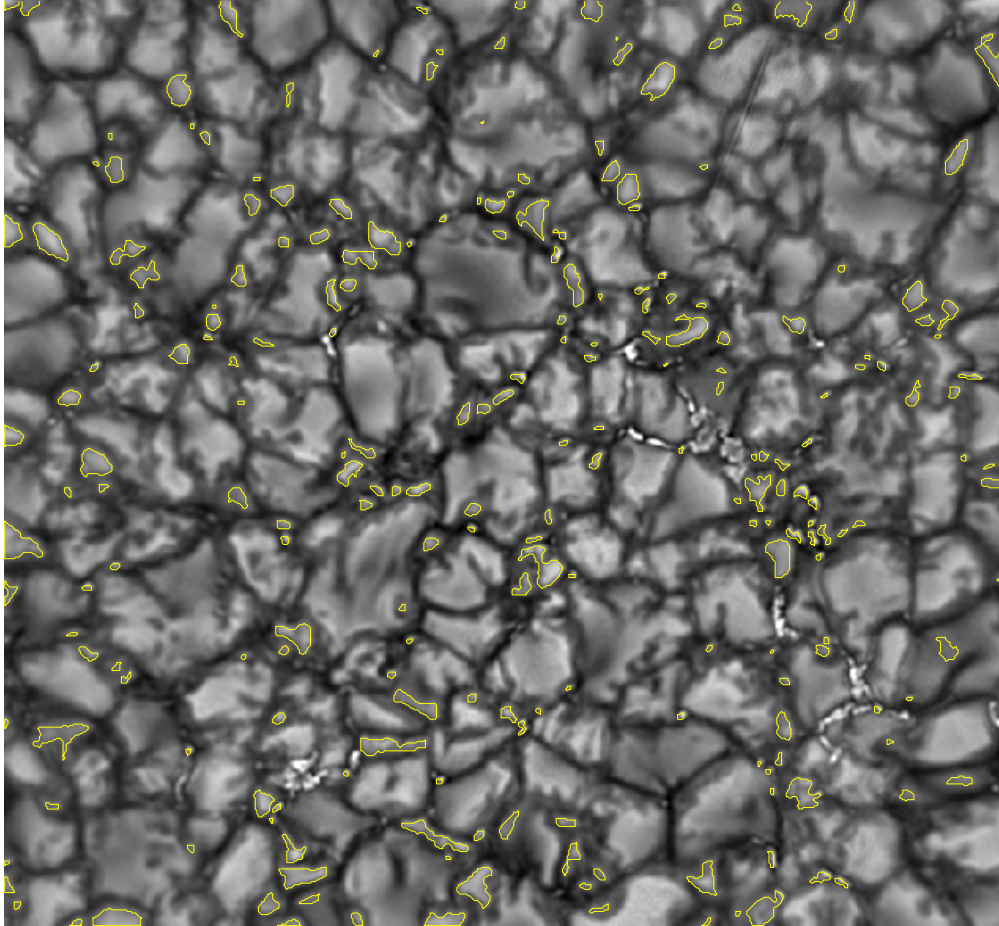


Fig. 11.— A TiO image of the solar surface is shown, containing normal granules and mini-granules in a Quiet Sun region, observed with the New Solar Telescope (NST). Mini-granules are outlined with yellow contours, which show granular-like features of sizes below 600 km located in dark intergranular lanes. Note that the mini-granules do not coincide with magnetic bright points [Abramenko et al. 2012].

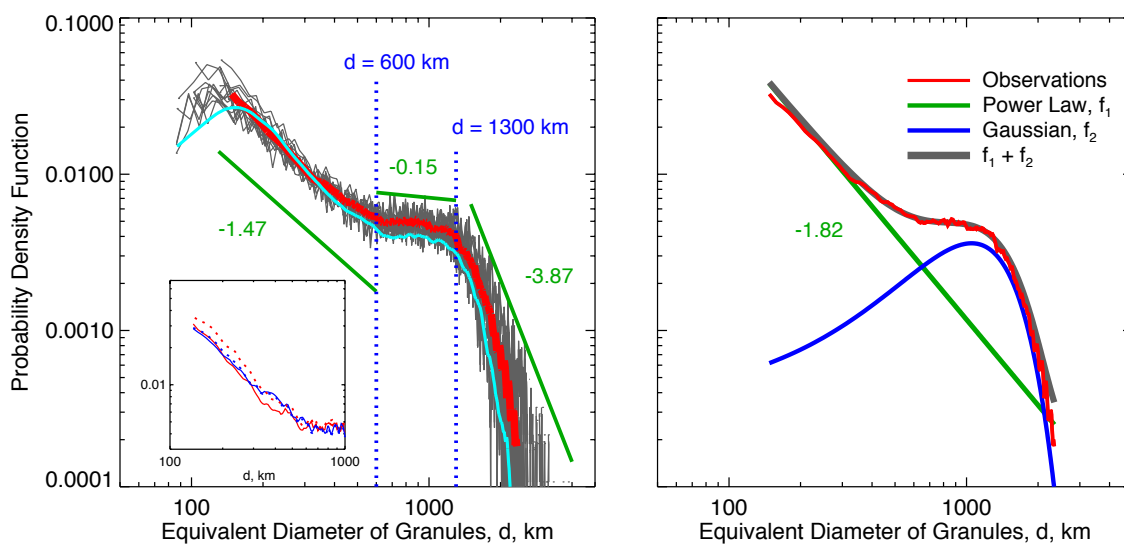


Fig. 12.— The probability density function of the equivalent diameter of granules (in units of km) is shown, observed in Quiet Sun regions with the New Solar Telescope (NST). The regular granules have a size of  $w \approx 500 - 2000$  km, while the range of  $w \approx 100 - 500$  km exhibits the new phenomenon of “mini-granules” [Abramenko et al. 2012].

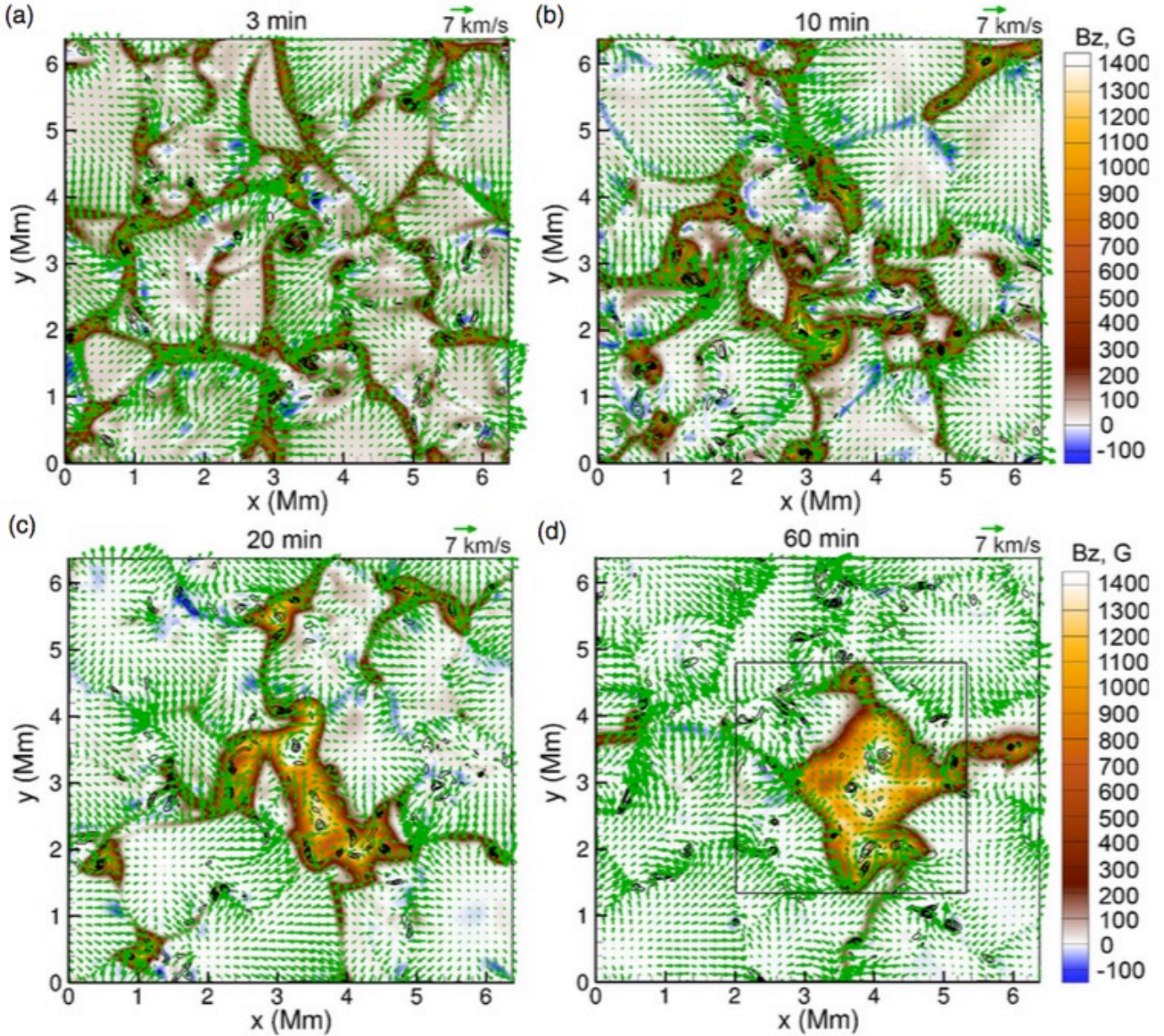


Fig. 13.— Four snapshots of the simulated formation of magnetic field structures (pores and sunspots), showing the surface distribution of the vertical magnetic field (color background), the horizontal flows (arrows), and the vorticity magnitude (black contour lines), at 4 times (3, 10, 20, 60 min) from the moment of initiation of a uniform magnetic field ( $B_z = 100$  G) [Kitiashvili et al. 2010].

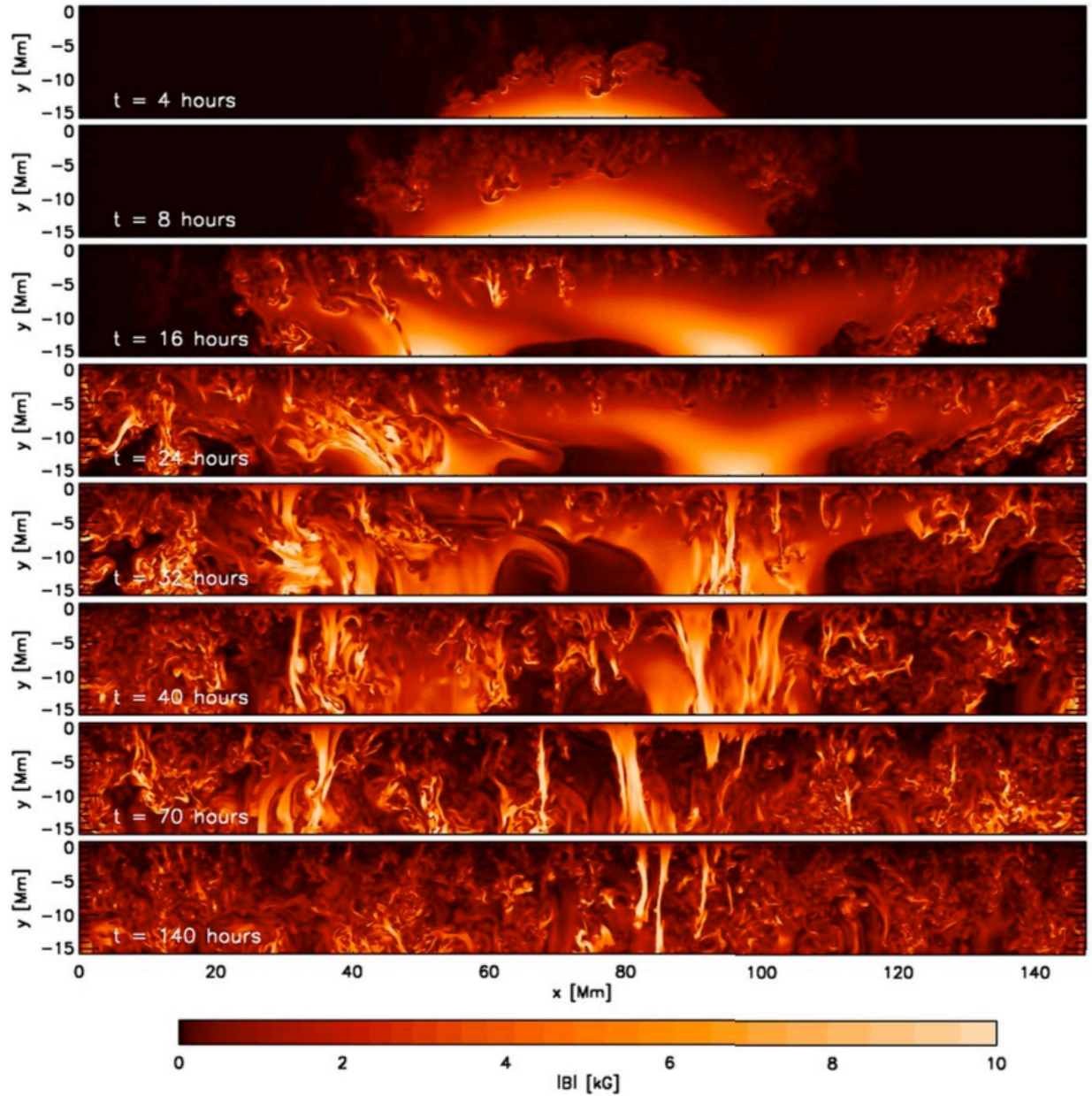


Fig. 14.— Time evolution of the magnetic field strength  $|B|$  during magnetic flux emergence on a vertical cut through the center of the domain along the  $x$ -axis. The first two snapshots show the subsurface field evolution prior to the appearance of flux in the photosphere, the remaining six snapshots correspond to the photospheric magnetograms [Rempel and Cheung 2014].

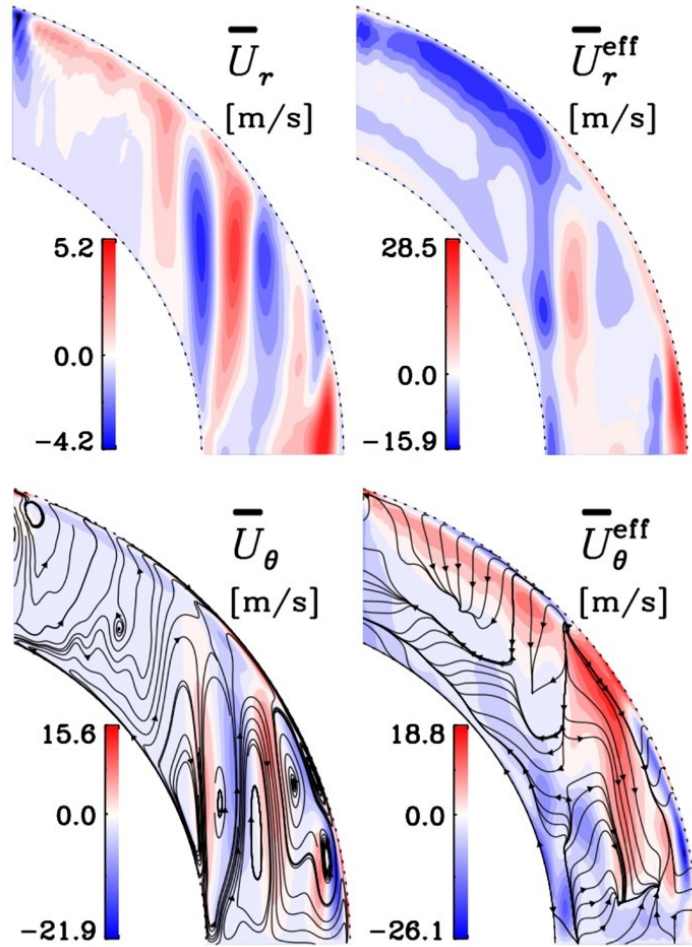


Fig. 15.— The solar dynamo action obtained from a 3-D MHD simulation is depicted in the convection zone, showing the time-averaged radial and effective radial flow (top panels), and the latitudinal and effective latitudinal flow [Warnecke et al. 2017].

### DAILY SUNSPOT AREA AVERAGED OVER INDIVIDUAL SOLAR ROTATIONS

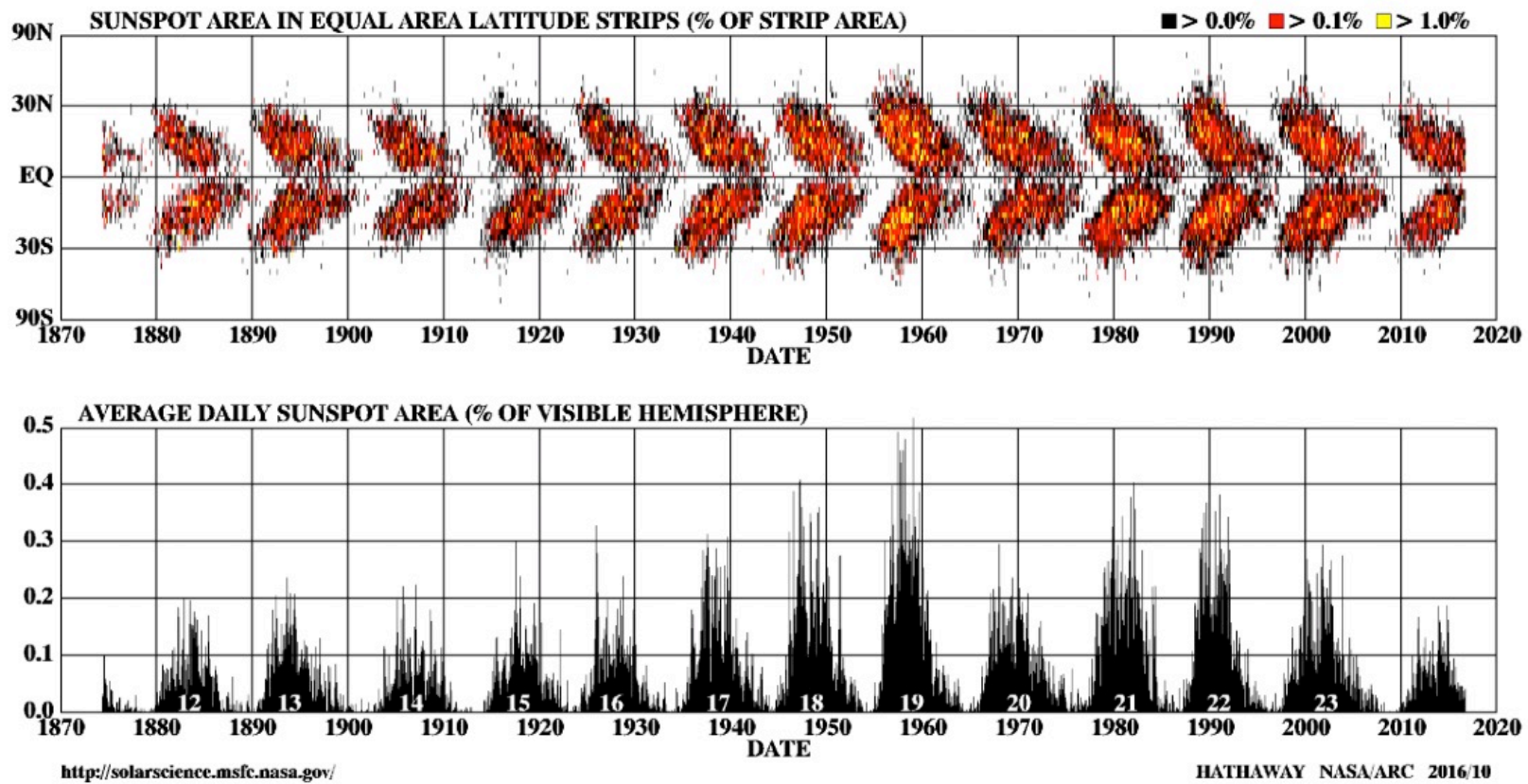


Fig. 16.— The variation of the sunspot number from 1870 to 2020, showing the 11-year periodicity in the average daily sunspot area (bottom panel) and in the latitude distribution (butterfly diagram in top panel). [Credit: <http://solarscience.msfc.nasa.gov/>, David Hathaway, NASA/ARC].

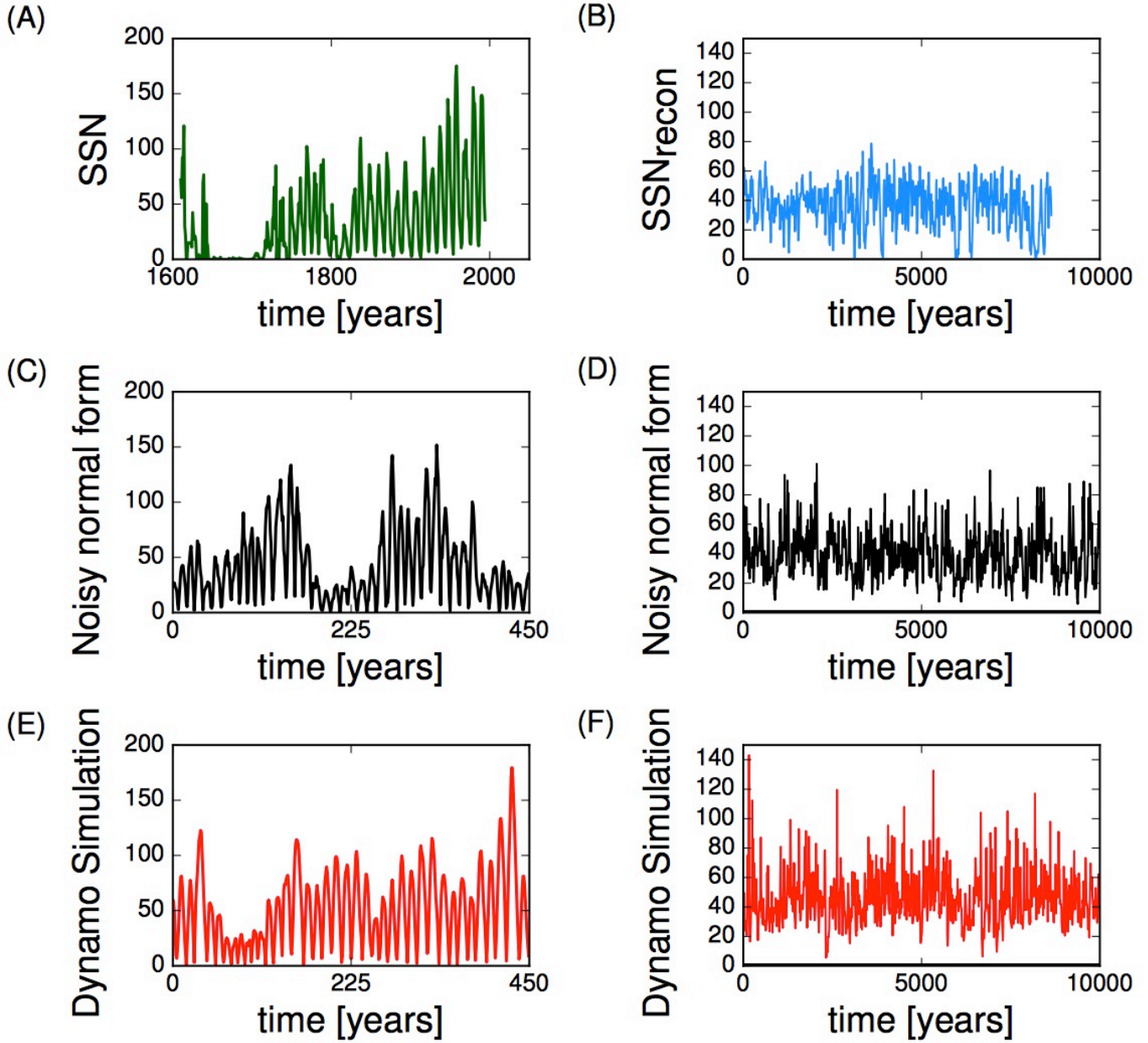


Fig. 17.— (A) Time series of the observed sunspot numbers (SSN); (B) Sunspot number reconstructed from cosmogenic isotopes ( $SSN_{recon}$ ); (C,D) Monte-Carlo simulations of a weakly nonlinear, noisy limit cycle (Hopf bifurcation normal-form model); (E,F) Results from Babcock-Leighton dynamo model with fluctuating sources [Cameron and Schüssler 2017].

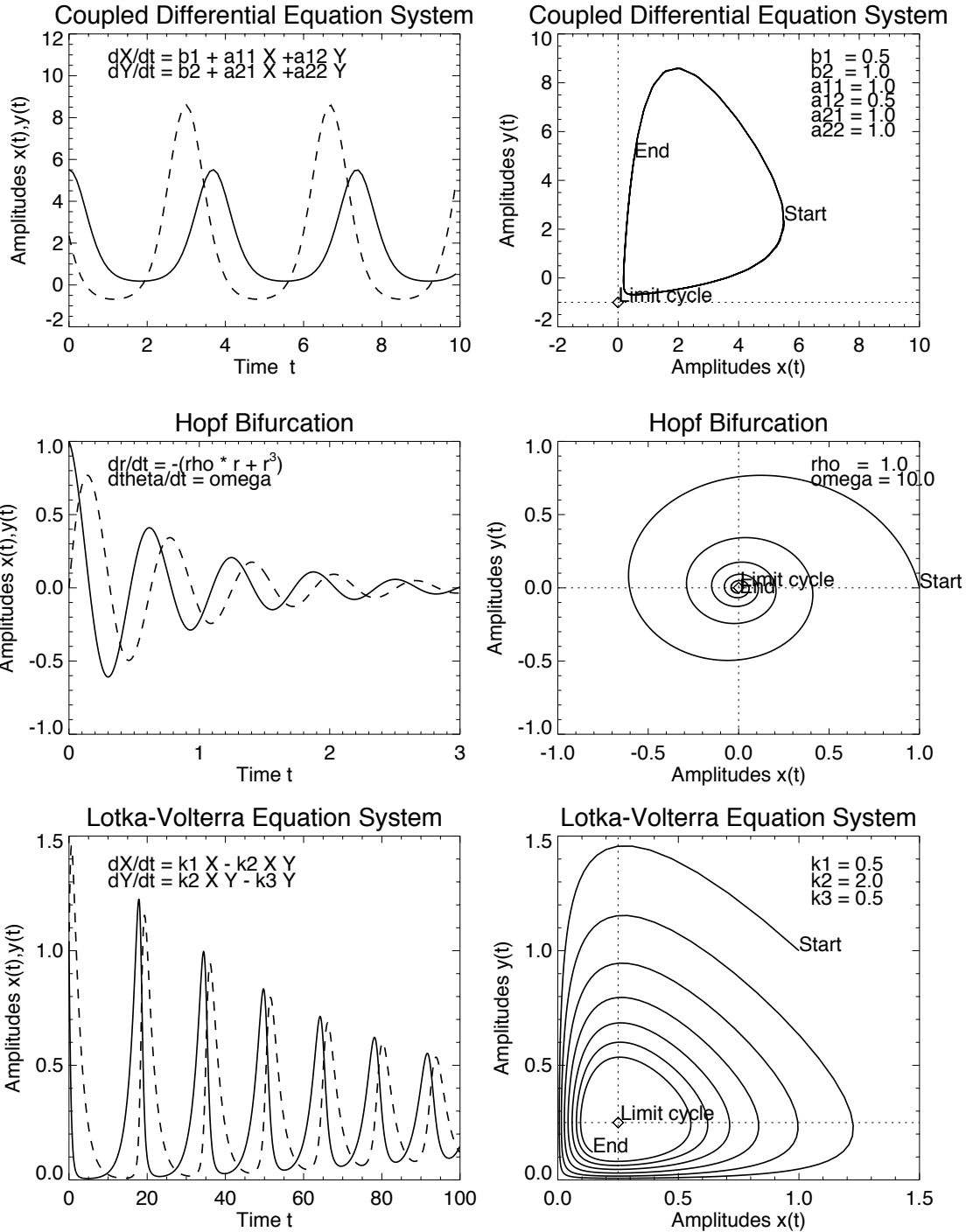


Fig. 18.— The dynamic behavior near a limit cycle is shown for three different nonlinear systems: for coupled oscillators (top), the Hopf bifurcation (middle), and the Lotka-Volterra equation system (bottom). For each case the trajectories are shown in phase space  $Y(X)$  (right panels), and as a function of time,  $X(t)$  and  $Y(t)$  (left panels), for the parameters indicated in the right panels. The system starts to oscillate far away from the limit cycle, but gradually approaches the attractor at the fixed point  $(X_0, Y_0)$ .

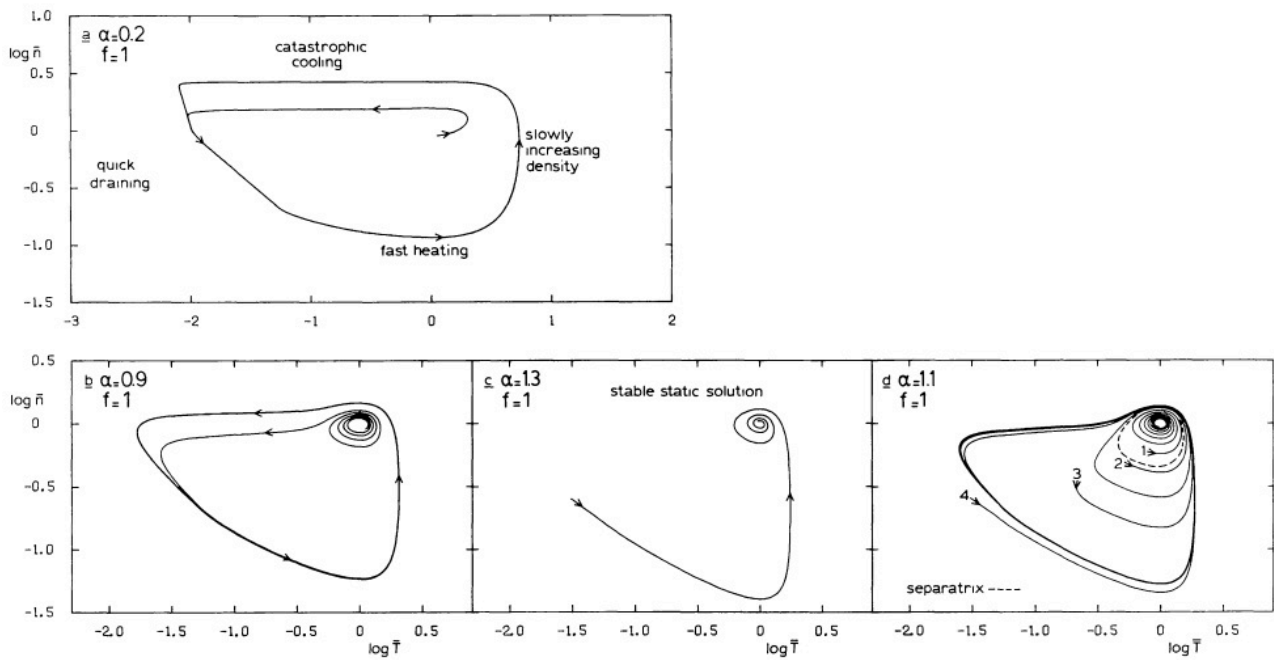


Fig. 19.— Solutions of the evaporation-condensation system (Eq. 24-25) in the phase plane of dimensionless (logarithmic) temperature  $\log(X) = \log(T/T_0)$  and electron density  $\log(n) = \log(n/n_0)$ . Cases (a) and (b) represent nonlinear oscillations near the limit cycle, case (c) is a stable static solution. A separatrix between stable and oscillatory solutions is indicated in (d) [Kuin and Martens 1982].

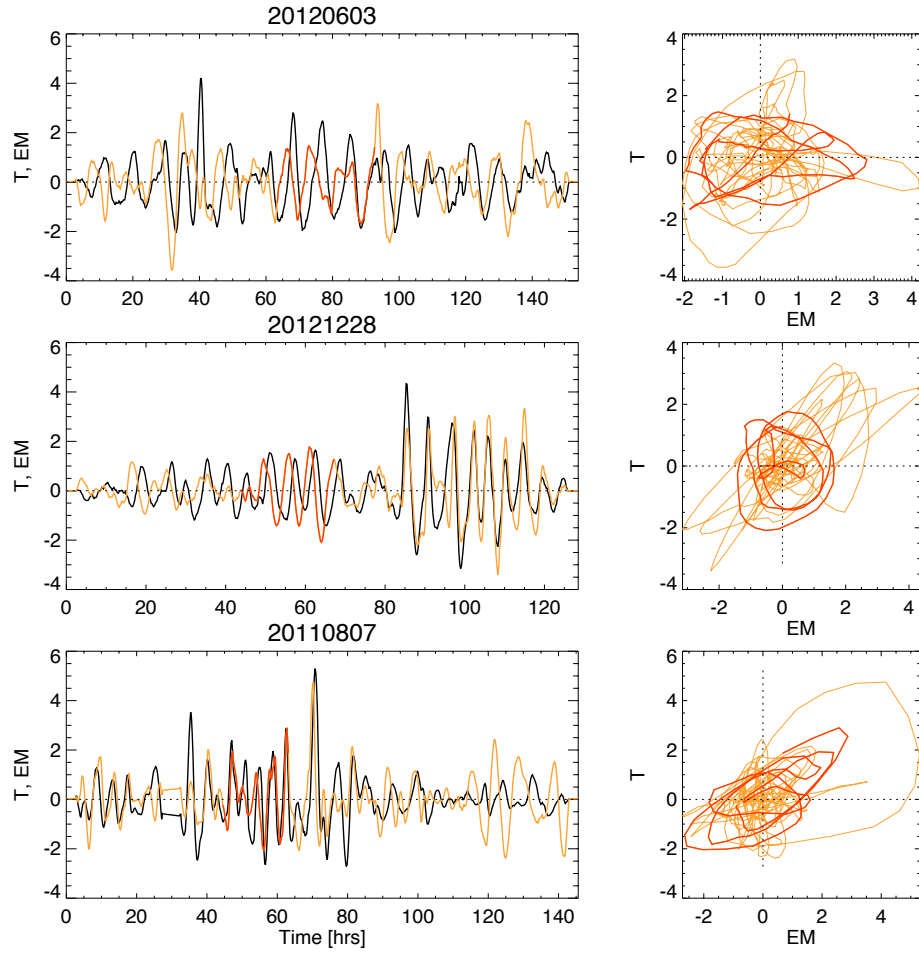


Fig. 20.— Smoothed time profiles of the emission measure  $EM(t)$  (black in left panels) and the electron temperature  $T_e(t)$  (red in left panels, and phase diagram  $T_e(EM)$  (right panels) of three loop episodes observed in an active region with AIA/SDO. A moving average background has been subtracted in all time profiles, and the amplitudes are normalized by their standard deviation from the means. A quasi-stationary time interval with near-elliptical phase trajectories is colored with red. The quasi-periodicity and the phase delay indicate a limit-cycle behavior of the evaporation-condensation cycle in solar flares [Froment et al. 2015].

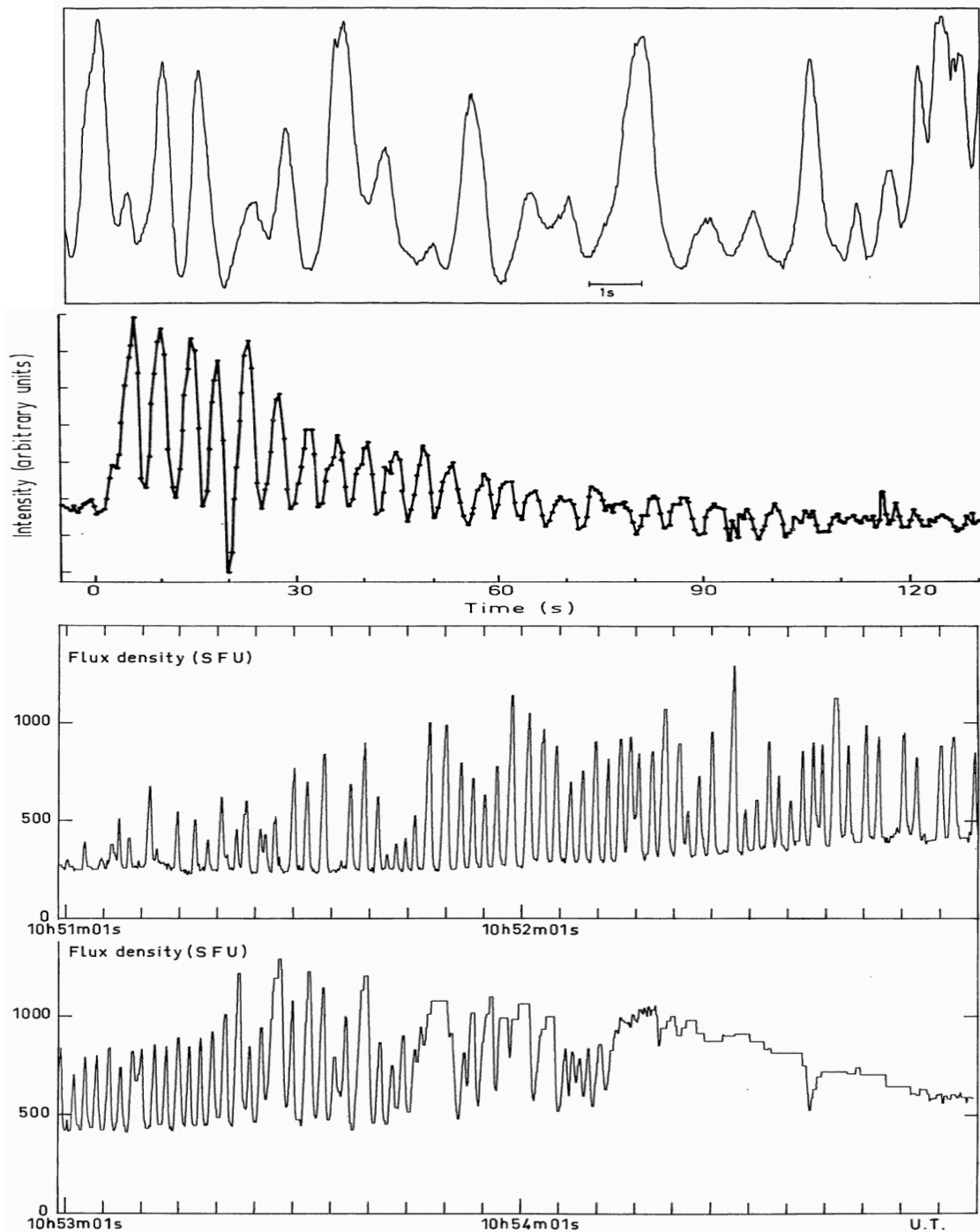


Fig. 21.— Three examples of solar radio burst oscillations: *Top*: Evidence for sub-harmonics (1:3) [Rosenberg 1970]; *Second row*: Exponentially damped oscillation [McLean and Sheridan 1973]; *Third and bottom row*: Metric radio oscillations with a period of  $P \approx 1.5$  s [Trottet et al. 1981].

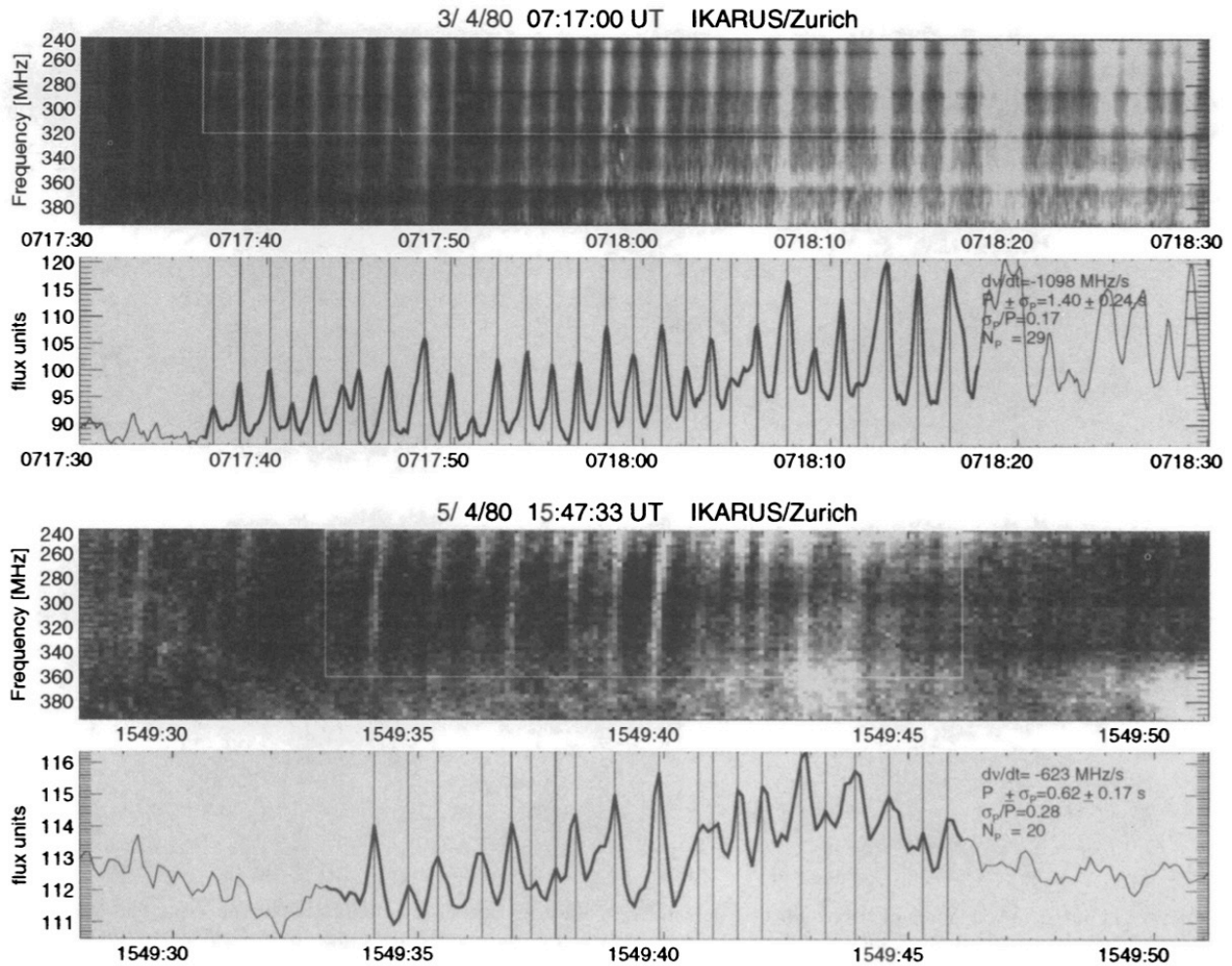


Fig. 22.— Dynamic spectra of solar radio pulsations (top two panels) and a series of type III bursts (bottom two panels), observed with the IKARUS/Zurich spectrograph in the frequency range of 240-400 MHz. The quasi-periodic pulsation pattern is characteristic for nonlinear systems with limit cycles, while the radio type III bursts appear to be produced by a random process [Aschwanden et al. 1994].

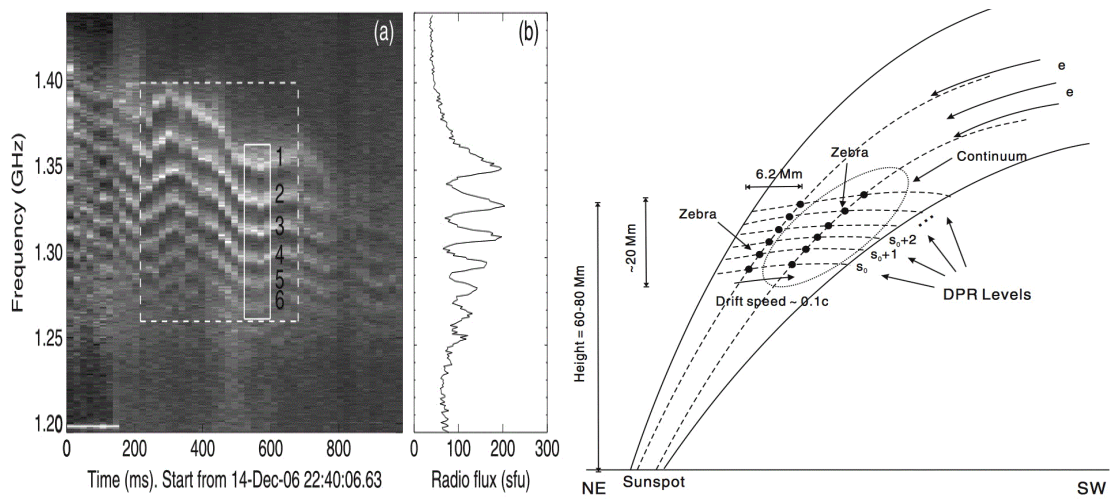


Fig. 23.— *Left*: A zebra-pattern solar radio burst observed on 2006 December 14, 22:40 UT. Six successive stripes with decreasing frequency are marked. *Middle*: A time-averaged flux profile as a function of the frequency, averaged over the box shown in the left panel. *Right*: Simplified spatial model of the location of 6 different harmonics of the gyrofrequency [Chen et al. 2011].

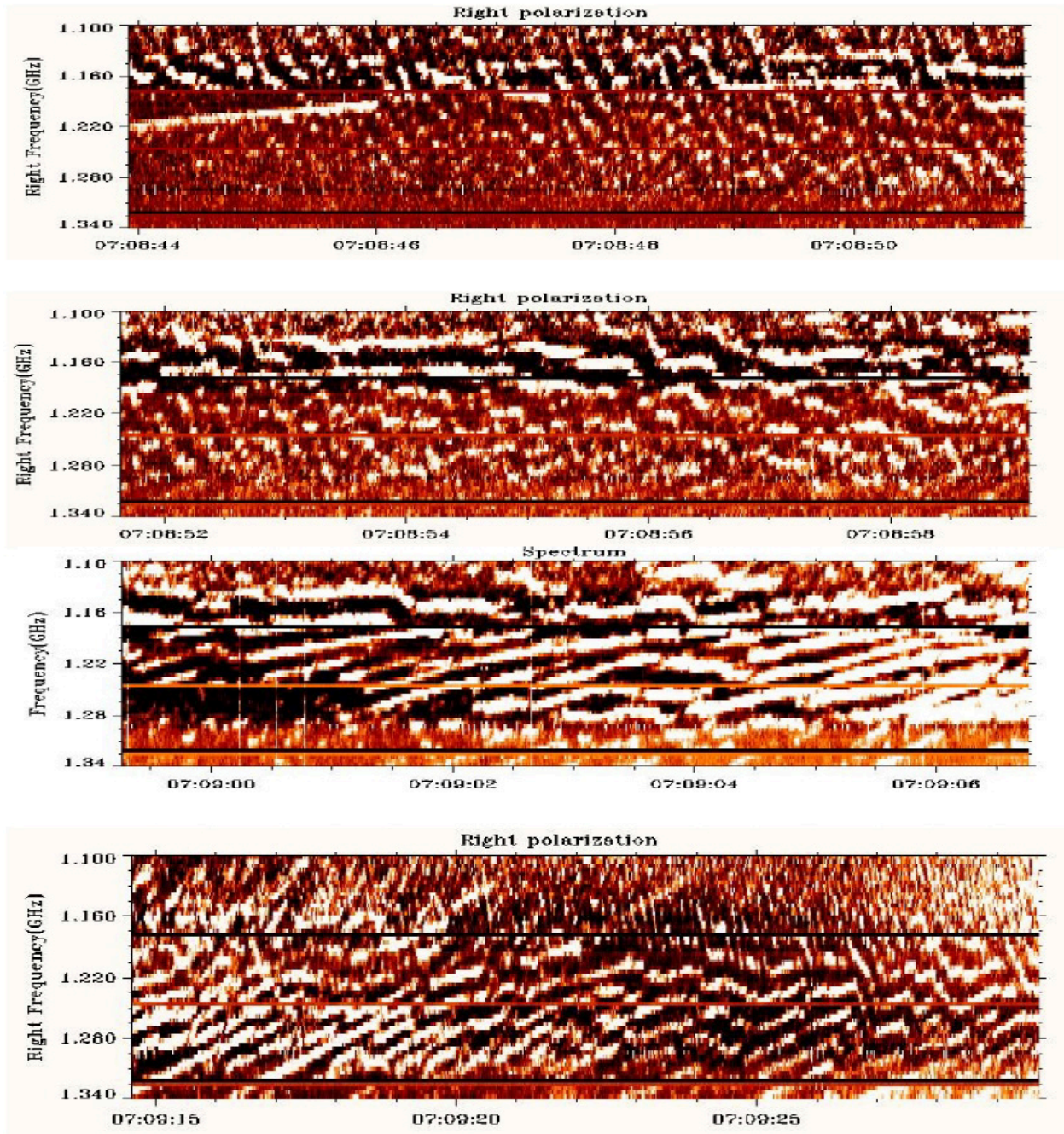


Fig. 24.— This dynamic spectrum (frequency versus time) shows the evolution of zebra-type bursts during 46 s, observed on 2004 December 1 with the Huairou radio station (Beijing). Initial fiber-type bursts transform into zebra patterns, as well as into decimetric millisecond spikes in the lower frequency range of 1110-1160 MHz [Chernov et al. 2017].



Fig. 25.— Star formation regions in the Eagle nebula form spatial structures in the shape of towering pillars [credit Hubble Space Telescope (HST), NASA].

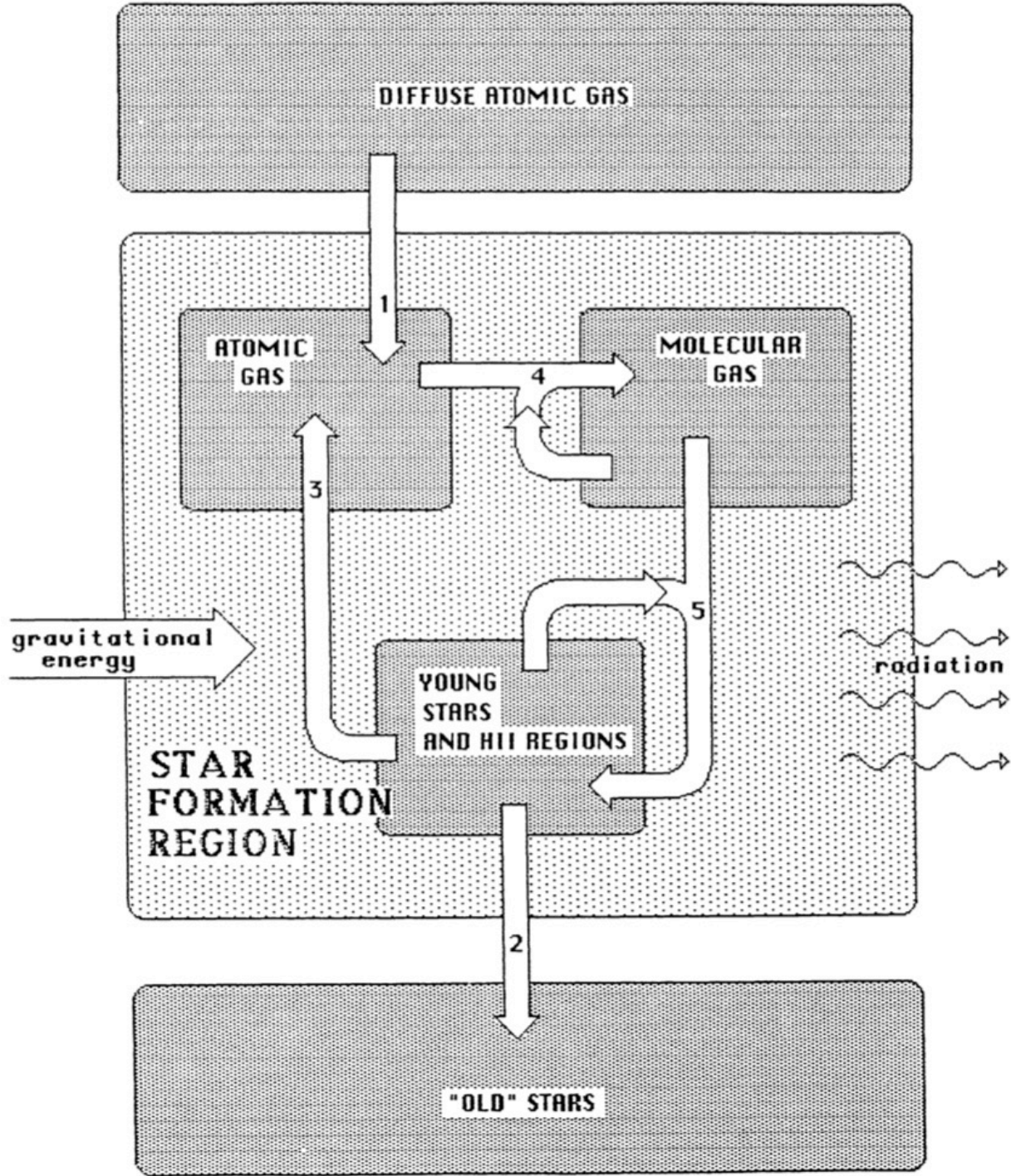


Fig. 26.— The self-organizing system of star formation amounts globally to a transformation of diffuse atomic gas (supply reservoir) into “old” stars (waste reservoir). The internal processes consist of: (1) gas inflow, (2) stellar evolution, (3) stellar mass loss and recombination of ionized gas; (4) production of molecular gas, and (5) triggered star formation [Bodifée 1986].

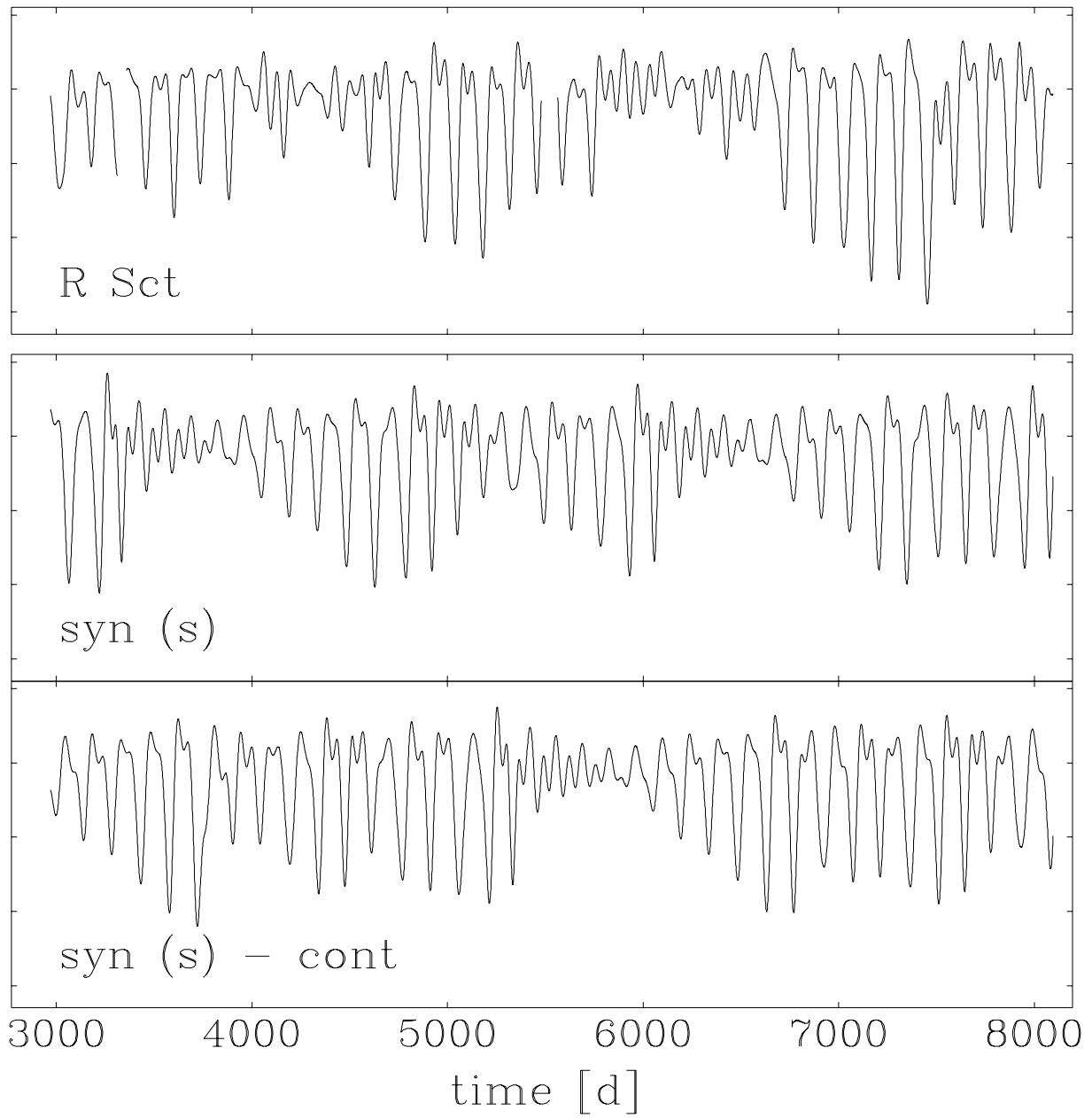


Fig. 27.— The smoothed light curve observed from the RV Tau-type star R Scuti (top) and synthetically generated light curves with a model of a low-dimensional strange attractor (middle and bottom) [Buchler et al. 1996].

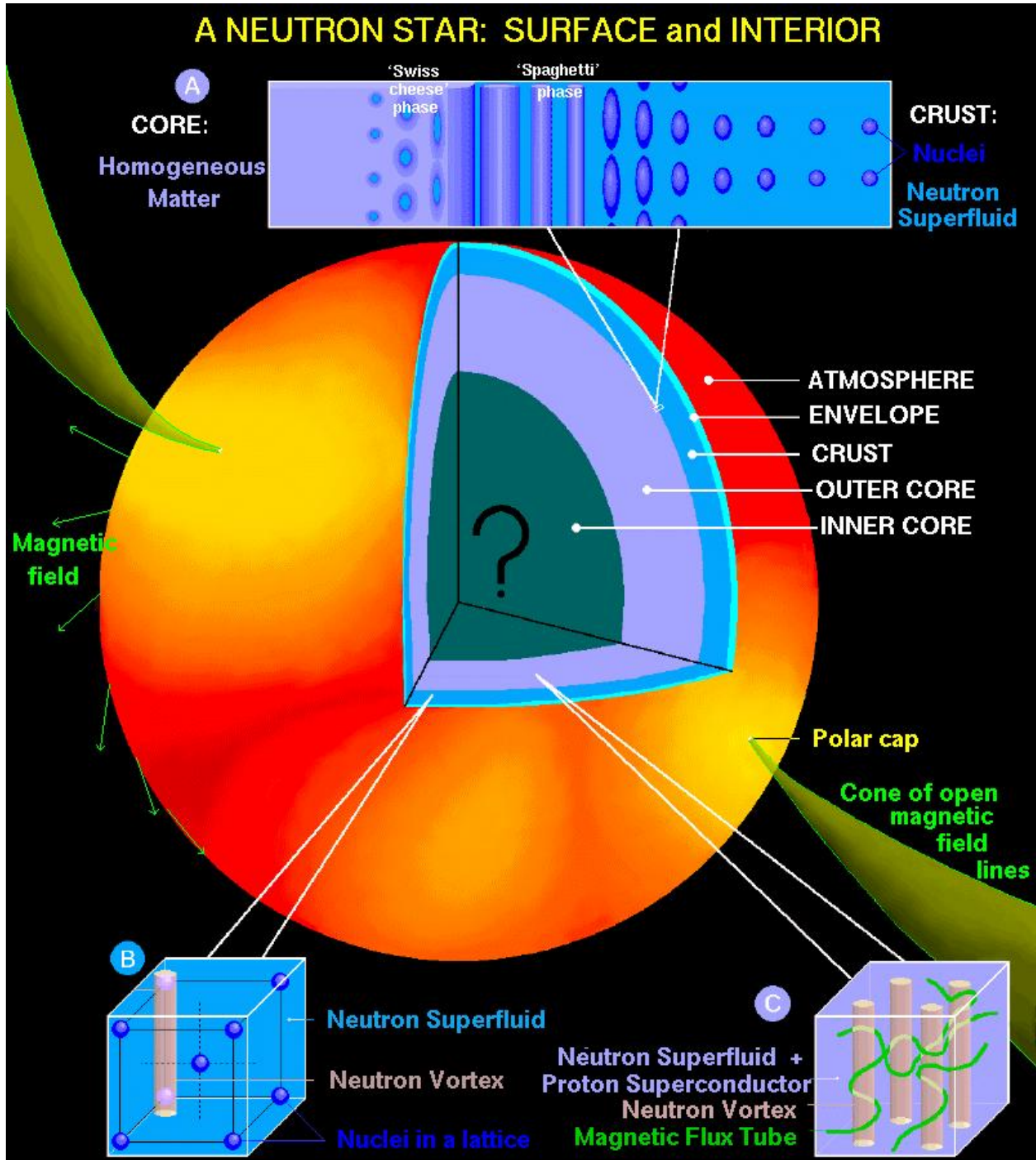


Fig. 28.— A cross-section of a neutron star shows the rich variety of emergent quantum matter expected in its crust and core. [credit: Matthew H. Schneps, Science Media Group, Harvard-Smithsonian Center for Astrophysics (CfA)].

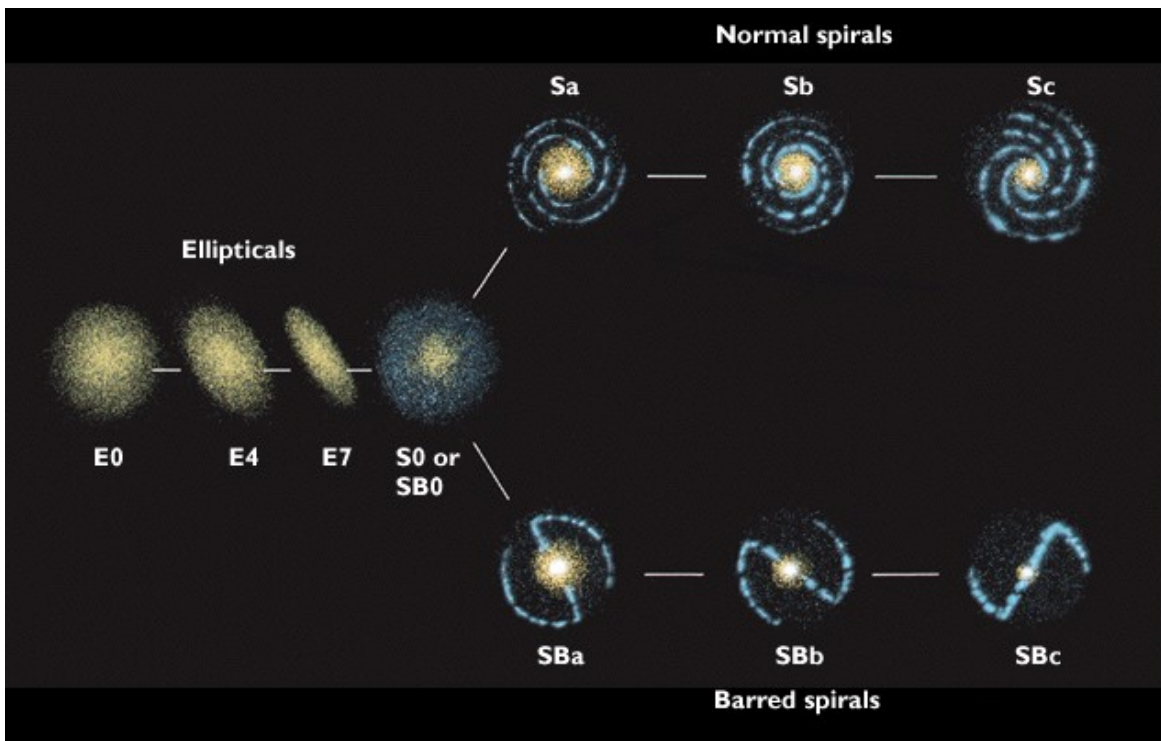


Fig. 29.— The Hubble galaxy classification reflects the morphology from random-like clusters (E0) to spiral-structured ordering (Sc, SBc) [credit [www.physast.uga.edu](http://www.physast.uga.edu)].

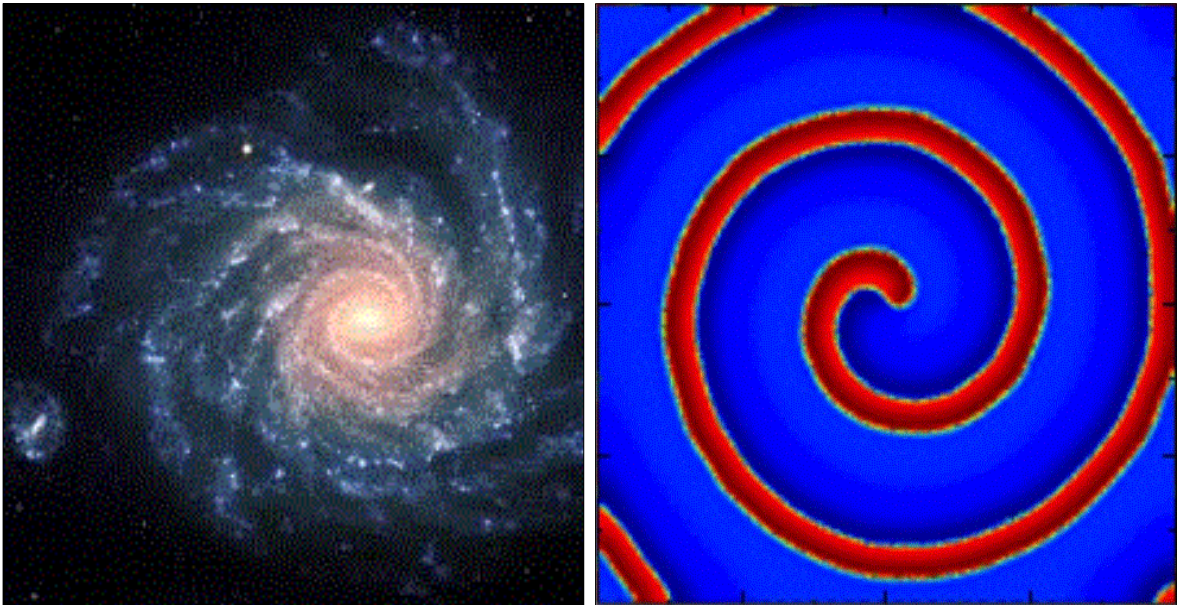


Fig. 30.— *Left*: Spiral galaxy NGC 1232 [Credit: European Southern Observatory (ESO)]; *Right*: Spiral pattern in two-component reaction-diffusion system of Fitzhugh-Nagumo type [Credit: Wikipedia - Reaction-diffusion system].

## EXPANSION OF THE UNIVERSE

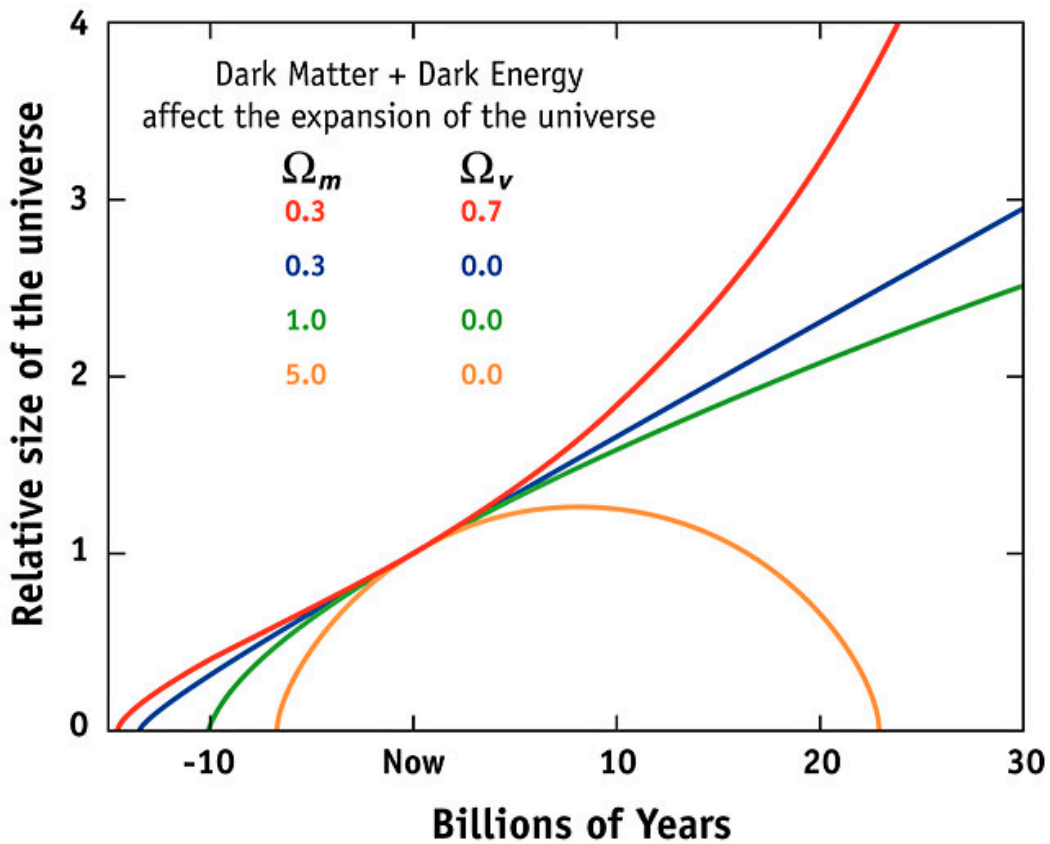


Fig. 31.— Four scenarios of the expansion or contraction of the universe: the closed, high-density universe (orange), the critical-density universe, the Einstein-de Sitter model (green), the open, low-density universe (blue), and the universe in which a large fraction of the matter is in a form of “dark energy” (the  $\Lambda$ CDM model; red), which is causing the expansion of the universe to accelerate [NASA/WMAP Science Team].

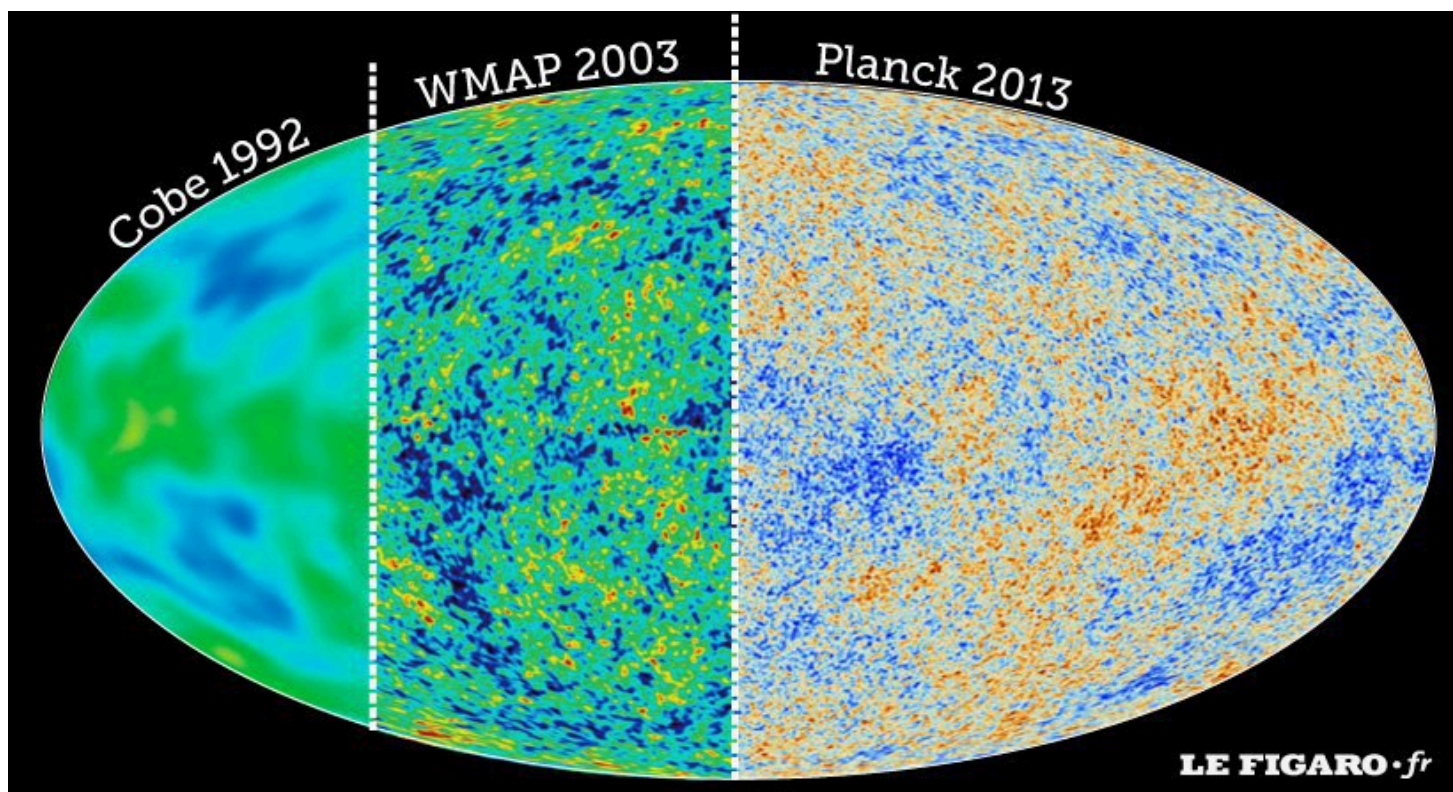


Fig. 32.— Measurements of the spatial distribution and anisotropy of the cosmological microwave background radiation at 3 K with the Cosmic Background Explorer (COBE) in 1992, the *Wilkinson Microwave Anisotropy Probe* (WMAP) satellite in 2003, and the Planck satellite in 2013 [Credit: COBE/NASA, Mather et al. 1991, Boggess et al. 1992; WMAP/NASA, Bennett et al. 2013, Hinshaw et al. 2013; and Planck/ESA; Planck Collaboration 2016].

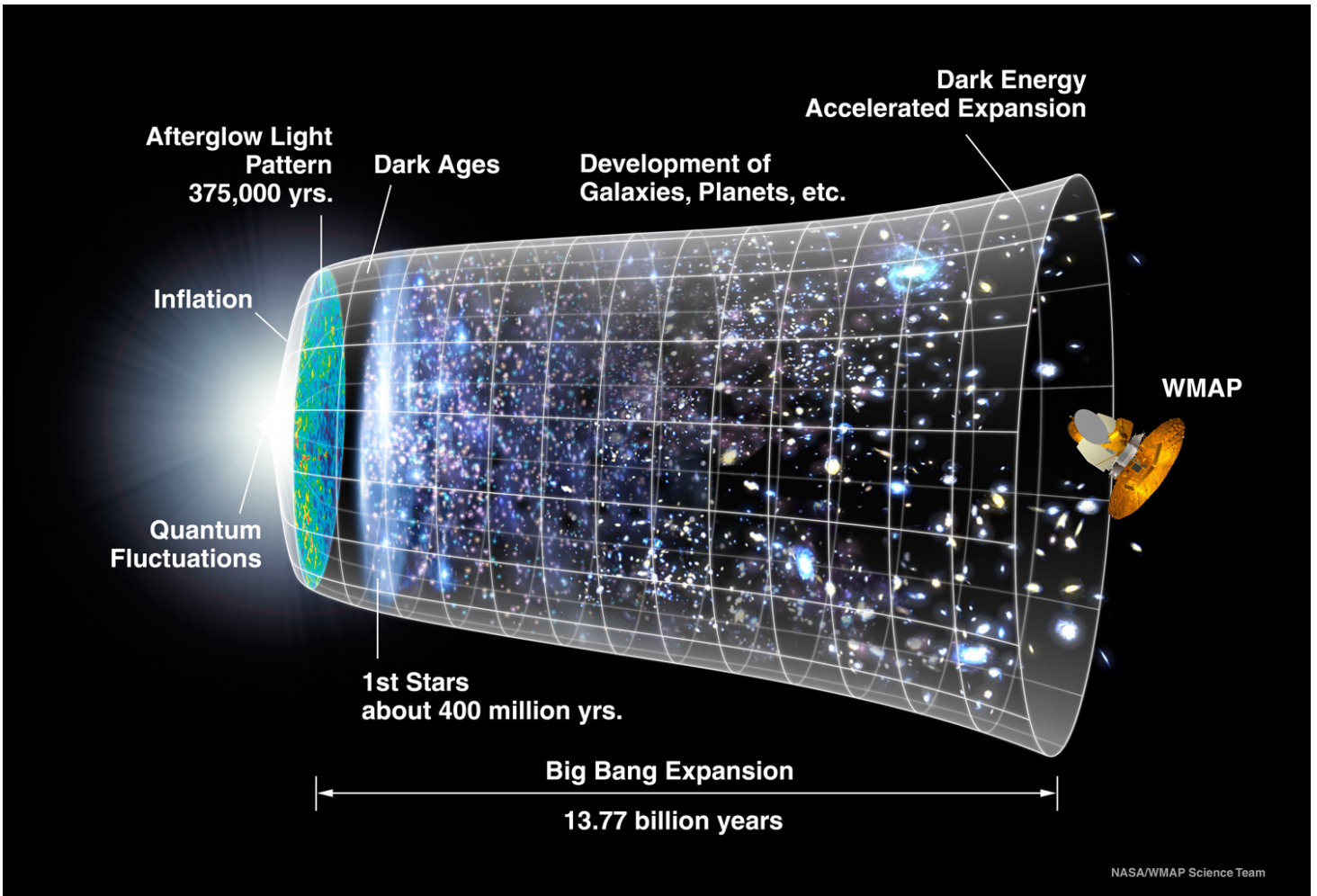


Fig. 33.— A representation of the evolution of the universe over 13.77 billion years. The far left depicts the earliest moment we can now probe, when a period of "inflation" produced a burst of exponential growth in the universe. (Size is depicted by the vertical extent of the grid). For the next several billion years, the expansion of the universe gradually slowed down as the matter in the universe pulled on itself via gravity. More recently, the expansion has begun to speed up again as the repulsive effects of dark energy have come to dominate the expansion of the universe. The afterglow light seen by WMAP was emitted about 375,000 years after inflation and has traversed the universe largely unimpeded since then. The conditions of earlier times are imprinted on this light; it also forms a backlight for later developments of the universe [Credit: NASA/WMAP Science Team].

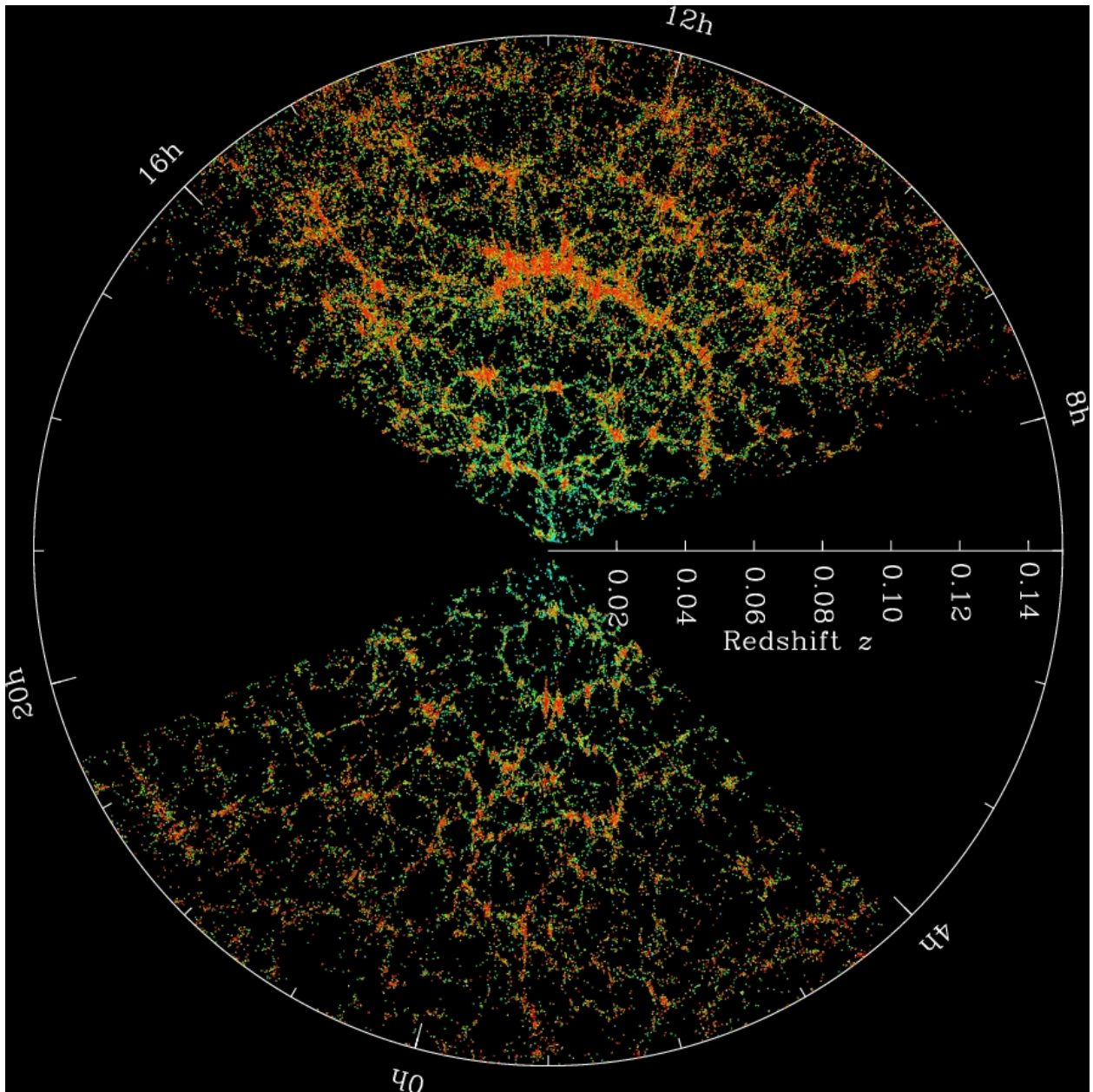


Fig. 34.— *Sloan Digital Sky Survey (SDSS) galaxy map*: A slice of the universe showing the large-scale structure of galaxies. Each dot is a galaxy: the color is the green-red color of that galaxy [Credit: M. Blanton and Sloan Digital Sky Survey, [www.sdss.org](http://www.sdss.org)].

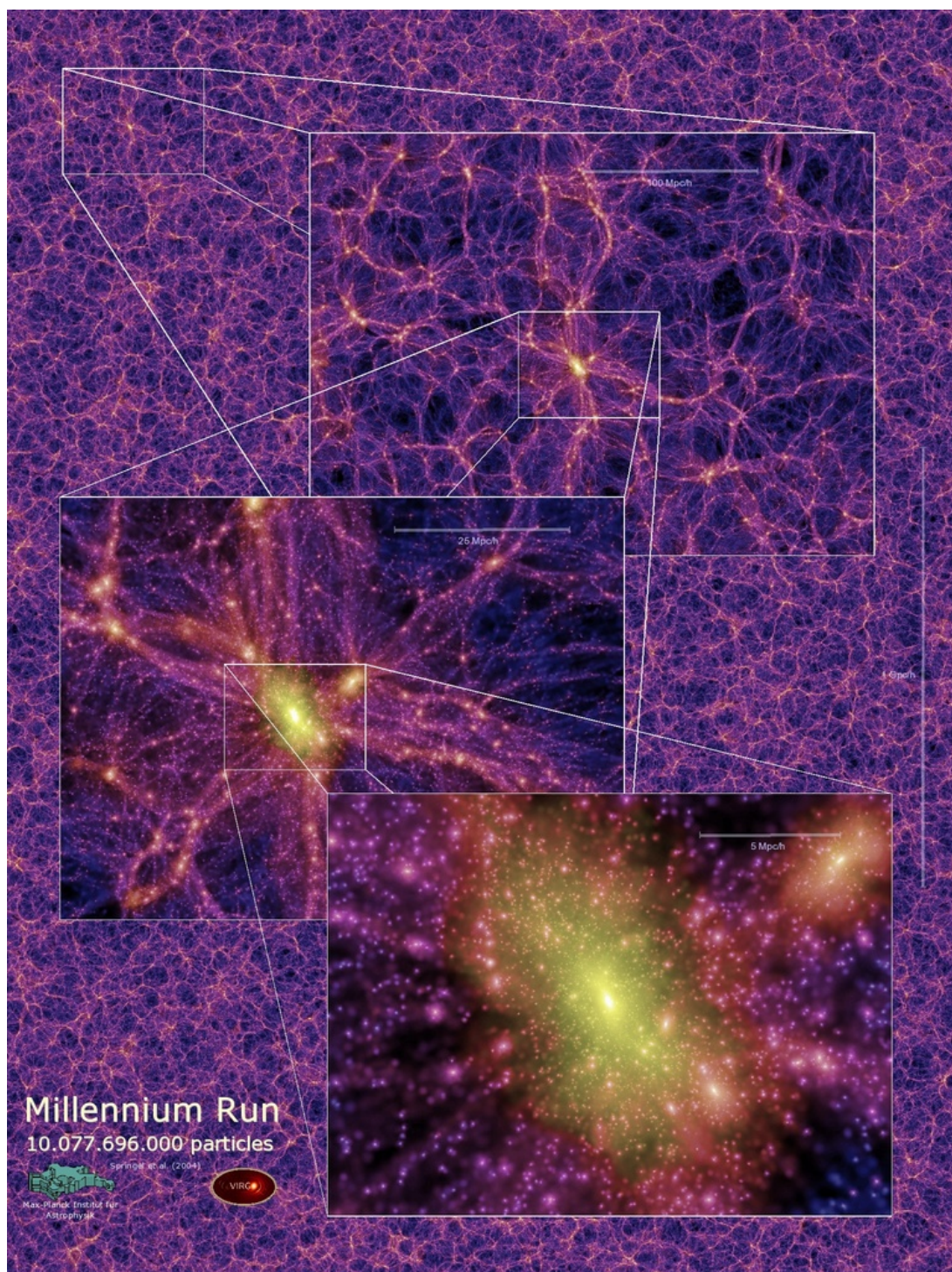
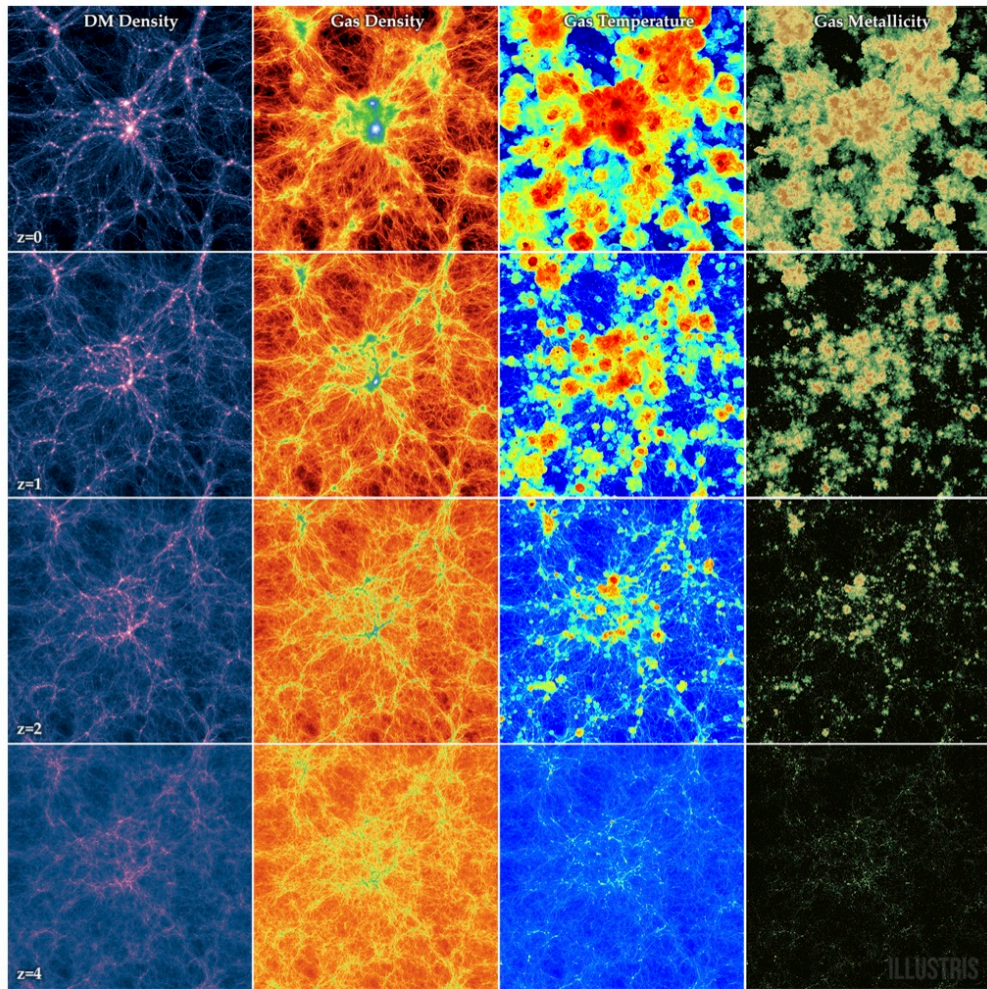


Fig. 35.— Numerical simulations of the dark matter density field on various scales. Each individual image shows the projected dark matter density field in a slab of thickness  $15 h^{-1}$  Mpc (sliced from the periodic simulation volume at an angle chosen to avoid replicating structures in the lower two images), color-coded by density and local dark matter velocity dispersion. The zoom sequence displays consecutive enlargements by factors of four, centered on one of the many galaxy cluster halos present in the simulations [Credit: Millenium Simulation, Virgo Consortium, Max-Planck-Institute for Astrophysics; Springel et al. 2005].



Illustris Collaboration / Illustris Simulation

Fig. 36.— Illustris Simulation (IS) of the galaxy formation in our universe. In the  $\Lambda$ CDM model, galaxies build up their mass hierarchically through the mergers of smaller galaxies to larger ones in a cold dark matter-dominated universe. The time axis is from bottom to top, and the 4 columns contain the dark matter density (left), the gas density, the gas temperature, and the gas metallicity (right column) [Credit: Illustris Collaboration, Illustris Simulation; Vogelsberger et al. 2014].

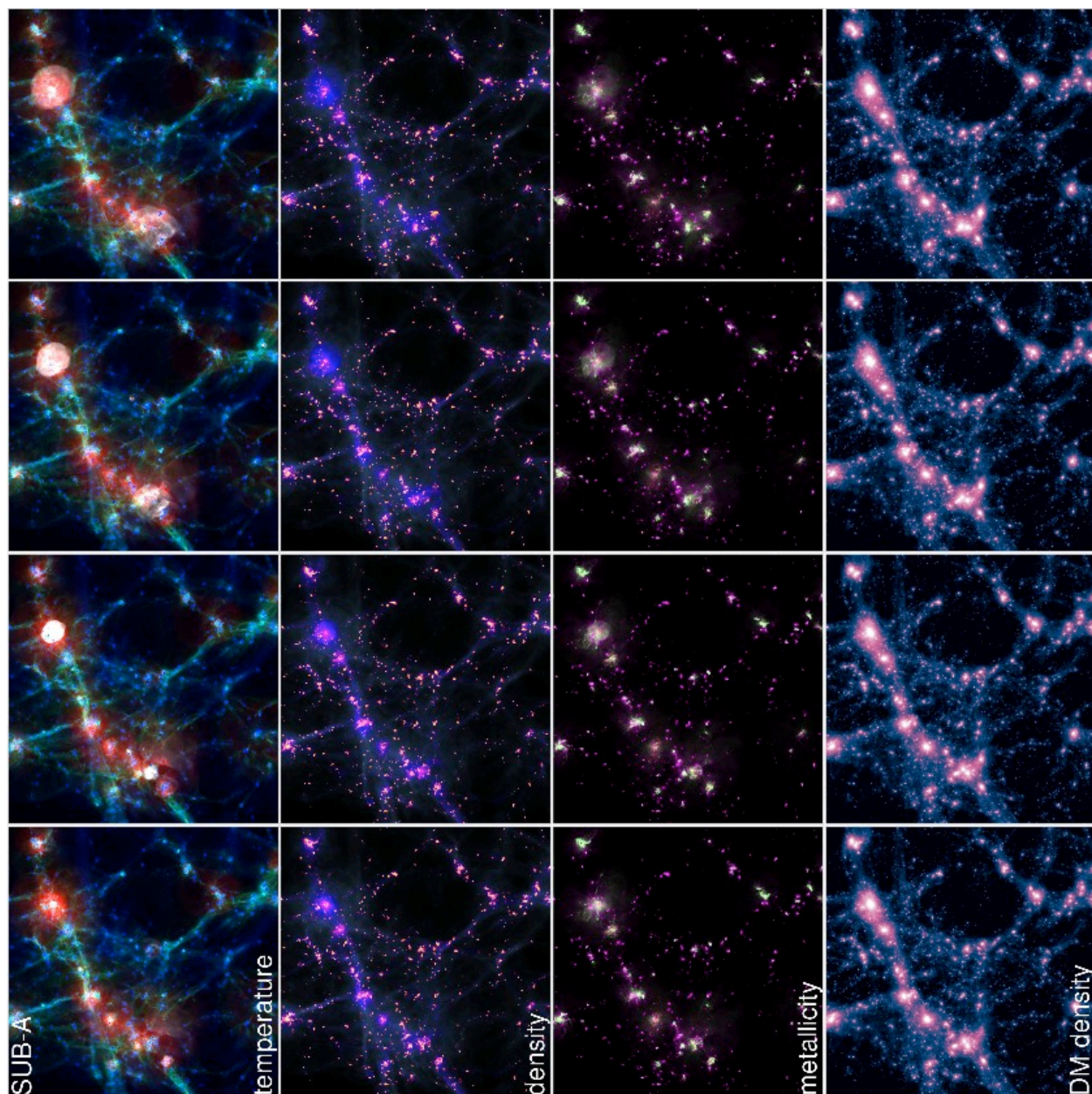
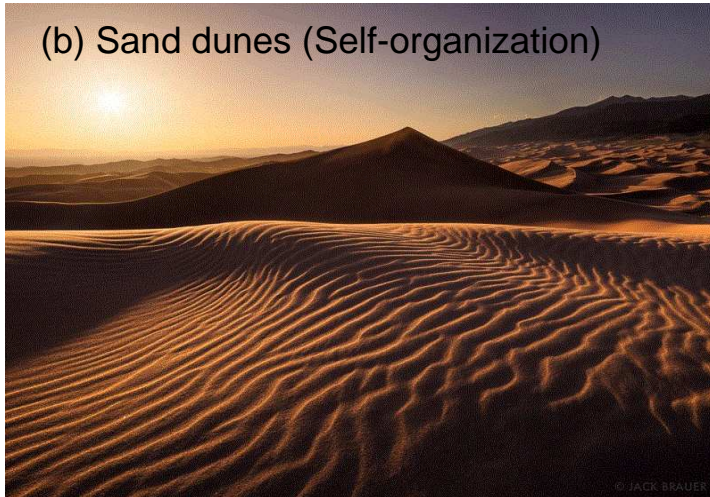


Fig. 37.— Short-time evolution of baryonic parameters (gas temperature, gas density, gas metallicity, Dark Matter density, each one shown in a row, while the columns contain 4 different time steps). The time resolution is less than 3 Myr. The more massive halo in the upper right shows strong AGN activity leading to heating and expansion of large amounts of gas [Credit: Illustris Collaboration, Illustris Simulation; Vogelsberger et al. 2014].

(a) Sand beach (Random process)



(b) Sand dunes (Self-organization)



(c) Sandpile (Self-organized criticality)



Fig. 38.— The same medium (for instance sand) can be subject of three different dynamical processes, such as (a) random processes (sand beach), (b) self-organization (sand dunes), or (c) self-organized criticality (sand piles) [Credit: Google].